




EX LIBRIS
UNIVERSITATIS
ALBERTENSIS

The Bruce Peel
Special Collections
Library



Digitized by the Internet Archive
in 2025 with funding from
University of Alberta Library

<https://archive.org/details/0162015205055>

University of Alberta

Library Release Form

Name of Author: **Jason Lee Young**

Title of Thesis: **Two-Layer Cermet Anodes for Solid Oxide Fuel Cells**

Degree: **Master of Science**

Year this Degree Granted: **2001**

Permission is hereby granted to the University of Alberta Library to reproduce single copies of this thesis to lend or sell such copies for private, scholarly or scientific purposes only.

The author reserves all other publication and other rights in association with the copyright in the thesis, and except as herein before provided, neither the thesis nor any substantial portion thereof may be printed or otherwise reproduced in any material form whatever without the authors prior written permission.

University of Alberta

Two-Layer Cermet Anodes for Solid Oxide Fuel Cells

by

Jason Lee Young



A thesis submitted to the Faculty of Graduate Studies and Research in partial
fulfilment of the requirements for the degree of Master of Science

in

Materials Engineering

Department of Chemical and Materials Engineering

Edmonton, Alberta

Fall, 2001

University of Alberta

Faculty of Graduate Studies and Research

The undersigned certify that they have read, and recommended to the Faculty of Graduate Studies and Research for acceptance, a thesis entitled "TWO-LAYER CERMET ANODES FOR SOLID OXIDE FUEL CELLS" submitted by JASON LEE YOUNG in partial fulfilment of the requirements for the degree of MASTER OF SCIENCE in MATERIALS ENGINEERING.

Abstract

A new process originally developed for sensors shows promise for producing two-layer cermet anodes for Solid Oxide Fuel Cells. Traditionally cermets of randomly interspersed Ni and YSZ powders result in a mostly discontinuous Ni phase, impeding the conductivity unless the electrode is made thicker or contains a larger Ni fraction. The polarized electrochemical vapour deposition (PEVD) technique deposits thin uniform layers of YSZ over the surface of high aspect ratio electron conducting substrates. Film growth characteristics proceed according to Wagner scale growth theory, producing ultrathin ($< 1 \mu\text{m}$) membranes for low electronic transport number (t_e) 8 YSZ and thin films ($1\text{-}2 \mu\text{m}$) for 3 YSZ which have a larger t_e . Chloride sublimation temperatures of 170°C and $720\text{-}735^\circ\text{C}$ for ZrCl_4 and YCl_3 , respectively, resulted in films with 3 - 14 mol% yttria in a linear relationship. Preliminary I-V and impedance spectroscopy investigations on low t_e 8-10 mol% yttria films indicate a drop in cell current density and an increase in electrode resistance.

Acknowledgements

I would like to thank Dr. T. H. Etsell for his advice, support, encouragement and especially the confidence in my abilities he has imparted throughout the course of this study.

I would also like to thank all of the staff in the department who provided assistance assembling and carrying out experiments, for providing equipment, for their advice and for their friendship, especially Dr. E. Z. Tang, Ms. T. Barker, Mr. S. Merali, Dr. J. L. Luo, Mr. B. Konzuk, Mr. M. Haldane and Ms. P. Cameron.

Of course, I could not have done this without the love and support of my wife Margaret, my mom Audrey, my dad Dennis and all of my friends and relatives.

Table of Contents

Chapter 1	Introduction	1
Chapter 2	Thick and Thin Film Ceramic Processing in Solid Oxide Fuel Cells	4
2.1	Thick Film Processing	6
2.1.1	<i>Powder Production</i>	7
	Conventional Ceramic Processing	7
	Precipitation Powder Processing	8
	Colloidal Suspensions	9
	Sol-Gel	9
2.1.2	<i>Thick Film Application Methods</i>	10
	Screening, Dipping, Spraying and Spin Coating	10

	Tape Casting	11
	Electrophoretic Deposition	12
	Plasma Spray Deposition	13
	Laser Spraying	13
2.1.3	<i>Sintering</i>	14
	Sintering Aids	15
	Plasma Enhanced Sintering	17
2.2	Thin Film Processing	18
2.2.1	<i>Sputtering</i>	18
	Reactive Sputtering	19
	Other Sputtering Systems	20
2.2.2	<i>Vapour Phase Deposition</i>	21
	Vapour Pressure	23
	Evaporation Rates	24
2.2.3	<i>Chemical Vapour Deposition</i>	25
2.2.4	<i>Electrochemical Vapour Deposition</i>	28
	Pore Closure	29
	Scale Growth	30
	Deposition Rate	31
	Film Composition Control	33
	Film Morphology	36
	EVD with NiO as an Oxygen Source	37
	Vapour Phase Electrolytic Deposition	39

Chapter 3 Solid State Ionic Conductors 40

3.1	Ion Conduction Mechanisms in Solid Electrolytes	42
3.2	Properties of Good Solid Ionic Conductors	43
3.3	Fluorite-Type Oxygen Ion Conductors	44
3.3.1	<i>Zirconia-Based Electrolytes</i>	49
	Tetragonal Zirconia Polycrystals	52
	Mixed conductors	53

3.3.2	<i>Bismuth Oxide-Based Electrolytes</i>	54
3.3.3	<i>Ceria-Based Electrolytes</i>	55
	Composite Electrolytes	56
3.3.4	<i>Thoria Based Electrolytes</i>	57
3.3.5	<i>Hafnia Based Electrolytes</i>	57

Chapter 4 **Fuel Cells** **59**

4.1	Fuel Cell Operation	60
4.1.1	Fuel cell Performance	62
	Resistive Polarization	63
	Chemical Polarization	64
	Concentration polarization	64
4.1.2	<i>Electrochemical Impedance Spectroscopy in Fuel Cells</i>	65
4.2	Fuel Cell Classification	70
	Acid Fuel Cells	71
	Alkaline Fuel Cells	71
	Molten Carbonate Fuel Cells	72
	Solid Polymer Fuel Cells	72
	Solid Oxide Fuel Cells	73
4.3	Materials for Solid Oxide Fuel Cells	74
4.3.1	<i>Interconnect</i>	74
4.3.2	<i>Electrodes</i>	76
	Cathode	78
	Anode	81
	Platinum	82
4.4	Electrode Morphology	85
4.4.1	<i>Two-Dimensional Interface</i>	87
4.4.2	<i>YSZ/Metal Cermet Mixtures</i>	87
4.4.3	<i>Mixed Conducting Electrodes</i>	90
4.4.4	<i>Two-Layer Cermet Electrodes</i>	92

Chapter 5	Experimental	94
5.1	PEVD Deposition	96
5.2	Microstructure and Composition Studies	97
5.3	Electrochemical Studies	98
Chapter 6	Results and Discussion	99
6.1	Deposition Parameters	102
6.2	Film Composition Analysis	105
6.3	Film Morphology	110
6.4	Current Characteristics During Deposition	116
6.5	Electrochemical Characterization	116
6.5.1	<i>Current-Voltage Characteristics</i>	116
6.5.2	<i>Electrochemical Impedance Spectroscopy</i>	123
6.5.3	<i>Electrochemical Properties</i>	124
6.6	Future Considerations	125
Chapter 7	Conclusions	127
	 References	 130
Appendix 1	Wavelength Dispersive X-ray Analysis Data	143

List of Tables

2.1 - Selected vapour pressure data	35
3.1 - Solid ionic conductors and their primary charge carriers	41
3.2 - Bulk grain and grain boundary resistivity values measured at 300°C for samples of zirconia with varying yttria contents	53
5.1 - Burnout and sintering program used for 4 YSZ electrolytes by the Doctor Blade technique	95
6.1 - Measured chemical contents by WDX and the yttria content in the YSZ membranes (wt%). * represents the zircon standard after correcting for Pt/Zr peak overlap	107

List of Figures

Figure 2.1 - Common porosity effects in ceramic materials.	6
Figure 2.2 - Particle size distribution after (A) oven drying at 80°C and (B) centrifuging and microwave drying.	7
Figure 2.3 - Effect of mechanical methods on the breakdown of agglomerates by (A) stirring in water, (B) ultrasonic agitation, (C) ultrasonic probe disruption and (D) two days of ball milling in water plus lignosulphonate dispersant.	8
Figure 2.4 - Effect of acid concentration on particle size in sol-gel synthesis	11
Figure 2.5 - Grain boundary traction of a large pore in a polycrystal	16
Figure 2.6 - Sintered density of Y-TZP as a function of MgO content	17
Figure 2.7 - Schematic representation of the sputter deposition process	19
Figure 2.8 - Schematic diagram of the electron beam evaporation technique used by Yoshida and Toda, 1989	22

Figure 2.9 - Schematic diagram of the CVD process.	27
Figure 2.10 - Common porosity effects in ceramic materials.	29
Figure 2.11 - Particle size distribution after (A) oven drying at 80°C and (B) centrifuging and microwave drying.	30
Figure 2.12 - Transport processes for EVD scale growth	31
Figure 2.13 - Relationship between thin film and gas composition in MOCVD	34
Figure 2.14 - Comparison of equilibrium dopant concentration with experimental data	36
Figure 2.15 - Gap observed using NiO as an oxygen source for EVD	38
Figure 3.1 - Cubic fluorite type structure of stabilized ZrO_2	44
Figure 3.2 - Oxide ion conductivity of some oxides with fluorite-type or fluorite related crystal structures	45
Figure 3.3 - Schematic representation of $\log \sigma$ surfaces over $\log P_{x_2}$ and $1/T$ space .	48
Figure 3.4 - Relationship between electrolyte and ionic domain boundaries in the $\log P_{x_2}$, $1/T$ plane	50
Figure 3.5 - Activation energy from 950°C to 1050°C versus molar yttria content	51
Figure 3.6 - SEM micrographs illustrating the variation in grain size distribution as a function of yttria content. All materials sintered at 1600°C for 2 h ...	53
Figure 4.1 - Schematic diagram of the fuel cell reaction	61
Figure 4.2 - Potential versus current density graph illustrating the various polarizations that affect fuel cell performance	63
Figure 4.3 - Complex impedance loci for R-C-Z(f) circuits	68
Figure 4.4 - Equivalent circuit and schematic of the complex plane plot where R_s is the solution resistance, C the double layer capacitance, R_t the transfer resistance, p the faraidic resistance and L the self inductance	69
Figure 4.5 - Impedance spectra calculated with stepwise charge transfer model, as a function of polarization	70
Figure 4.6 - Measured impedance Spectrum at 700°C and 1 atm O_2 and its equivalent circuit	83
Figure 4.7 - Impedance spectrum at 800°C of platinum electrodes for YSZ fuel cells before and after reduction in a hydrogen environment	84
Figure 4.8 - Reversible surface adsorbed oxygen coverage on a platinum cathode due to anodic and cathodic current. Coverage is shown for before, during and after current passage	85

Figure 4.9 - Schematic diagram of the reaction zone of an SOFC cermet anode	88
Figure 4.10 - Effect of YSZ conductivity in the cermet on the exchange current density at 1000°C	89
Figure 4.11 - Illustration of a purely electronic conducting electrode with a two-dimensional reaction interface (left) and a hypothetical mixed conducting electrode with a three-dimensional reaction zone	90
Figure 4.12 - Schematic representation of a two-layered electrode	92
Figure 5.1 - Schematic diagram of two designs used for the PEVD reactor.	95
Figure 5.2 - Apparatus used for PEVD deposition. Anode reactants and gases enter through the glove box on the right and cathode gases enter on the left of the tube furnace.	96
Figure 5.3 - Schematic diagram of PEVD reactor design	97
Figure 6.1 - Schematic diagram of the PEVD process	102
Figure 6.2 - Schematic representation of electron flow in the EVD and PEVD process	102
Figure 6.3 - SEM micrograph of a plan view of a platinum electrode after sintering at 975°C for 15 minutes.	103
Figure 6.4 - SEM micrograph of a plan view of a platinum electrode after sintering in air for 7 d at 950°C	104
Figure 6.5 - Pt, Y and Zr standards at 20 kV accelerating voltage in EDX	106
Figure 6.6 - Pt, Y and Zr standards at 30 kV accelerating voltage in EDX	107
Figure 6.7 - Platinum, yttrium and zirconium standards at 20 kV accelerating voltage in WDX	109
Figure 6.8 - Theoretical and experimental yttria content versus yttrium chloride temperatures while maintaining a constant ZrCl_4 temperature of 170°C.	110
Figure 6.9 - Preferred growth direction of an ionic conducting layer over electronically (metal electrode) and ionically (YSZ electrolyte) conducting layers	110
Figure 6.10 - PEVD membrane over porous platinum in both (A) secondary and (B) backscattered electron images. The dark phase is the PEVD membrane and the white phase is the platinum	112
Figure 6.11 - Secondary electron images of membranes deposited over (A) 24 h and (B) 72 H containing 3 mol% yttria	113
Figure 6.12 - Zirconium content over the film thickness.	114

Figure 6.13 - Morphology of zirconia membranes containing (A) 3 mol% yttria and (B) 12 mol% yttria 115

Figure 6.14 - I-V characterization of Pt electrodes before PEVD deposition of 8 YSZ using 4 YSZ electrolytes. 118

Figure 6.15 - I-V characterization of Pt electrodes after PEVD deposition of 8 YSZ using 4 YSZ electrolytes. 119

Figure 6.16 - I-V characterization of Pt electrodes before PEVD deposition of 8 YSZ using 8 YSZ electrolytes. 120

Figure 6.17 - I-V characterization of Pt electrodes after PEVD deposition of 8YSZ using 8YSZ electrolytes. 121

Figure 6.18 - Platinum electrodes sintered in (A) air and (B) hydrogen for 168 h ... 122

Figure 6.19 - Typical impedance plots at 950°C before (A) and after (B) PEVD deposition of 8 YSZ using 8 YSZ electrolytes. 123

List of Symbols

a	Activity
A	Area
A_e	Area of Evaporation
α	Thermal Expansion Coefficient
α_v	Evaporation Coefficient
C	Capacitance
c_b	Bulk Concentration
c_{if}	Interface Concentration
C_{int}	Constant
C_p	Heat Capacity
d	Lattice Parameter
ΔG_e°	Standard Free Energy of Evaporation
ΔH_e	Molar Heat of Evaporation

ΔH°_e	Standard Heat of Evaporation
ΔS°_e	Standard Enthalpy of Evaporation
E	Young's Modulus
\mathcal{E}	Electromotive Force
f_r	Residual Solvent of Fully Dried Film
f_s	Volume Fraction of Solvent at Gel Point
\mathcal{F}	Faraday's Number
γ_{SL}	Solid/Liquid Interfacial Energy
I	Current
J	Current Density
J_l	Limiting Current Density
J_o	Exchange Current Density
k	Boltzman's Constant
l_{eq}	Equivalent length
L	Inductance
m	Molecular Weight
M_k	Mole Percent Dopant
μ_c	Chemical Potential of the Condensed Phase
μ_g	Chemical Potential of the Gas Phase
n	Number of Electrons
N_c	Number of Atoms
η_a	Anode Polarization
η_c	Cathode Polarization
p	Hydrostatic Pressure
p^*	Thermodynamic Equilibrium Pressure
P_k	Number of Ions per Unit Cell
ϕ	Phase Angle
Q	Activation Energy
Q_{CPE}	Constant Phase Element
r_c	Cation Radius
R	Resistance
R	Gas Constant
R_k	Ionic Radius
R_s	Solution Resistance
R_t	Transfer Resistance

ρ	Faraidic Resistance
s	Channel Radius
S	Particle Solubility
S_o	Solubility of a Flat Plate
σ	Conductivity
σ_T	Tensile Stress
t	Time
t_e	Electron Transference Number
T	Temperature
V_{ac}	a.c. Voltage
V_{chem}	Chemical Polarization
V_{conc}	Concentration Polarization
V_m	Molar Volume
ν	Poisson's Ratio
ω	Angular Frequency
x	Particle Radius
Z	Impedance

As the world comes to grips with the rising costs of a finite energy supply whose use has been linked to global warming, energy efficiency is becoming a primary concern. Electric efficiencies of nearly 60% for gas-fired combined cycle (steam and gas) turbine plants and 47% for coal-fired steam cycles can now be attained as a result of advanced technologies (Winkler and Koeppen, 1996). Solid oxide fuel cells (SOFC's) are highly efficient energy conversion devices that produce electricity by the electrochemical combination of a variety of fuels with oxidant gases across an ionic conducting oxide (Minh, 1993). Inefficient mechanical conversion steps are eliminated and a high quality waste heat is produced that can be used in a combined cycle or cogeneration system and result in efficiencies of up to 80 %, effectively lowering CO₂, particulate, NO_x, SO_x and noise pollution.

The challenge is to develop materials with adequate electrocatalytic activity without significant performance losses for tens of thousands of hours (Antonucci et al., 1997). Several

optimistic authors have ventured out to say that SOFC's would be producing power within the next five to 10 years (Sheppard, 1987). Those articles were written 10 to 15 years ago. The greatest stumbling block to commercial development are problems related to the high operating temperatures of the fuel cells necessary to attain a reasonable power density, including electrode sintering, interfacial diffusion between fuel cell components and mechanical stresses arising from different thermal expansion coefficients. Tests show that power output decreases and internal resistance increases with thermal cycling as a result of local ruptures at the interfaces of the electrode layers of the anode and cathode with the electrolyte (de Souza et al., 1997a; Hsiao and Selman, 1997).

In solid oxide fuel cells, the Ni-YSZ cermet anodes and $\text{La}_{0.7}\text{Sr}_{0.3}\text{MnO}_3$ cathodes, the most commonly used electrode materials, have electronic resistivities of less than $10^{-2} \Omega\cdot\text{cm}$ and usually do not significantly influence the overall cell resistance. Likewise, transport of gaseous species through the electrodes is usually rapid and thus its effect on performance is only significant at high current densities and/or low electrode porosities. The contribution to the cell resistance of an 8 mol% yttria-stabilized zirconia (8 YSZ) electrolyte (35 to $50 \Omega\cdot\text{cm}$ at 800°C) has, with recent advances in thin film technology, been significantly reduced such that it is now possible to produce electrolytes thinner than $15 \mu\text{m}$ with area specific resistance of less than $0.1 \Omega\cdot\text{cm}^2$ at 800°C (although in practice, it is normally well above $0.5 \Omega\cdot\text{cm}^2$). At present, the primary concern is the slow rate of interfacial (charge-transfer) reactions which often limits performance (Tanner et al., 1997).

Electrode kinetics and electrode/electrolyte interface stability of the cells in particular, play the most important role in their performance. Thus, there is a need to understand the behaviour of electrodes in terms of design parameters in order to advocate materials and fabrication technologies which will improve the overall performance of the cell. This requires a detailed knowledge of the atomistic structure and composition of the interface, as well as that of the intermediate species of the electrode processes, and the influence of changes of the electrode potential, work function and electron affinity on the interface structure and kinetics (Göpel and Wiemhöfer, 1990; Zipprich et al., 1995; Tanner et al., 1997).

This thesis is divided into seven chapters. Chapters 2 through 4 confer an overview of the present technology as it relates to solid oxide fuel cells. Chapter 2 is a summary of deposition techniques used for component fabrication, especially the electrodes, and those processes directly related to the polarized electrochemical vapour deposition (PEVD) technique. Chapter 3 is a review of solid state ionic mechanisms and properties, and some of the more common ionically conducting materials, especially the cubic fluorite-type ceramics.

Chapter 4 examines fuel cell operating principles, classification and materials before addressing electrode morphologies and how they relate to the effective reaction area or the triple phase boundary length (TPB).

The remainder of this thesis relates to investigations of the PEVD process as applied to SOFC's during the current study. Chapter 5 is a summary of the experimental methods, while Chapter 6 catalogues the results obtained and discusses their implications. Finally, Chapter 7 summarizes the significant results and conclusions which can be taken from this morphological, chemical and electrochemical investigation.

The exceptionally high melting temperatures typical of ceramic materials preclude the use of traditional liquid phase forming methods (casting, injection molding, etc.) common in metals and polymers processing. Alternative strategies are therefore necessary for the fabrication of ceramic wares. For the most part, ceramic processing has taken place in the solid phase, with most techniques using a chemical precursor (with a low decomposition temperature or a high vapour pressure) to significantly lower the processing temperatures. Poor sintering behaviour and irregular particle size distribution are the primary factors causing a majority of ceramic defects, although serious problems also arise as a result of byproduct entrapment, rearrangement and local melting.

The desire for thin ceramic membranes with specific properties, such as high density or constant porosity, amplifies an already complex problem. In the case of some electrochemical devices, the performance is dependent in large part upon the ionic resistance

of the electrolyte. It is recognized that by reducing the thickness of the solid oxide electrolyte layer in fuel cells to a level of approximately 10-50 μm , the ionic resistance can be significantly reduced and, thus, the performance of these devices is enhanced (Sasaki et al., 1993; Mineshige et al., 1995). This places considerable limitations on the manufacturing processes that are available for ceramic materials.

Serious developmental efforts were made between 1962 and 1970 to develop commercial solid oxide fuel cell power generating systems. Specifically, several processes were studied to produce thin, crack and pore free electrolytes. Chemical vapour deposition successfully performed on dense substrates was unsuccessful on porous substrates, as the films were not gas tight. Electron beam deposition had similar difficulties on porous substrates. On the other hand, r.f. sputtering was very successful on porous substrates, but growth rates were exceedingly slow (typically $< 1\mu\text{m/hr}$). Other methods available, such as sol-gel, were only in their infancy or were incapable of depositing thin enough films. In 1970, with no practical fuel cell foreseen, development contracts were cancelled. Difficulties producing dense and crack free electrolyte and interconnection materials, especially in their overlap areas, were cited as the primary factor hampering the development of a commercially feasible fuel cell (Feduska and Isenberg, 1983).

Since then, thin film technologies have made great strides in advancing microelectronic technologies through improved material properties and miniaturization (Yoshida and Toda, 1989). The dizzying array of processes and the variations thereof now available are almost as numerous as the papers written on them. The result is a renewed interest of SOFC's, as the electrolyte reaction that is no longer severely limiting performance (Boukamp, 1993). The focus of research is now aiming to improve electrode performance, as the electrode reactions now have the largest polarizations in the SOFC reaction.

The goal of Chapter 2 is to outline the membrane processing routes important to SOFC electrode manufacturing and to describe in detail those processes closely related to the PEVD process. Two divisions are used in this chapter to describe membrane processing: thick ($\geq 100\mu\text{m}$) and thin ($\leq 100\mu\text{m}$) films. This is not a perfect description though, as some thick film processes, such as colloid deposition, have demonstrated that they can be used to deposit very thin ($\sim 10\mu\text{m}$) films (de Souza et al., 1997b). A better description may be that thick films are deposited from powder form and thin film processes involve a vapour or a pseudo-vapour phase (in the case of sputtering).

2.1 Thick Film Processing

Typical thick film processes involve the production of a powder that is applied to the substrate in the form of a slurry or suspension, etc., and then sintered. Refined powder preparation techniques have led to improved quality and reliability of ceramic parts, due in large part to an increased emphasis on chemical preparation methods. Commercial powders are now available that possess reduced sintering temperatures, increased flexibility and consistency resulting in better overall properties in the final product. An increase in the knowledge of the effects of sintering aids, grain growth and sintering variables, cannot be overlooked for their role in improving material densities to greater than 99% (eliminating open porosity) (Brook, 1989).

Nonetheless, improving powder properties remains the most important factor in improving the final properties of the ceramic component. Powders with wide size distributions tend to result in mesoporosity where the large particles are clustered as seen in Figure 2.1, whereas clusters of small particles can result in localized high dimensional shrinkage that produces stress in the surrounding matrix. Unless the internal stresses can be relieved by shear deformation (i.e. creep), a significant reduction in densification rates occurs and may exacerbate the development of deleterious crack-like voids (Chu et al., 1989; Julbe et al., 1993).

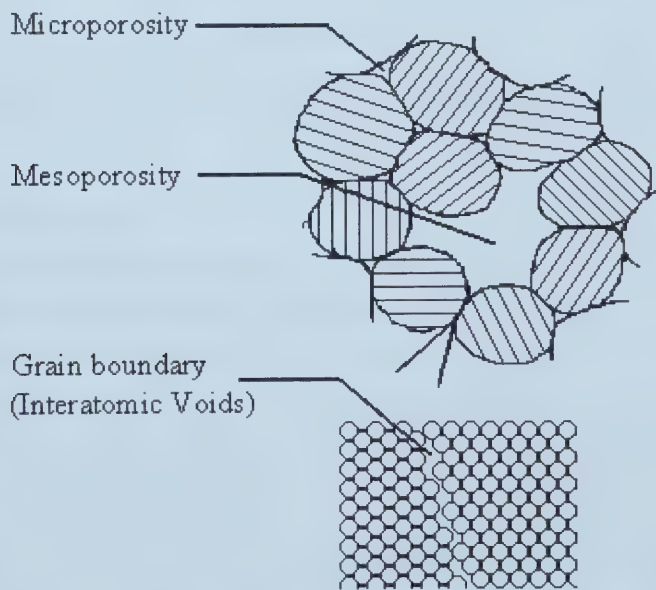


Figure 2.1 - Common porosity effects in ceramic materials (Julbe et al., 1993).

Non-uniformities are part of the nature of the powder and vanquishing them represents a serious obstacle to accomplishing both high density and constant porosity ceramic parts. In the absence of electrostatic or steric repulsions, attractive van der Waals forces between clean solid particles cause agglomeration in powders, whether suspended in liquids or dried at temperatures of less than 100°C. In short, perfectly dispersed powders are the exception rather than the rule. All processing steps must therefore be modified to reduce the fluidity and time available for the growth of flocculants. Figure 2.2 illustrates the particle size distribution attained with oven and microwave drying techniques (Kendall et al., 1990; Kabanova et al., 1992).

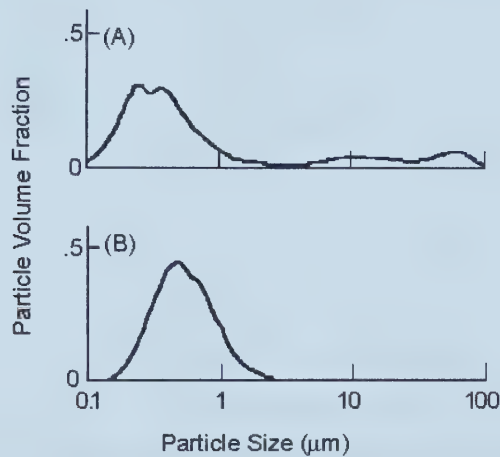


Figure 2.2 - Particle size distribution after (A) oven drying at 80°C and (B) centrifuging and microwave drying (Kendall et al., 1990).

2.1.1 Powder Production

Conventional Ceramic Processing. Mechanical methods, such as stirring in water, ultrasonic agitation, ultrasonic probe disruption or ball milling, are used to produce the powder in conventional ceramic processing. The ceramic materials are simply mixed together and ground to reduce the quantity of agglomerates. The degree of success of the four methods listed above are illustrated in Figure 2.3. As can be seen, the only way to break down large agglomerates is by ball milling in a solvent for several days. The relative inefficiency, relatively large particle sizes (~1 to 1000 μm), the possibility of contamination by grinding media and the possibility of a particle size distribution that is too broad (sieving and hydrocyclones can reduce this problem) are the most severe problems associated with mechanical powder production (Kendall et al., 1990).

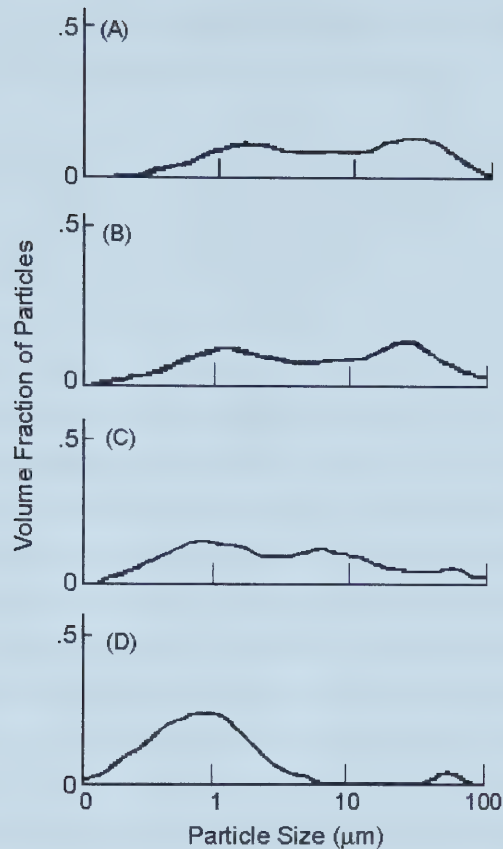


Figure 2.3 - Effect of mechanical methods on the breakdown of agglomerates by (A) stirring in water, (B) ultrasonic agitation, (C) ultrasonic probe disruption and (D) two days of ball milling in water plus lignosulphonate dispersant (Kendall et al., 1990).

Precipitation Powder Processing. In precipitation powder processing, precursors such as nitrates (Trubelja and Stubican, 1991), oxychlorides (Duh and Lee, 1989) or even oxides (Lambert Bates et al., 1986; Kutty and Raghu, 1992) are dissolved into solution. The powder is precipitated by allowing the dissolved ceramic to drip into a solution such as ammonium hydroxide, by adding the precipitation solution to the dissolved ceramic, or by drying the solution. Any chemical precursor can be used as long as it can be dissolved into and recovered from solution, and can easily be converted into the desired compound. If there are two or more ceramic materials involved in a solid solution, they can be precipitated simultaneously, or co-precipitated. The powder is then washed to remove any impurities, which may cause problems later, and allowed to dry before any subsequent steps are carried out. Narrow

powder size distributions can be attained providing strict controls on the process conditions, including the pH and solution concentrations, are maintained.

Colloidal Suspensions. Strict control of critical powder characteristics, including chemical homogeneity, small particle size, and narrow size distribution are attained with the use of colloidal suspensions. Although this process has close similarities with sol-gel and precipitation powder processing, the precursor will not form a gel and it is never dissolved into solution. Instead, the colloid is suspended in a liquid solution through the manipulation of interparticle forces with a suitable combination of surfactants. Surface active agents break apart weakly bonded agglomerates, eliminate strongly bonded agglomerates by sedimentation or centrifuge, fractionate desirable particle size distributions, eliminate inorganic and organic inclusions of a given size, homogeneously mix two or more powders, store powder slurries without mass segregation and consolidate powders to very high bulk densities. Ultrasonic vibration can also be used to further break up powder agglomerates (Kellett and Lange, 1990).

Comparisons of droplet and oxide particle sizes show that, depending on the concentration of metal ions in the starting solution, about 2 to 500 droplets have to exchange their contents to obtain oxide particles of about 30 nm (Sager et al., 1993), even though the solutions are up to 60 vol% solids (Kellett and Lange, 1990). This explains the tight powder size control achieved with this process. It also has the advantage of lower transition temperatures from amorphous precursors to the crystalline state than those required in conventional powder routes (Sager et al., 1993). The disadvantages are one dimension is limited, as the chemical precursor must be eliminated, and there can be a high residual impurity content.

Sol-Gel. The sol-gel process has many advantages over other powder processing routes, including greater purity and compositional control, shorter sintering times at lower temperatures, ability to produce amorphous solids outside the compositional range of normal glass formation, scalability and the possibility of producing specialized products (films, fibres, bulk monolithic structures, heterophasic composites and powder). This versatility is available thanks in part to the myriad of fabrication techniques available to sol-gel, such as slip casting, slurry coating, tape casting and spin coating (Budd et al., 1985; Oishi et al., 1993; Hirano et al., 1995; Mahia et al., 1996). As with colloidal suspensions, one dimension is limited, as the chemical precursor must be eliminated, and there can be a high residual impurity content. Organic precursors can be burned out with heat treatments over 400°C (Oishi et al., 1993),

but metal salt precursors cannot be removed in this manner. Thus, salt precursors are normally only used for producing powders (Bourell et al., 1993).

As with the colloidal route, a metal salt or a hydrated oxide is reacted with excess water. A precipitate of gelatinous hydroxide particles is obtained. This is then peptized with electrolytes which may then lead to a stable colloidal suspension. The particle size in the sol is dependent on the process parameters. Very small elementary particles are bound in larger aggregates (up to 1 μm). With appropriate treatment, the aggregates can be broken down to a few nanometres (Julbe et al., 1993).

Gels are formed by partial hydrolysis of a mixed solution of aqueous (metal salt) or organic (alkoxides) solvents followed by polymerization, further hydrolysis and polycondensation to form inorganic polymers composed of M-O-M bonds along with water and alcohol byproducts. In multicomponent oxide systems, if the hydrolysis rates of the M-OR bonds are different from one another, then element segregation can occur (Hsueh et al., 1991; Hirano et al., 1995). The sol-gel transition consists of clusters growing through condensation reactions, until these clusters collide and connect into a three dimensional network, producing a gel (Julbe et al., 1993; Brinker et al., 1994).

Sol-gel systems are very complex, with a number of factors having an effect on the quality of the resulting film. The choice of precursors is dictated by the reactivity, solubility, viscosity, organic content, decomposition temperature, by-products, cost and availability (Julbe et al., 1993; Brinker et al., 1994). Improved porosity gels are obtained by the addition of higher levels of hydrolysis water, but this can compromise the stability of the gel (Lijzenga et al., 1991). The addition of acids can refine the size of the primary particles to the nanometre range by peptizing the larger particles in an uncharged system. The particles become positively charged by proton adsorption, causing them to repel one another. This results in sols with more stability and smaller particle sizes as observed in Figure 2.4 (Anderson et al., 1988).

2.1.2 *Thick Film Application Methods*

Screening, Dipping, Spraying and Spin Coating. Once the powder is in liquid form, several techniques can be used to apply it to the substrate. Gels, slurries, suspensions, or even a simple powder-carrier-binder mixture can be used to apply the film to the substrate by means of dipping, spin coating, spraying, screening or even hand painting with a brush. In screen printing, the slurry or paste is applied to the substrate through a screen. The primary steps of this method are mixture preparation, screening-spraying-dipping-spinning, drying and sintering

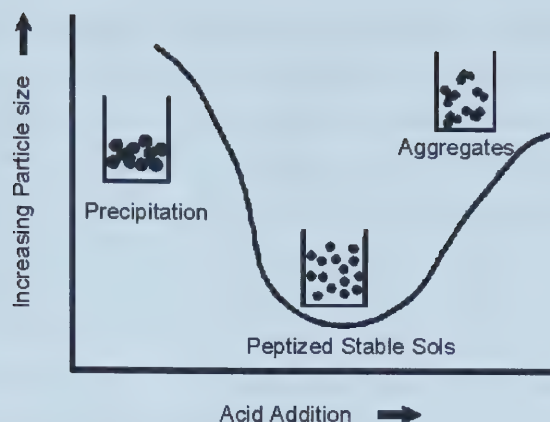


Figure 2.4 - Effect of acid concentration on particle size in sol-gel synthesis (Anderson et al., 1988).

(Sammes et al., 1994).

The slurry must have good consistency to flow over the desired substrate area. If it is too thick, it may not cover the area in a consistent thickness. On the other hand, if the viscosity is too thin, it may permeate through to parts of the substrate that a coating is not desired. The expected advantages of these technique are their simplicity and low cost. However, the disadvantage is that it may only be possible to deposit films on substrates with simple geometries. In the case of screen printing, the substrate must be perfectly flat (Labrincha et al., 1993).

Tape Casting. Tape casting is a very attractive technique, as it may be possible to complete an entire electrochemical device in one sintering process. This is a very complex process, however, as the electrolyte and interconnect must be pore and crack free, while maintaining a porous electrode structure. Of paramount importance is maintaining equal shrinkage behaviour of each layer (Kawada et al., 1992b).

In this process, a stable slip is created by mixing the powder in a liquid containing binders, plasticisers and dispersants, etc., for several hours. The slip is spread over a flat surface allowing the solvent to dry off and the powder and binders form a ceramic tape. In the doctor blade technique, the flat surface is a carrier belt which is constantly fed from a slip chamber. The belt passes under carefully adjusted blades which level off the top and the cast slip is “doctored” to a predefined level. The layer of slip dries as it passes through the apparatus and is removed from the belt for further processing (Cannell and Trigg, 1990).

Electrophoretic Deposition. Electrodeposition is better known for electroplating metal coatings on substrates. Electrophoretic deposition differs from electrolysis in that the moving species is a solid particle (usually a colloid or suspension) instead of an ion. There is no charge transfer on deposition and a higher deposition rate is attained in comparison with electroplating (1 mm/min compared to 0.1 $\mu\text{m/min}$). Electrophoresis can deposit films in two distinct manners: either by adding an oxidizing agent to the solution to oxidize metal ions out of solution and form oxides or by the motion of particles in a colloidal solution or suspension in an electric field. To minimize forming times the applied voltage is much higher than that used in biological electrophoresis, resulting in fewer variations of electrophoretic mobility from one particle to another due to particle size differences (Heavens, 1990).

In electrophoretic deposition, the particles do not immediately lose their charge on being deposited. In fact, a reversal of the electric field will strip off the deposited layer. When phases come into contact, some redistribution of positive and negative charges can occur, leading to the formation of an electric double layer through one or more of the following mechanisms:

- Selective adsorption of ions onto the solid particle from the liquid phase,
- Dissociation of ions from the solid phase into the liquid,
- Adsorption or orientation of dipolar molecules at the particle surface, and
- Electron transfer between solid and liquid phases due to differences in work function.

In the case of ceramic and glass particles, the last mechanism is inapplicable but the first two invariably occur. Stable suspensions show little tendency to flocculate and settle slowly, forming dense, strongly adhering deposits. The function of the electric field is to drive the particles towards the electrode and exert pressure on the deposited layer (Heavens, 1990).

The preferred solvent of choice is organic-based, as the electrolysis of water occurs at low voltages and in addition to efficiency losses, etc., bubbles can be trapped within the deposit preventing full densification. Although organic liquids have lower dielectric constants, and thus lower zeta potentials as a result of lower dissociating power, higher field strengths can be used since the problems of electrolytic gas evolution at the electrodes are greatly reduced. The high current densities which are then necessary can result in Joule heating and degradation of the electrodes, contaminating the deposit. Isopressed graphite/clay or graphite/cement are commonly used for electrodes to overcome these problems (Heavens,

1990).

Plasma Spray Deposition. Very few application processes are available to liquid ceramic materials as discussed in the introduction, because of the difficulties involved in attaining and maintaining the high temperatures involved. Thermal spray, which deposits films by heating a charge of powder and propelling it towards the substrate in a liquid, or at least a partially liquid, state, is by far the most common liquid phase ceramic membrane process. Plasma spray is the most well known and industrially developed thermal spray technique, with a suitably high materials throughput for large scale production rates. Laser spraying has recently been tested and will also be discussed.

In the plasma spray system, powder is injected into a plasma stream of gases (usually argon, hydrogen, nitrogen or helium) ionized with an electric arc. Upon injection into the plasma stream, the powder is melted and accelerated towards the substrate. If a sufficient amount of the particles are melted and the velocity is great enough to cause the molten particles to spread out and flow when they impinge upon the substrate, dense high strength deposits are achieved. Because this is a liquid phase process, a strong inter-particle bond and particle substrate bond is realized, resulting in dense, adherent films (Nicoll, 1992).

High heating and cooling rates inherent in this process can lead to severe thermal shock of the substrate and/or the film. In addition, ultrathin films, which are necessary for electrochemical applications, are difficult to attain with this process (Eguchi et al., 1991). Recent studies by Schiller et al., 1997, applied plasma torches with specially developed Mach 3 Laval nozzles in d.c. vacuum plasma spraying. Very thin, gas tight zirconia films and porous electrode layers with graded composition and porosity in transition regions were attained in this fashion. Increased velocities and higher resulting kinetic energy for the particles on impact with the substrate lead to greater particle spread and thinner films. Also, the lower radial temperature and velocity gradients and a jet core with high temperature and velocity values which is more extended, results in good melting conditions for a greater amount of particles. Denser and more homogeneous films are attained with higher deposition rates.

Laser Spraying uses a high power density laser directed parallel to the substrate surface. Powder, supplied with an extra high accuracy supply device, passes through the laser and adheres to the substrate surface. The closed system allows for a reacting gas, inert gas or vacuum environment. An auxiliary laser beam can be used for substrate heating or for heat treating the depositing film (Tsukamoto et al., 1990).

This process allows liquid phase deposition of high temperature materials with a high purity and minimal damage to the substrate. High melting point materials can be coated on low melting point materials with this technique. However, to coat large areas, a very large and hence very powerful laser is needed. Also, the maximum powder feed rate is limited by the ability of the laser to melt all of the powder which passes through the beam. Finally, the material which is being deposited must be able to absorb the laser light (Tsukamoto et al., 1990).

2.1.3 Sintering

Sintering is a complex and unavoidable step involved in the deposition of thick films, and as such, cannot be avoided in this discussion. It is however, too complex a subject to review in such a short section, and as such will only be discussed in relationship to the effect it has on the final product, whether as a dense or a porous membrane.

Porosity is generally not defined by a spatially extensive crystalline lattice; thus, strategies designed to control porosity often rely on managing the packing efficiency of polymers or particles during gelation and aging and their extents of collapse upon drying. Random dense packing of monosized spherical particles always results in about 33% porosity, independent of particle size. Virtually all packing concepts utilize particles that are packed together to create pores of a size related to the primary particle size. Since it is not yet possible to avoid some distribution of particle sizes, the current state-of-the-art is to create particles with quite narrow particle size distributions that are more or less randomly close-packed into a membrane configuration without aggregation, which leads to a second class of larger pores. The advantage of this approach is that the pore size of the membrane is dependent on the particle size (Brinker et al., 1994).

To arrive at small pore sizes, appropriate for gas separation applications, for example, it is necessary to prepare smaller particles. However, avoidance of cracking essential for membrane performance may be a fundamental limitation of the particle approach to the preparation of gas separation membranes. The removal of liquid during the drying process creates a tensile stress along the surfaces of the membrane that results in cracking as follows:

$$\sigma_T = \left[\frac{E}{1 - \nu} \right] \left[\frac{f_s - f_r}{3} \right] \quad (2.1)$$

where E is Young's modulus (Pa), ν is Poisson's ratio, f_s is the volume fraction of solvent at the gel point and f_r is the residual solvent in the fully dried film. The result is that cracking is

more likely to occur in particulate membranes as the particle size is reduced. As the particle radius is reduced, the particle solubility increases according to the Ostwald-Freundlich equation:

$$S = S_o \exp \left[\frac{2\gamma_{SL} V_M}{RTx} \right] \quad (2.2)$$

where S_o is the solubility of a flat plate, γ_{SL} the solid-liquid interfacial energy, x the particle radius and V_m the molar volume of the solid phase. As the particle size is reduced, S increases dramatically; thus, in many liquid environments, nanosized particulate films are inherently unstable (Brinker et al., 1994).

Dense structural ceramics formed by commercial sintering processes generally result in a residual porosity on the order of 2 to 6%, which can have several deleterious effects. Voids formed near the surface can interact with surface cracks created during machining or surface finishing to produce fracture-limiting flaws. Elimination of near-surface voids should have a beneficial influence on contact fracture (Drory and Evans, 1985). In the case of thick films, this amount of porosity is unacceptable, especially in solid electrolyte applications. Gas leakage can cause loss of efficiency, in the case of solid oxide fuel cells, and a decline in accuracy, in the case of gas sensors.

The trends suggest that void distributions are essentially lognormal and stationary. Specifically, the mean void size varied little with heat treatment, but the overall number of voids continuously diminished as the heat treatment proceeded. Furthermore, the behaviour of the intra- and intergranular voids was indistinguishable (Drory and Evans, 1985). The usual relatively small sintering potential causes large pores to shrink very slowly, caused by grain boundary tractions as illustrated in Figure 2.5. An expected rapid increase in the densification and pore removal rates occurs when the pore size becomes in the order of the grain size because of an increase in chemical potential gradient. Hence, grain growth during sintering may exhibit an instantaneous beneficial influence upon densification (Evans and Hsueh, 1986).

Sintering Aids. In Figure 2.6, it can be seen that the extent of densification of zirconia is dependent on the additive content. As far as the sintering temperature is concerned, the sintering behaviour could be divided into two categories. At low temperatures below 1300°C, the MgO addition acts to retard densification. The sintered density decreases with MgO addition. On the other hand, the sintered density increases with increasing MgO contents at 1350°C and above. The MgO doped Y-TZP (yttria - tetragonal zirconia polycrystals) would

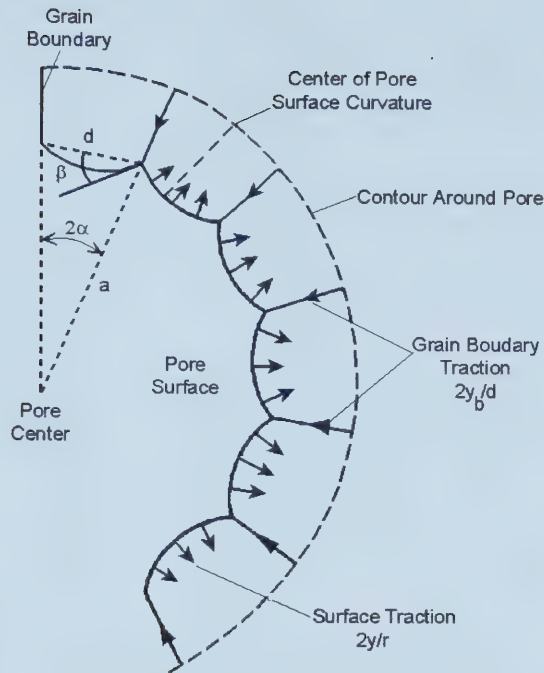


Figure 2.5 - Grain boundary traction of a large pore in a polycrystal (Evans and Hsueh, 1986).

achieve nearly 100% of theoretical density at 1400°C for 3.5 h with 0.5 mol% MgO dopant. It is interesting to point out that the densification process of the undoped sample appears to cease at 1400°C (Duh and Hwung, 1988).

Observations of the microstructure of doped Y-TZP made it apparent that the MgO dopant was reducing the grain size of the sintered body. The open porosity of the undoped Y-TZP is identical to that of the doped samples after sintering at 1500°C. The sintered density of the undoped Y-TZP is, however, lower than that of the MgO doped. An SEM micrograph also shows that, in the undoped Y-TZP specimen, there are few intergranular pores observed. The pores are trapped in the grains of the undoped Y-TZP because of fast grain boundary mobility. These pores are difficult to eliminate, and thus the undoped Y-TZP fails to reach complete densification. On the other hand, for the MgO doped sample, the pores adhere to the grain boundary because of the low boundary migration rate. Pores can thus be eliminated by grain boundary diffusion, and full densification could be achieved (Duh and Hwung, 1988).

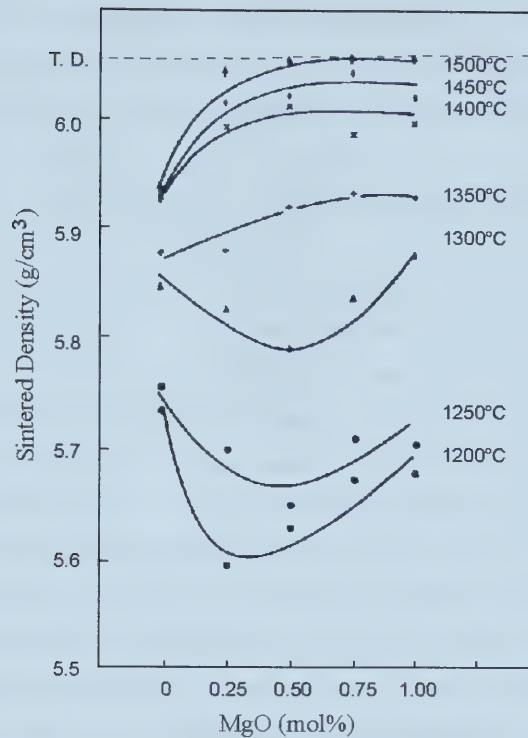


Figure 2.6 - Sintered density of Y-TZP as a function of MgO content (Duh and Hwung, 1988).

Plasma Enhanced Sintering. The use of plasma to assist in sintering ceramic materials was first carried out in 1968 by Bennet et al. With the use of microwave induced plasma discharge at various pressures, a range of oxides was found to have smaller grain sizes and greater densification compared with samples conventionally sintered at the same temperature, time and atmospheric conditions. Thus films can be sintered at much lower temperatures with similar density results (Metaxas and Binner, 1990).

Plasmas can be generated by d.c. devices, radio frequency induction or by microwaves. Microwaves have the following advantages over d.c. and r.f. induced plasmas (Metaxas and Binner, 1990):

- A microwave-induced plasma produces a much higher degree of ionization and dissociation which provides a field of active species 10 times higher than electrically excited plasma.
- The range of pressures in which plasmas can be created with microwaves, typically 10^{-5} torr to several atmospheres, is much

greater, broadening the range of applications.

- The electron to temperature ratio is very high, allowing the carrier gas and substrate to remain moderately cool even in the presence of high electron energy.
- Internal electrodes are a source of impurities and are unnecessary in microwave induced plasmas.

The lack of internal electrodes also has the added benefit of a simplified system design.

Very high sintering rates are observed with microwave plasma enhanced sintering (up to 99% of theoretical in 2 min and up to 99.9% of theoretical in 10 min). The exact reasons for the observed benefits that plasma enhancing provides are not well understood. It is speculated that the very high temperatures attained ($>1900^{\circ}\text{C}$) combined with high heating rates (up to 100°C/s) enhance grain boundary and lattice diffusion, leading to densification without increasing surface diffusion which leads to grain coarsening. The possibility that the plasma interacted chemically with the particle surfaces to enhance densification has also been considered. Although this theory has largely been discounted, the presence of plasma etching has been suggested as evidence of non-thermal effects. There is a widespread feeling among researchers that microwaves may result in improved densification through reductions in activation energies (Metaxas and Binner, 1990).

2.2 Thin Film Processing

2.2.1 Sputtering

The sputter deposition process involves the removal of atoms from the surface of a solid or liquid target by energetic ion bombardment and the collection of those same atoms on a solid surface or substrate. The target is held at a negative potential ranging from a few hundred volts to a few kilovolts. The chamber pressure must be maintained between 10^{-3} and 1 Torr for the voltage to cause a discharge in the vicinity of the target. The target, because of its negative potential, is bombarded by the ions in the plasma. Argon because of its higher atomic number and non-reactivity, is the most commonly used sputtering gas. The discharge is sustained by the stochastic ionization of the gas atoms by the secondary electrons emanating from the target. The bombardment of the target leads to sputtering of the target surface by a momentum transfer process. This deposition process is represented schematically in Figure 2.7 (Budhani and Bunshah, 1990).

Increasing the ion density in the vicinity of the target increases the sputtering rate. This increased ion density can be realized by the introduction of a magnetic field, commonly known

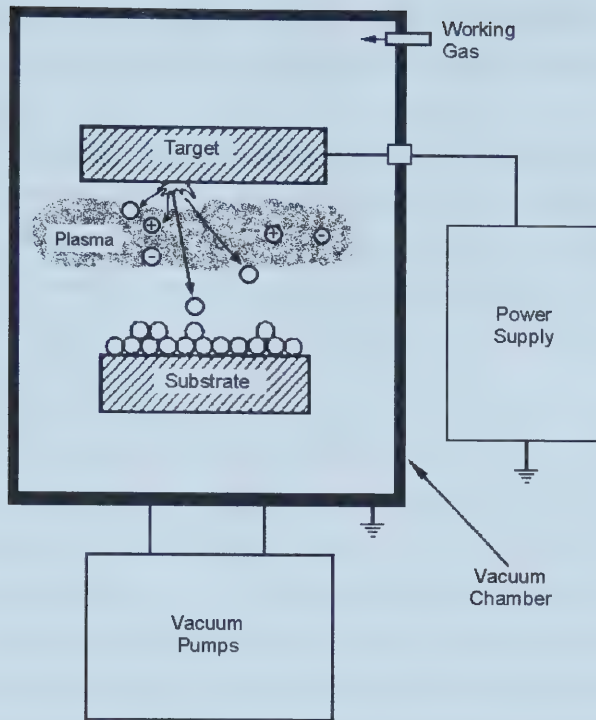


Figure 2.7 - Schematic representation of the sputter deposition process (Budhani and Bunshah, 1990).

as magnetron sputtering. Electrically conducting targets allow the use of d.c. voltages for sputtering; however, in the case of electrically insulating targets, a radio frequency (r.f.) potential must be applied (Budhani and Bunshah, 1990). R.f. magnetron sputtering is commonly used, although it is not without fault. Difficulty arises in precisely controlling film stoichiometry and substrate materials are damaged by bombardment of high energy particles, especially organic substrates (Mansingh and Kumar, 1988; Maiwa et al., 1993).

Reactive Sputtering. The dissociation of the target material into atoms and molecular fragments can result from the bombardment, resulting in a deficiency of the gaseous constituent of the material. The problem of non-stoichiometry can be minimized if some of the constituent gas is added to the plasma with the argon. Although a wide range of ceramics have been deposited by this method, it still suffers from the following disadvantages (Budhani and Bunshah, 1990):

- Ceramic targets with poor thermal conductivity do not allow effective cooling during sputtering, resulting in local hot spots, consequent

spitting of the material and the formation of particulates in the film. Also, massive cracks can develop on the ceramic targets on prolonged usage.

- Multicomponent targets can demonstrate preferential sputtering of one or more of the components, resulting in off-stoichiometric films.
- The reactive gas can poison the sputtering target, especially in oxygen environments. Target-gas-plasma interaction during sputtering leads to the formation of compound layers on the target, slowing the sputtering rate.

Reactive magnetron sputtering is a high rate alternative to r.f. sputtering, which has been used more often for SOFC components. Deposition rates have been reported as high as 9 $\mu\text{m/h}$, but the most important advantage in the use of reactive magnetron sputtering for thin films is the ion irradiation of the film during deposition. Ion irradiation of the film is crucial for obtaining high density films at low temperatures (350°C); therefore, thinner films with a higher density and adhesion strength can be obtained with higher deposition rates and materials utilization efficiency in comparison with r.f. sputtering (Wang et al., 1992; Barnett, 1990). For these reasons, the d.c. reactive magnetron sputtering technique is expected to give stable and adherent electrode layers, with a narrow grain and pore size distribution and without the formation of unwanted reaction products with the substrate. Unfortunately, the process is expensive and Labrincha et al., 1993, were not successful in obtaining LSM thin films by the sputtering technique, due to intrinsic magnetic properties of the material. They were, however, successful in obtaining thin films of cobalt-based perovskite electrodes.

The total gas pressure of the system during deposition can have adverse affects on the final properties of the film. The optimum operating conditions for fully dense YSZ thin films were determined by Wang et al., 1992: a pressure between 4 mTorr and 20 mTorr and a substrate temperature of 350°C. At pressures above 20 mTorr, a crack network was discovered from SEM images.

Other Sputtering Systems. There are many sputtering systems that have been used with some success. Ion beam sputtering, for example, utilizes a beam of inert gas ions generated from an ion source to bombard the target. Neutral beams can be used for electrically insulating targets. The sputtered species are deposited on a substrate which is situated in a relatively high vacuum. The reactive gas is either introduced directly into the discharge chamber of the ion gun or a separate gun may be used for compounds with different

sputtering rates (Budhani and Bunshah, 1990).

Electron cyclotron resonance is another example of the myriad of sputtering processes available. A magnetic field (875 G) is generated and microwaves (2.45 GHz) are introduced into the plasma chamber through a quartz window. The plasma generated by the ECR condition is transported toward the substrate stage by the gradient of the magnetic field. Cylindrical targets are arranged so that they encircle the plasma stream. Toyama et al., 1994, associated an increase in microwave power (up to 300 W) with an increase of the deposition rate of $\text{Pb}(\text{Zr},\text{Ti})\text{O}_3$ from 2.1 nm/min at 150 W to 3.9 nm/min at 300 W. Deposition rates are up to four times that achieved with r.f. sputtering (Masada et al., 1991; Toyama et al., 1994).

2.2.2 Vapour Phase Deposition

The deposition of thin films by vacuum evaporation consists of the following steps (Maissel and Glang, 1970):

- Transition of a condensed solid or liquid phase into a gaseous state,
- Vapour traversing the gap between the evaporation source and the substrate at reduced gas pressure, and
- Condensation of the vapour on the substrate.

The theory of vacuum evaporation includes the thermodynamics of phase transitions from which the equilibrium vapour pressure of materials can be derived, as well as the kinetic theory of gases which provides models of the atomistic processes.

Relatively few inorganic compounds, alloys or mixtures evaporate congruently. As a consequence, except for elements the composition of the vapour, and hence of the condensate, is not the same as that of the source material. In principle, compositional changes associated with the vaporization can be predicted from thermodynamics, but in practice the available thermochemical data are rarely sufficient to describe quantitatively the complex processes which may occur. Empirical information, although far from perfect, is the most reliable guide in determining the experimental conditions necessary to produce films of the desired composition. Special techniques such as reactive, two-source and flash evaporation are sometimes necessary to obtain the desired film composition (Maissel and Glang, 1970).

Evidence shows that the vaporization of compounds is usually accompanied by dissociation, association or a combination of both processes. Dissociation represents thermal decomposition and makes direct evaporation impractical. Deposition of compound films from a single vapour source requires that the material enters the gaseous state either in the form of complete molecules or, if dissociation occurs, that the constituents are equally volatile. The

degree of dissociation or association which some of these compounds shows is negligible for most practical purposes and barely affects the vapour pressure. Generally, the tendency to dissociate is greater the higher the evaporation temperature and the lower the pressure (Maissel and Glang, 1970).

Direct evaporation of ceramic materials is not practical in most instances, as the vapour pressure is much too low. There are, however, some techniques that can be used, such as laser evaporation (Craciun and Craciun, 1992) and electron beam evaporation (Yoshida and Toda, 1989). Yoshida and Toda, 1989, deposited Pb_2CrO_5 films using a magnetic field deflection-type e-beam as seen in Figure 2.8. The vacuum requirements for this technique are critical and the chamber was evacuated by a Ti-sublimation pump and a noble ion pump in addition to the use of intermittent deposition to maintain the high quality of the vacuum. Direct evaporation is very inefficient in ceramics and it is, therefore, more common to use a chemical precursor as in chemical vapour deposition and reactive pulsed laser ablation.

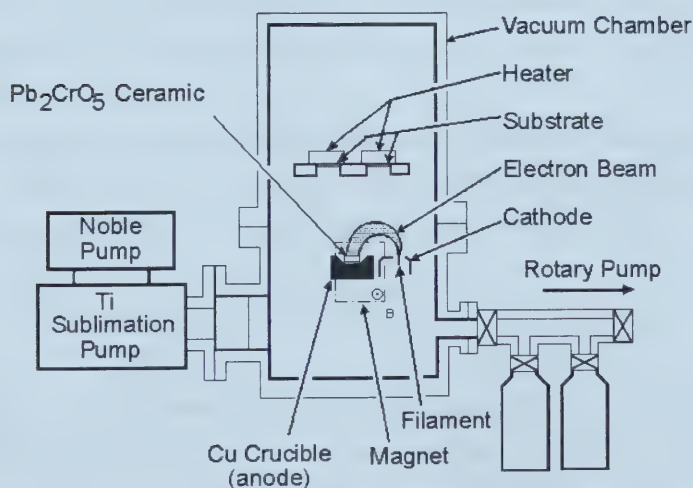


Figure 2.8 - Schematic diagram of the electron beam evaporation technique used by Yoshida and Toda (1989).

Vapour Pressure. Atomic theory and extensive experiments have shown that evaporation rates cannot exceed an upper limit which is proportional to the equilibrium vapour pressure. Therefore, the saturation pressure of a vapour over its condensed phase is an important quantity to assess the amenability of a substance to evaporation and the temperatures required to achieve practical transfer rates. Free energy determines the stability of one state relative to another. If there is no driving force between two states, they can coexist without a net change and, therefore, are at equilibrium. The vapour-solid or vapour-liquid equilibrium can be defined as an equality of the chemical potentials as follows:

$$\mu_c = \mu_g \quad (2.3)$$

where c and g identify quantities associated with the condensed and gaseous states, respectively. From the Clausius-Clapyron equation:

$$\ln(p^*) = \frac{\Delta H_e}{RT} + C_{\text{int}} \quad (2.4)$$

where C_{int} is a constant, p^* is the thermodynamic equilibrium pressure and ΔH_e is the molar heat of evaporation. If the pressure is known at a given temperature, then the equation at an unknown temperature can be set equal to it (cancelling the constants) to give an estimate of the vapour pressure (Zumdahl, 1989).

In order to omit the constant and use commonly published thermodynamic data, the molar volume of the condensed phase is neglected and the vapour is assumed to obey the ideal gas law, attaining the following equation (Maissel and Glang, 1970):

$$\frac{dp^*}{p^*} = \frac{\Delta H_e dT}{RT^2} \quad (2.5)$$

Equilibrium between the two states is established hypothetically in van't Hoff's equilibrium box by expanding (or compressing) both phases isothermally and reversibly. The two chemical potentials change until they become equal at the equilibrium pressure p^* . Introducing $\mu_g^\circ(T) - \mu_c^\circ(T) = \Delta G_e^\circ(T)$ results in the following relation (Maissel and Glang, 1970):

$$\log p^* = -\frac{\Delta H_e^\circ(298)}{4.575T} + \frac{\Delta S_e^\circ(298)}{4.575} + \frac{1}{4.575T} \iint_{T-298} \frac{\Delta C_p}{T} dT^2 \quad (2.6)$$

where

$$C_p = a \ln T + bT + cT^{-1} \quad (2.7)$$

If the specific heat functions are given as series for both the gaseous and the condensed state, the temperature dependence of the heat capacity change may be integrated resulting in the following relationship (Maissel and Glang, 1970):

$$\log p^* (\text{torr}) = AT^{-1} + B + C \log T + DT + ET^{-2} \quad (2.8)$$

where variables A through E are represented by the following equations:

$$\begin{aligned} A &= - \frac{\Delta H_e^\circ(298) - 298(\Delta a + 149\Delta b) + 3.35 \times 10^{-3} \Delta c}{4.575} \\ B &= \frac{\Delta S_e^\circ(298) - 6.70\Delta a - 298\Delta b + 5.6 \times 10^{-6} \Delta c}{4.575} + 2.8808 \\ C &= \frac{\Delta a}{1.987} \\ D &= \frac{0.5 \cdot \Delta b}{4.575} \\ E &= \frac{0.5 \cdot \Delta c}{4.575} \end{aligned} \quad (2.9)$$

Evaporation Rates. Investigations by Hertz in 1882 established that evaporation rates in a vacuum are proportional to the difference between the equilibrium pressure of mercury at the surface temperature of the reservoir p^* and the hydrostatic pressure p acting on that surface. He drew the important and fundamental conclusion that a liquid has a specific ability to evaporate and cannot exceed a certain maximum evaporation rate at a given temperature, even if the supply of heat is unlimited. Furthermore, the theoretical maximum evaporation rates are obtained only if as many evaporated molecules leave the surface as would be required to exert the equilibrium pressure p^* on the same surface while none of them must return. The latter condition means that a hydrostatic pressure of $p = 0$ must be maintained (Maissel and Glang, 1970).

Knudsen argued that molecules impinging on the evaporating surface may be reflected back into the gas rather than incorporated into the liquid. Consequently, there is a certain fraction $(1 - \alpha_v)$ of vapour molecules which contribute to the evaporant pressure but not to the net molecular flux from the condensed into the vapour phase. To account for this

situation, he introduced the evaporation coefficient α_v , defined as the ratio of the observed evaporation rate in vacuo to the value theoretically possible according to Hertz' equation. The most general form of the evaporation rate equation is as follows (Maissel and Glang, 1970):

$$\frac{dN_e}{A_e dt} = \alpha_v (2\pi mkT)^{-1} (p^* - p) \quad (2.10)$$

is commonly referred to as the Hertz-Knudsen equation where N_e is the number of atoms, A_e is the area of evaporation and m is the molecular weight.

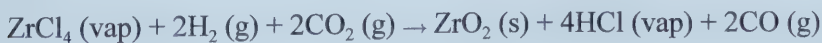
From a small quantity of mercury, Knudsen obtained values of α_v as low as 5×10^{-4} . Concluding that the low rates were attributable to surface contamination as manifest in the discoloured appearance of the metal, he allowed carefully purified mercury to evaporate from a series of droplets which were falling from a pipette and thus continually generating fresh, clean surfaces. This experiment yielded the maximum evaporation rate where α_v is equal to one and p is equal to zero. It was shown by Langmuir in 1913 that the Hertz-Knudsen equation also applies to the evaporation from free solid surfaces (Maissel and Glang, 1970).

2.2.3 Chemical Vapour Deposition

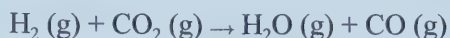
CVD is "a material synthesis method in which the constituents of the vapour phase react to form a solid film on some surface" - Vossen, 1978. A chemical precursor with a high vapour pressure migrates to the substrate, reacts with the carrier gas when heated by the substrate and the final product deposits on the substrate. Without the use of a chemical precursor, most ceramic materials could not be deposited from the vapour phase. In the deposition of zirconia films, for example, zirconium tetrachloride is utilized, as the sublimation temperature is a mere 331°C (604 K) compared with a melting point of 2680°C (2953 K) for the oxide (Powell et al., 1966).

There are many mechanisms possible for the deposition of oxides as coherent films. When the gases come in contact with the substrate, the vapours and gases react as follows (Powell et al., 1966):

1. Decomposition of the precursor vapours by thermal decomposition, exposure to an ionized carrier gas or by electron bombardment. Decomposition is carried out in an oxidizing environment with H_2O and CO_2 present to control the stoichiometry of the depositing film.
2. Hydrolysis of a metal halide vapour at a heated surface by the reaction:

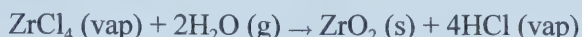


This produces, in effect, hydrolysis of the metal halide vapour by the water vapour formed by the water-gas shift reaction as follows:



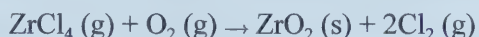
yet allows the halide precursor to transport to the substrate in a relatively inert H_2 and CO_2 atmosphere. The water-gas shift reaction has a free energy which ranges from +2.5 kJ/mol at 1000 K to -25.9 kJ/mol at 2000 K. The hydrolysis of ZrCl_4 ranges from -166.4 to -194.1 kJ/mol for the same temperature range.

3. Hydrolysis of a halide precursor with water vapour at a heated surface as follows:



This reaction is more thermodynamically favoured than the water-gas shift reaction at temperatures below 1000 K. However, the reactivity of halide precursors with water vapour makes it necessary to have separate streams to bring the water vapour and the halide and carrier gases to the substrate.

4. Direct oxidation of the halide with oxygen as follows:



This reaction has similar free energy to the water-gas shift reaction at 1000°C, but is much less favourable at 2000°C.

The gaseous byproducts are removed by means of a vacuum pump, which maintains a total pressure of approximately 0.1 Torr. This method, as illustrated in Figure 2.9, successfully deposits films of up to 10 microns thick on dense substrates (Powell et al., 1966).

The reaction process is thermodynamically spontaneous at temperatures below 800°C, but higher substrate temperatures are required to drive reaction kinetics (Belot et al., 1999). Plasmas are becoming increasingly common for decreasing the substrate temperature necessary for film deposition in CVD. The use of plasmas has been discussed in Section 2.1.3 and will, therefore, not be discussed here, except to point out that substrate temperatures as low as 200°C (Meng et al., 1991) have been attempted and dense, thin films successfully deposited at temperatures as low as 450°C (Cao et al., 1994).

Metal chloride precursors, although resulting in favourable membrane properties, have several problems associated with them. In addition to an increase in temperature to drive reaction kinetics, halides are extremely hygroscopic, require relatively high temperatures to vaporize them and, ultimately, form corrosive gas (HCl and Cl_2) byproducts, corroding the film, substrate and apparatus (Aizawa et al., 1993). The following precursor properties are desirable for chemical precursors in CVD (Sheshu et al., 1990):

- They should be stable in air, moisture and on prolonged heating,

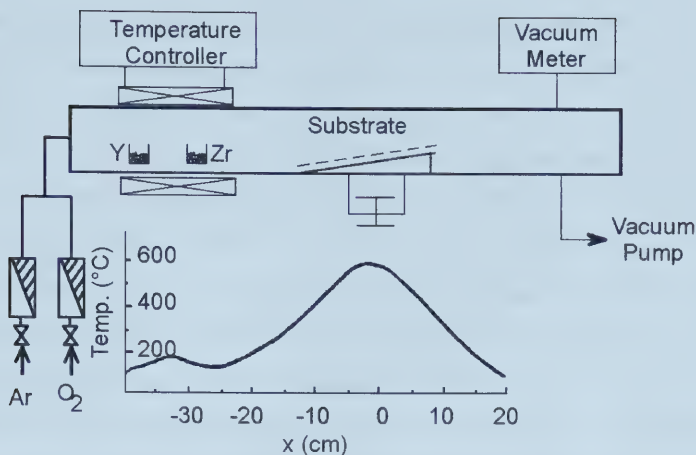


Figure 2.9 - Schematic diagram of the CVD process (Powell et al., 1966).

- They should have an appreciable vapour pressure (>0.1 torr) at low temperatures and pressures, and
- The final product must be of acceptable quality (i.e. purity, microstructure etc.)

Several organic compounds fit these requirements and the process is commonly referred to as MOCVD or Metal-Organic Chemical Vapour Deposition. The most prevalent classes of these organic compounds are the homoleptic β -diketonate and alkoxide complexes which have both enjoyed a measure of success. From these classes of precursors, zirconium and yttrium acetylacetonate ($\text{Zr}(\text{acac})_4$), dipivalomethane ($\text{Zr}(\text{dpm})_4$) and tetra-methyl-heptanedionates ($\text{Zr}(\text{thd})_4$), are most commonly studied and used. These compounds not only have a lower melting point, but reaction kinetics are sufficient for reaction on low temperature substrates. This results in more energy efficient film production, fewer reaction byproducts and a wider variety of substrate types (Meng et al., 1991; Dzjubenko, 1993).

Alkoxide precursors leave little residual carbon under pyrolytic and especially hydrolytic conditions, according to alkoxide chemistry. However, these highly branched alkoxides are unstable at the evaporation temperatures due to kinetically favoured elimination reactions producing olefin byproducts. Incomplete sublimation has been reported with as much as 15% residue (Belot et al., 1999). Using long carbon chain normal alkoxides provides stability against decomposition at evaporation temperatures. The presence of water vapour plays a critical role in the deposition reaction of alkoxides. These compounds can be highly hygroscopic and, if the hydrolysis reaction is given sufficient opportunity to occur in the

vapour phase, the hydrolysis-polycondensation reaction may be present. Consequently, the deposition rate will show a dependence not only on the partial pressure of the alkoxide precursor, but also on the partial pressure of the water vapour (Chour and Xu, 1997).

Thd precursors, which are among the β -diketonate metal-organic compound class, are nontoxic, environmentally benign, stable and sufficiently volatile to allow processing with substrate temperatures as low as 450°C. Sublimation temperatures of 140 to 160°C are used for yttria and zirconia precursors, as higher temperatures created complicated dependence between mass losses and temperature indicating the existence of a minority mechanism such as degradation or oligomerization (Dubourdieu et al., 1999).

Growth rates using thd precursors have been as high as 0.7 $\mu\text{m}/\text{min}$ with good compositional control of yttria stabilized zirconia (Dubourdieu et al., 1999). At low deposition temperatures ($<770^\circ\text{C}$), both the surface roughness and growth rate are low. A small increase in the temperature dramatically increases the deposition rate and growth along the direction of the corners would be favoured. The dependence of the deposition rate with temperature (a linear relationship in a $\ln(\text{rate})$ vs. $1/T$ plot) reveals that the deposition kinetics is reaction controlled with an activation energy of 48 kJ/mol (Garcia et al., 1995).

2.2.4 *Electrochemical Vapour Deposition*

The electrochemical vapour deposition process (EVD) was first conceived and developed by Isenberg in 1970, while working for the Westinghouse Electric Corporation (Feduska and Isenberg, 1983). Although this method has been used extensively for depositing stabilized zirconia membranes, it has also been applied to systems of doped cerium oxide (Tanner and Virkar, 1994), lanthanum chromate (Kawada and Yokokawa, 1997) and doped indium oxide films (Carolan and Micheals, 1990a). The remainder of this section will focus on the yttria-stabilized zirconia system, as most of the literature deals with this system and this is the principal area of interest.

EVD is a modified form of chemical vapour deposition where the $\text{O}_2/\text{H}_2\text{O}$ mixture is separated from the reactant metal chlorides by a porous substrate. An electrochemical gradient between the chloride and the oxygen chambers pushes the reaction and produces a non-porous film. For the technique to be successful, the film being deposited must have a combination of both ionic and electronic conductivity. These films display a uniform thickness due to the electrochemical potential gradient that drives film growth. In other words, where the film is the thinnest, the driving force is the greatest (Schoonman, 1991).

The EVD process consists of two steps which are illustrated in Figure 2.10. The first

step is a pore closure or chemical vapour deposition stage, as the two reactant gases are allowed to interdiffuse within the substrate pores. Reaction carries on in the pores, forming the corresponding solid oxide product on the pore wall until finally all of the substrate pores are closed. At this point, the second step of the technique begins and it is now a scale growth or electrochemical vapour deposition stage. If the deposited solid oxide meets the conditions of electronic and ionic conductivity, the oxygen source reactant can diffuse through the oxide film and react with the metal source reactant leading to continuous oxide film growth (Schoonman, 1991; Han and Lin, 1994).

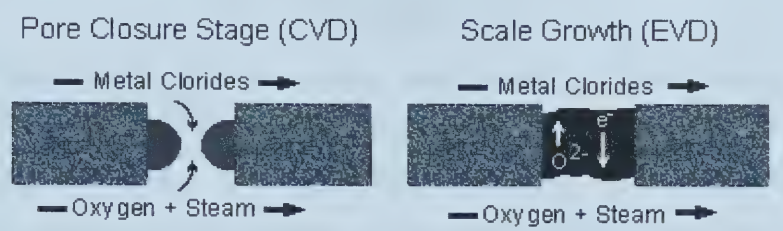


Figure 2.10 - The CVD and EVD steps involved in thin film formation on porous substrates (Schoonman et al., 1991).

Pore Closure. If CVD proceeds in an ideal fashion, electrolyte is deposited at the metal chloride face of the porous substrate, without significant penetration of the pores. This is shown schematically in Figure 2.11 A. On the other hand, a non-ideal CVD process might plug pores deep within the substrate, as shown in Figure 2.11 B. The actual thickness of this film is much larger than that of the ideal film and the processing time is increased. Furthermore, ZrO₂ may not deposit as a high density film, but rather in a way which narrows the pore significantly. Such a deposit will hinder the transport of oxygen to the electrode, thereby reducing the efficiency of the electrochemical device. After 20 minutes of deposition, the mean pore radius is reduced from 9 to 6 nm. For these reasons, it is important the understand how to control the CVD stage of electrolyte deposition (Carolan and Micheals, 1987).

The deposition location can be changed from the top to the inside of porous substrates by varying the concentration and/or concentration ratio of the metal/oxygen reactants. Increasing the water vapour concentration and/or decreasing the metal chloride concentration resulted in a shift of the YSZ deposition toward the surface near the metal chloride chamber. In a study by Cao et al., 1993, the concentration of the metal chloride vapours was reduced

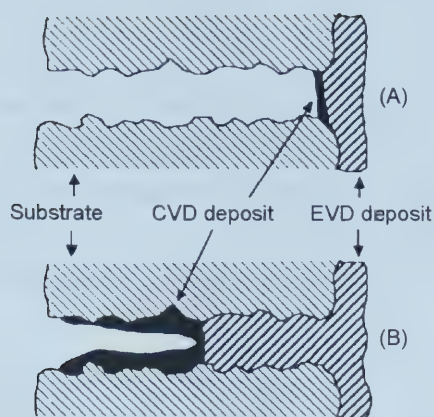


Figure 2.11 - Ideal (A) and non-ideal (B) CVD deposits (Carolan and Michaels, 1987).

about five times, while the water vapour concentration remained unchanged; the YSZ deposition was shifted outside the pores to the surface of the substrate facing the metal chloride chamber. When the CVD experimental conditions are carried out in this way there is no reduction of the average pore size in the substrate; if the film is deposited on top of the surface of the substrate, poor mechanical properties may ensue.

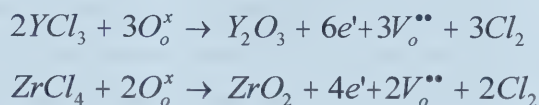
A result of the EVD process was an increase in the amount of phase boundary between the electrode substrate and the electrolyte. This is a result of the CVD portion of the reaction; electrolyte formation begins in the pores, and as long as these initial electrolyte formations are all connected to the bulk electrolyte (otherwise, they act as a barrier to oxygen diffusion), the length of the triple phase boundary is significantly increased (Schoonman et al., 1991).

Scale Growth. Once the pores are fully closed and the reactants are no longer in direct contact, the electrochemical vapour deposition step of the reaction begins. The reaction proceeds by way of oxygen anion and electron and electron hole diffusion from the H_2O/O_2 side to the metal chloride side. Metal ion and electron migration are countercurrent to oxygen ion diffusion maintaining a zero net charge. These transport processes are as illustrated in Figure 2.12. In the EVD stage of film growth, the yttrium and zirconium oxide deposit in the same ratio as present in the vapour phase (Carolan and Micheals, 1990b).

The incorporation of oxygen anions into the electrolyte film at the H_2/H_2O face of the growing film can be represented in Kroger-Vink notation as follows (Carolan and Micheals, 1990a):



Where V_o is an oxygen anion vacancy with $\bullet\bullet$ representing the effective vacancy charge, in this case, +2. Since the oxygen activity in the metal chloride atmosphere is many orders of magnitude lower than that in the oxygen/water atmosphere, oxygen anions then migrate to the chloride face of the growing film. At the metal chloride face, the oxygen reacts with the metal chlorides to produce additional electrolyte material as follows (Carolan and Micheals, 1990a):



A flux of electrons balances the ionic flux since no net current is passed (Carolan and Micheals, 1990a; Schoonman, 1991).

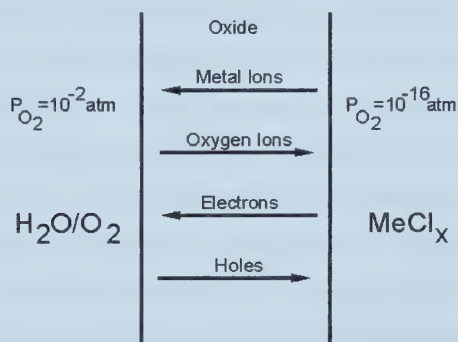


Figure 2.12 - Transport processes for EVD scale growth (Schoonman et al., 1991).

Deposition Rate. A firm understanding of reaction kinetics is necessary in EVD, as it is difficult to monitor experimentally. The self sustaining nature of the reaction, although advantageous in maintaining uniform film thickness and stoichiometry, precludes film thickness monitoring during the deposition process. Only by developing a theoretical model of the reaction kinetics can the process be controlled to consistently produce films of equal thicknesses.

The film growth rate will be constant if either the gas-phase transport steps or

oxidation steps are rate limiting, since the gas phase composition on either side of the film is held constant. On the other hand, if film growth is charge transport limited, the growth rate should be proportional to the inverse of the square root of time. Early studies analysed film growth processes in terms of the Wagner scaling process, which is the classic parabolic rate law often observed in the formation of compact scales during high temperature oxidation of metals, with four mass transport steps as follows (Carolan and Micheals, 1990a; Sasaki et al., 1993; Jonghee and Lin, 1994):

- Oxygen reactant diffusion in the substrate pores,
- Surface oxygen reduction reaction,
- Bulk electrochemical transport of oxygen ions in the EVD film, and
- Surface reaction for formation of the oxide film.

Dekker et al., 1992, plotted the various reported film thicknesses versus the deposition times according to the equation $L^2=2Kt+C_0$. Since the curve is a straight line (parabolic rate law is obeyed), it is concluded from the Wagner oxidation theory that the rate limiting step of the reaction is solid state bulk diffusion.

Carolan and Micheals, 1990a, showed that by increasing the concentration of metal chloride in the gas phase, the film growth rate increased. This was not the expected result, as the parabolic growth kinetics imply that film growth is electron diffusion limited, a process which is not directly influenced by the composition of the gas phase. Consequently, the increased deposition rate was due to changes in the oxygen partial pressure in the metal chloride atmosphere rather than increases in mass transfer or reaction rates.

A transition has been observed between the rate limiting steps of oxygen diffusion in the substrate pores and electrochemical oxygen diffusion through the growing film. At 1000°C, YSZ growth on α -alumina seems to be linear due to the pore diffusion limitation, whereas, below 900°C, the bulk electrochemical diffusion of oxygen ions through the EVD layer is the rate limiting step (Brinkman et al., 1993). de Haart et al., 1991b, on the other hand, determined that oxygen diffusion through the substrate pores was rate limiting until the growing film has reached a critical thickness. At this point, electrochemical oxygen diffusion through the film becomes dominant. The transition time was mostly affected by the substrate characteristics (i.e., a substrate with a small pore-radius to pore-length ratio increases the transition time from several minutes to several hours or days). For this reason, linear regions were not observed by most authors and they came to the justified conclusion that bulk electrochemical oxygen diffusion is the rate limiting step.

Sasaki et al., 1993, on the other hand, suggested electron transport through the YSZ

film and reaction between the surface oxygen and the metal chloride on the chloride side of the film affect the deposition rate from electrochemical vapour deposition. This supposition was also based on a change of rate limiting steps as the film thickens, although different steps were considered to be responsible. For small film thicknesses, the deposition rate is thought to be controlled by the surface reaction step; as the film thickness increases, electron transport becomes rate controlling.

However, this model employed the empirical equations without physical significance for surface reactions. It is difficult to integrate the surface reaction equations with the bulk diffusion equation using the Wagner approach. In addition, most studies considered the EVD film as essentially a single component material. Han and Lin, 1994, however, determined the four steps in the EVD process to be the same as above, except the fourth step is changed to a surface “oxidation” reaction for the formation of the oxide film. This change simply allows the model to be analysed by empirical equations for the reaction.

If the surface oxidation step is the rate limiting step, the dopant composition in the film is determined by the permeation parameters for the surface oxidation reactions. In general cases, the dopant composition may vary along the film growing direction. Conditions with high chloride partial pressures, achieved by raising the chloride temperatures in the feed and lowering the substrate surface area to flow rate ratio, favour quasi-equilibrium of the surface oxidation reactions (Han and Lin, 1994).

Film Composition Control. In order to obtain fully stabilized cubic zirconia in CVD, it is necessary to boost the vapour phase content of the yttria precursor. Dubourdieu et al., 1999, used $Y(thd)_3$ concentrations in the vapour phase above 30 mol% to obtain film compositions of 10 mol%. Figure 2.13 is a summary of vapour phase compositions versus the thin film compositions. They are compared with those of Holzschuh et al. who used the same precursors as Dubourdieu et al., although Dubourdieu et al. used a single source delivery system to deliver the chloride precursors at 300 to 350°C. Both results, however, indicate that the apparent yield of yttria is lower than that of zirconia. This phenomenon is commonly observed in MOCVD as well as conventional CVD with chloride precursors. Dubourdieu et al., 1999, speculated that this may be due to two distinct mechanisms, namely, gas phase reactions or decomposition of the yttria precursor during vaporization to reduce the net flux of active precursor into the substrate and less efficient incorporation of yttria in the growing film compared to zirconia. Since the precursors have the same chemical composition and similar atomic weights, their diffusion through the boundary layer should be

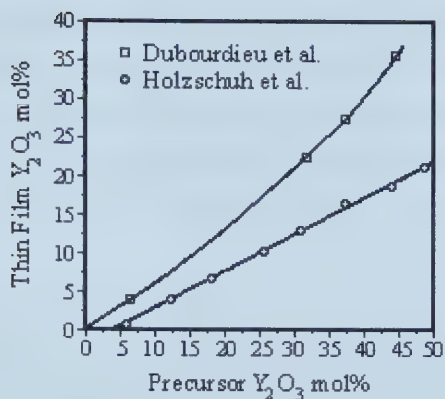


Figure 2.13 - Relationship between thin film and gas composition in MOCVD (Dubourdieu et al., 1999).

similar.

Controlling the chemical composition of yttria stabilized zirconia films during vapour phase deposition is dependent on the molar composition of the vapour phase and the molecular diffusivity and reaction kinetics of the chlorides at the substrate. A summary of vaporization temperatures, gas flow rates and chamber vapour pressures used by various authors is provided in Table 2.1. The vapour pressures and vaporization rates of the precursors are calculated using Equation 2.6 and 2.11, respectively. As is obvious from this table, it is not possible to obtain consistent or relevant data using these methods. In the case of the vapour pressures, the differing gas flow rates over the solid chlorides, which may not allow the compound to reach its equilibrium partial pressure, and chamber pressures acting on the solid which effects the solid-gas equilibrium pressure relative to the triple point on their respective phase diagrams (Zumdahl, 1989) are to blame. Vaporization rates, in this case, should provide more relevant data, but since the vaporization rates are dependent on accurate equilibrium vapour pressure data, they cannot be relied on in this instance either, as accurate data are difficult to obtain as yttrium chloride is not commonly reported in thermodynamic tables up to the evaporation temperature (Barin, 1989).

Studies by Jeon et al., 1999, on CVD of YSZ thin films at atmospheric pressure indicated that the growth rate of ZrO_2 decreased with increasing vapour pressure of $ZrCl_4$. This aspect is unusual, as the higher deposition rate is expected from the higher vaporization rate. This caused the content of Y_2O_3 in the film to increase as the $ZrCl_4$ precursor increased

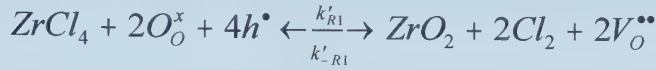
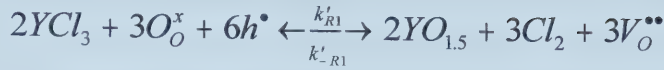
with the temperature of the YCl_3 and substrate temperature remaining fixed at 1000°C . Since the YCl_3 vaporization temperature was maintained constant, the flux of yttria into the film was assumed constant. The flux of zirconia into the film, however, decreases, contrary to their expectation that the film growth rate and zirconia content would increase. It was thought that the increase in vaporization temperature produced a high ion density, which resulted in smaller charged clusters of ZrCl_4 that do not favour rapid growth.

Table 2.1 - Selected vapour pressure data.

Reported Yttria Content (mol%)	Precursor Temperature		Theoretical Vapour Pressure			Pressure (Torr)
	T_{YCl_3}	T_{ZrCl_4}	YCl_3	ZrCl_4	Y/Zr	
7	820	280	0.250	94.731	0.13%	2.00
8	625	150	0.003	0.096	1.33%	1.50
8	724	195	0.034	1.613	0.98%	1.43
8	730	195	0.039	1.613	1.11%	1.40
10	735	170	0.043	0.361	5.02%	0.98
12.5	611	160	0.002	0.189	0.47%	1.10
17	640	160	0.004	0.189	1.03%	1.50
Reference	Flow Rates (cm^3/min)		Vaporization Rate			Deposition Process
	YCl_3	ZrCl_4	YCl_3	ZrCl_4	Y/Zr	
Ogumi et al., 1992	50	50	1.9e+16	1.7e+19	0.11%	VED
Brinkman et al., 1993	27.5	15	2.7e+14	3.3e+16	0.82%	EVD
Inaba et al., 1997	40	20	2.8e+15	4.2e+17	0.68%	EVD
Minsehige et al., 1995	40	20	3.2e+15	4.2e+17	0.77%	EVD
Ogumi et al., 1995	100	100	3.6e+15	1.1e+17	3.32%	EVD
Carolan and Michaels, 1990a	?	?	1.8e+14	6.0e+16	0.30%	EVD
Cao et al., 1993	1.5	3	4.0e+14	6.0e+16	0.66%	EVD

While in CVD, the yttrium chloride content in the gas must be enhanced, it is not the case in EVD reactions. Carolan and Michaels, 1990a, and de Haart et al., 1991b, reported that the yttria content in the film was roughly the same as that in the vapour phase. Han and Lin, 1994, performed the most comprehensive analysis of the relative reaction rates of yttrium chloride and zirconium chloride gases. The rate constants they determined at 1000°C were 2.126×10^{13} and 3.064×10^5 for yttrium and zirconium chloride, respectively, with a total

pressure of 0.14 Torr using the following reactions:



Using an yttrium chloride activity coefficient of 5.04×10^{-4} , plots of the calculated dopant concentration of the film versus the vapour phase match the experimental results reasonably well as seen in Figure 2.14.

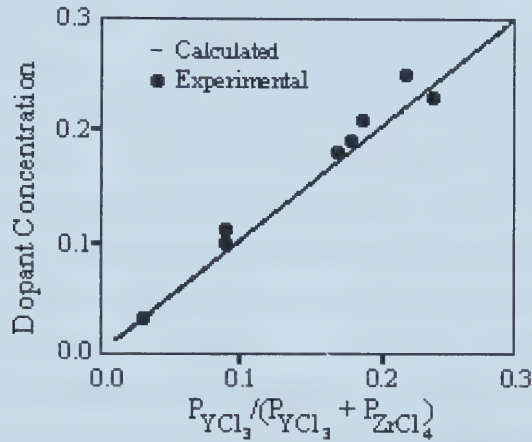


Figure 2.14 - Comparison of equilibrium dopant concentration with experimental data (Han and Lin, 1994).

Film Morphology. Due to the high activation energy for electron conduction, high temperatures are necessary for rapid film growth. However, changing the temperature of deposition affects more than the deposition rate. There is a dramatic difference in the surface texture of films grown at different temperatures, with highly faceted films grown at temperatures below 1075°C and smooth, featureless films grown at 1100°C. All films are fully dense and form independent of film composition and thickness (Carolan and Micheals, 1990a; 1990b).

Carolan and Micheals, 1990b, compared the x-ray diffraction patterns for these films to the XRD pattern of 10 mole% YSZ powder. The relative peak amplitudes for the powder and the film deposited at 1100°C were equal, indicating that the film grew isotropically or that some annealing took place. Thus, there was no preferred orientation exhibited by this film.

In contrast, however, the film deposited at 1050°C exhibits increased intensity of the (220) peak. It follows that this film is in fact oriented. In crystal structures, the first peak in the (110) group is the (220) line. Since the (220) peak intensity is enhanced, {110} planes must be oriented parallel to the substrate, indicating that the film grew preferentially in the (110) direction.

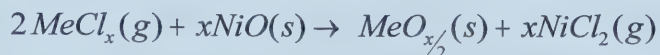
The faceting and orientation of the YSZ films indicates that a second transport process must occur in parallel with oxygen ion and electron diffusion through the film. Because faceting exposes low index planes with low surface energies in preference to high surface energy, high index planes, this process is thermodynamically driven by minimization of surface free energy. The mechanism to transform higher energy planes to lower energy planes requires a diffusional route for both anions and cations; this route is often surface diffusion. The final morphology of a film deposited by EVD, therefore, is a product of two competing processes: bulk and surface diffusion. If film growth is limited by bulk charge transport, smooth unoriented films should result. Oriented and faceted films should result when surface diffusion is the rate limiting process (Carolan and Micheals, 1990b).

An alternate and more likely explanation is that the mobile surface species that allows faceting and oriented growth to occur might become thermodynamically unstable between 1075 and 1100°C. At the higher temperature no mechanism would be available to allow surface transport of a metal species. This phenomenon has been observed in the epitaxial chemical vapour deposition of silicon on <111> silicon substrates using SiCl_3H and in the etching of <111> silicon substrates with gaseous HCl (Carolan and Micheals, 1990b).

The low temperature film morphology should provide more benefits, as the highly faceted surface has the advantages of a higher surface area and a greater surface roughness than the smooth films. Adhesion of electrodes to such a film should be superior and grain boundaries in oriented films tend to be perpendicular to the surface of the film, resulting in grains which are parallel to the direction of anion conduction in electrochemical devices. The effects of impurity phases at the grain boundaries should be reduced since the conduction path does not cross them (Carolan and Micheals, 1990b).

EVD with NiO as an Oxygen Source. Ogumi et al., 1995, reported an EVD process which utilizes the oxygen available from NiO to coat NiO pellets with YSZ by reaction with the corresponding chlorides. This coating was expected to further reduce sintering of the metal component of cermet anodes and to increase the triple phase boundary (TPB) length as will be discussed in Section 4.4 on electrode morphology.

However, two problems combine to reduce any benefits to the length of the TPB. In the initial CVD stage, the reaction between the metal chlorides and nickel oxide can occur as follows:



with standard free energy changes (at 1300 K) of -126 kJ/mol and -132 kJ/mol for zirconia and yttria, respectively (Inaba et al., 1997). The reactions take place, producing porous YSZ, until the layer was dense enough for the EVD stage of the reaction. It is during this EVD stage, however, that reduction of nickel oxide to its metal is associated with a volume reduction. The result of these two factors is a gap between the Ni and the YSZ as observed in Figure 2.15.

This method has advantages in that thin YSZ films can be prepared in any desired shape. If one uses wire shaped NiO as a substrate, a microtubular thin YSZ film will be obtained. The surface of the hollow fibre obtained by Mineshinge et al., 1996, was rough, but free of pinholes and the thickness of the zirconia layer was 3 μm . The film thickness increased linearly with deposition time, which indicates that the rate determining step is not electrochemical transport in this case. The interior of the NiO substrate as well as the NiO grains adjacent to YSZ participates in the EVD process via the dissociation of oxygen, and may enhance the deposition rate. Nevertheless, mass transport of oxygen gas was still slow in the rather dense NiO substrates used in this study, and its rate limited the overall deposition rate. It was considered that the use of a NiO substrate with a high porosity may be effective to enhance the deposition rate (Inaba et al., 1997).

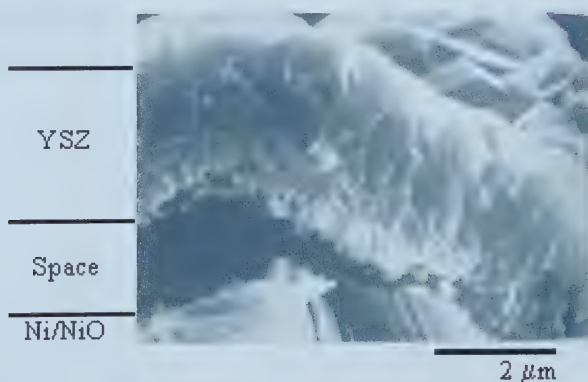


Figure 2.15 - Gap observed using NiO as an oxygen source for EVD (Ogumi et al., 1995).

Vapour Phase Electrolytic Deposition. In EVD, the motive force for the reaction is dependent on the difference in the oxygen activity in the two gaseous phases which contact the growing YSZ film. This activity difference causes a potential field, which accelerates the transport of oxide ions through the growing film. This movement disturbs the electroneutrality in the oxide and leads to charge distributions. In order to keep electroneutrality inside the YSZ layer, electrons must move in the opposite direction against an unfavourable potential field to maintain oxide layer growth. At steady state, the magnitude of the two fluxes moving in reverse directions to each other has to be equal. Therefore, in the EVD process, the deposition rate is determined by an electron flux in the oxide layer making it difficult to control the deposition rate (Ogumi et al., 1992).

In VED, however, electron transport through the growing film is not necessary and the motive force for oxide ion transport, i.e., the potential field throughout the growing oxide is supplied by an applied d.c. bias voltage. The d.c. current density will give the magnitude of the oxide ion flux through the oxide film which corresponds to the deposition rate of the oxide layer. If electron conduction participates to the same extent, the current efficiency will decrease. The VED process becomes more complicated than EVD and sputtering of the growing film may take place due to high energy particles formed in the plasma (Ogumi et al., 1992).

When the porous platinum electrode was not covered with an electrically non-conductive film, the current was carried mainly by electrons in the plasma. As a result, the YSZ layer did not grow. Before the VED process is begun, the porous platinum must be completely coated, and the first step (CVD) is carried out without application of r.f. power and a d.c. bias. The deposition rate is still slow, but Ogumi et al., 1992, contend that it will be accelerated with optimization of the plasma conditions, d.c. bias and reactor design.

Solid state ionic conductors are those materials which exhibit a high ionic transport while maintaining significantly lower electronic conduction in the solid state. An array of defects, corresponding to missing or extra atoms in the structure, participates in the movement of ions. In 1899, Nernst demonstrated that the conductivity of doped zirconia was due to mobile oxygen ions, though the concept of the responsibility of lattice defects for ionic transport in solids was not introduced until the 1920's by Frenkel. Mechanistically, ion migration occurs by ion hopping between normal and defect sites. Several different defect species will always coexist in crystals, although only those with the highest mobilities are responsible for conduction. The mobility, in turn, is governed by the energy required by the charge carrier to move between normal and defect sites. The conductivity, defect density and mobility can all be related by the Arrhenius relationship and will be discussed in Section 3.3 (Khandkar and Joshi, 1993).

The serious development of solid state electrochemical devices has continued since 1958. At the time, stabilized zirconia was recognized for its stability, ionic conduction properties and usefulness as an electrolyte material. Many solids that are now known to be ionic conductors are finding applications as electrolytes in batteries, sensors, gas separation membranes, fuel cells and many other electrochemical devices. A summary of some of today's solid electrolytes is presented in Table 3.1, although this only gives a glimpse of the number and diversity of solid state ionic conductors now available.

Table 3.1 - Solid ionic conductors and their primary charge carriers.

Conductors	Primary Charge Carrier	Reference
MgO	Mg^{2+}	Goto et al., 1990
Al_2O_3	Al^{3+}	Goto et al., 1990
CaS and CaS-TiO ₂	Ca^{2+}	Goto et al., 1990
SrS and SrS-Ce ₂ O ₃	Sr^{2+}	Goto et al., 1990
K ₂ SO ₄	K^+	Goto et al., 1990
Na ₂ SO ₄ , Na ₂ O-11 Al_2O_3 (β -alumina)	Na^+	Goto et al., 1990
<i>c</i> -ZrO ₂ , CeO ₂ , δ -Bi ₂ O ₃ , ThO ₂ , HfO ₂ , Zr ₂ Sm ₂ O ₇ , BaCeO ₃ , SrZrO ₃ , Zr ₂ Gd ₂ O ₇ , Ti ₂ Sm ₂ O ₇ and Ti ₂ Y ₂ O ₇ .	O^{2-}	Goto et al., 1990; Shukla and Gopalakrishnan, 1995; Minh, 1993; Etsell and Flengas, 1970; Kumar and Iwahara, 2000.
Li ₃ N, Li ₄ SiO ₄ -Li ₅ AlSi ₂ O ₈ (Lisicon)	Li^+	Goto et al., 1990; Bruce, 1990
KH ₂ PO ₄ , -CF ₂ -CF ₂ SO ₃ H (Nafion), CaZr _{0.9} In _{0.1} O _{3-α} , BaCeO _{3-α}	H^+	Goodenough, 1990; Iwahara and Hibino, 1993; Slade and Singh, 1991
AgI, RbAg ₄ I ₅	Ag^+	Bruce, 1990; Farrington and Dunn, 1985
CaF ₂ -MeF ₃ , SrF ₂ -MeF ₃ , BaF ₂ -MeF ₃ (Me = rare earth oxide).	F^-	Kumar and Iwahara, 2000
Eu- β -alumina	Eu^{2+}	Kumar and Iwahara, 2000
Gd- β -alumina	Gd^{3+}	Kumar and Iwahara, 2000
(NaH)GdSi ₄ O ₁₂ , SrCe _{1-x} Ln _x O _{3-δ} , BaCe _{1-x} Ln _x O _{3-δ}	H^+	Kumar and Iwahara, 2000

3.1 Ion Conduction Mechanisms in Solid Electrolytes

Solid state ionic systems include materials with lattice defects or channel structures that allow ions to flow rapidly through them (Julien, 1990). The mechanisms by which solids conduct ions were first described by Frenkel and Schottky early in the 20th century. Frenkel noted that if an ion in a normal lattice position moves to an interstitial site, it leaves behind a vacancy and can then hop to an adjacent interstitial site or to a vacant lattice site (Frenkel, 1926; Farrington and Dunn, 1985). Binary inorganic “Frenkel” salts like AgCl conduct Ag^+ ions by ion exchange between normal Ag^+ lattice positions and interstitial sites (Khandkar and Joshi, 1993).

Schottky proposed a mechanism which was slightly different. He suggested that a small fraction of normal lattice sites can be unfilled by their appropriate ions. The resulting vacancies can move through the structure and transport charge (Schottky, 1935; Farrington and Dunn, 1985). In “Schottky” salts, like LiCl, the Li^+ moves via hopping between normal and vacancy Li^+ sites. Fluorite structures typically exhibit oxygen anion motion via a vacancy mechanism (Khandkar and Joshi, 1993).

In glassy and amorphous electrolytes such as solid polymer electrolytes, conduction is through the correlated motion of ions. Glasses consist of random packing of atom clusters of varying proportions and in this super quenched liquid state the charge carriers are decoupled from the matrix. In such structures, the simplified concept of conductivity being a product of carrier concentration and mobility with a unique activation energy does not hold. Instead, a distribution of activation energies is more commonly observed, attributable to the statistical variation of the local ion coordination number surrounding the mobile ion (Khandkar and Joshi, 1993).

Composite electrolytes are the final distinct structural group of solid electrolytes which typically consist of two or more phases, such as AgI- Al_2O_3 . These composite materials exhibit very unique conduction properties, primarily influenced by space charge effects at heterogeneous interfaces between the particles (Khandkar and Joshi, 1993).

The rate at which these ions or defects migrate through a particular compound determines the ionic conductivity of the electrolyte and is dependent upon the energy required to move an ion from one interstitial site to another, or from one filled lattice site to a vacancy. For normal compounds, the energy required to create defects is rather high (typically 1-2 eV). As a result, the defect population can be small. However, in some rare compounds, the energy of defect creation is almost zero. An example is AgI, which has an ionic conductivity for Ag^+ of about 10 S/cm at 160°C. The Ag^+ ions are so conductive in the solid state that its

conductivity actually decreases after melting (Farrington and Dunn, 1985).

3.2 Properties of Good Solid Ionic Conductors

The mechanisms for ion conduction described by Frenkel and Schottky imply that for a solid to be a good ionic conductor, it must first have a population of ions vacant sites distributed within the lattice. In addition, the energy required to disorder the ions (energy for defect creation) and the energy required to move ions among the sites (the energy of defect migration) must both be small (Farrington and Dunn, 1985). The following is a list of some of the more important properties which are necessary for a solid electrolyte to be useful in practical applications (Huggins, 1980; Liang, 1983; Julien, 1990):

- high ionic conductivity,
- selectivity of ionic transport,
- negligible electronic transport,
- high power to volume and weight ratios,
- stability with respect to thermal and electrochemical decomposition,
- chemical stability of the components,
- mechanical stability, and other related properties (e.g. matching thermal expansion coefficients),
- ease of fabrication with readily available materials at satisfactory cost, and
- adequate safety (must not produce harmful byproducts).

If the electronic conductivity is not extremely low (at least two orders) in comparison with the ionic conductivity, significant internal short circuiting will occur. This short circuit is current that is unavailable to carry out useful functions in the external circuit. In the case of batteries, for example, electronic conductivity in the electrolyte would cause a battery to discharge as it stands unused (Julien, 1990).

Maintaining thermal, chemical and electrochemical stability with other components in their environments is of utmost importance for long term life and restricts operating temperatures, pressures and chemical potential ranges such that the most favourable kinetics may be unattainable. If interfacial byproduct layers form, further progress of the reaction is uncertain. If the reaction product layer is continuous, the reaction can only proceed by the transport of matter through it and it should therefore act as a protective barrier against further reaction, while remaining ion conducting. In most cases, however, the layer has a low value of ionic conductivity and solubility and gradually grows to an appreciable thickness,

producing large, deleterious impedances (Huggins, 1980).

3.3 Fluorite-Type Oxygen Ion Conductors

Typically, oxygen anion diffusion is very slow in most metal oxides, but some high melting point oxides develop high conductivities at temperatures of 500 to 1000°C. Various solid solutions of the group IV B oxides, such as zirconia and hafnia, have unusually high anion conduction properties. The highest conduction rates are achieved with the relatively open cubic fluorite-type crystal structure, an FCC arrangement of cations with the oxide ions occupying tetrahedral sites as seen in Figure 3.1. Fluorite type crystal structures are observed in zirconia, hafnia, ceria, bismuth oxide and thoria, although in some cases (i.e. zirconia) they are high temperature morphologies. Through substituting divalent or trivalent oxides into the matrix, the high temperature polymorphs can be stabilized and, more importantly, the oxygen vacancy concentration is enhanced significantly as detailed in Figure 3.2 (Hufschmidt, 1996; Badwal and Foger, 1997; Kawada and Yokokawa, 1997).

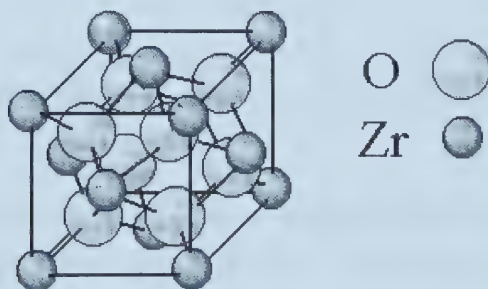
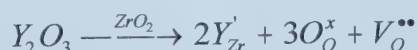


Figure 3.1 - Cubic fluorite type structure of stabilized ZrO_2 (Kawada and Yokokawa, 1997).

The high ionic conductivity of these oxide ceramics originates from the existence of vacancies on the oxygen sites. For example, in Kröger-Vink notation, substituting Zr(IV) with Y(III) is written as (Kawada and Yokokawa, 1997):



According to Heyne's model of ambipolar transport, mass transport in metal oxide systems requires local electroneutrality. Charge neutrality in this case is maintained by the formation of oxygen vacancies (Park and Blumenthal, 1989).

The ionic radius of the dopant has a quantifiable effect on the conductivity of the

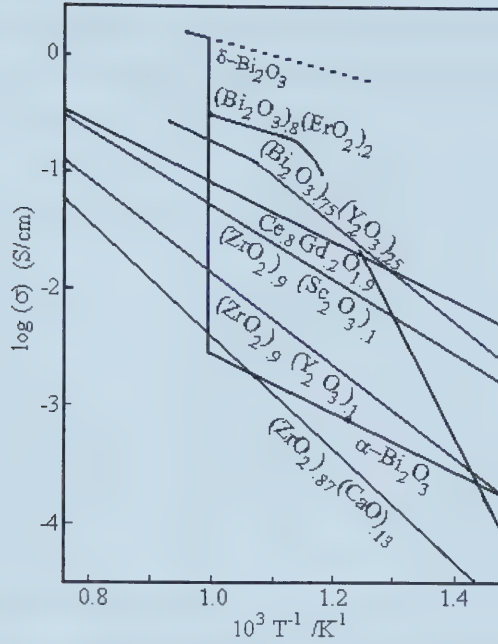


Figure 3.2 - Oxide ion conductivities of some oxides with fluorite-type or fluorite related crystal structures (Shukla and Gopalakrishnan, 1995).

fluorite-type oxides. If one assumes that the activation energy to move oxygen ions through the lattice is related to the channel radius formed by neighbouring cations, then the channel radii are calculated with the following equation (Pascual et al., 1983):

$$s = \left(\frac{d}{\sqrt{6}} \right) - r_c \quad (3.1)$$

where s is the channel radius, r_c is the average cation radius and d is the lattice parameter. The lattice parameter can be calculated with the Aleksandrov model, which is only applicable for single crystal or bulk polycrystalline materials, for different amounts of stabilizing elements by assuming spherical packing of ions and utilizing the calculated mean number of anion vacancies per cell as follows (Kim et al., 1993):

$$d = A \left[R_{Zr} + R_O + \frac{\sum (P_k M_k \Delta R_k)}{100 + \sum M_k (P_k - 1)} \right] \quad (3.2)$$

where k represents the stabilizer element, R the ionic radii, M the mole percentage of stabilizer

and P the number of ions per unit cell of each stabilizing element of the oxide. The constant A is based on the geometry of the unit cell of the fluorite structure ($A = 2.3094$ for cubic phase zirconia). A simplified form of this equation for the yttria-zirconia system can be expressed as follows (Kim et al., 1993):

$$d = 2.3094 \left[2.21 + \frac{0.018 M_{Y_2O_3}}{100 + M_{Y_2O_3}} \right] \quad (3.3)$$

The channel radius can be used to determine the order of increasing activation energy for various dopants, but it does not correspond with observed results. The activation energy for conduction should be lower for those solid solutions where d is larger, ie. $Er^{3+} < Y^{3+} < Dy^{3+} < Ce^{4+} < Nd^{3+}$. However, the activation enthalpy for ionic conduction has been shown to steadily increase and the conductivity steadily decrease with increasing ionic radius of the dopant (although most studies have focussed on dopants with a larger ionic radius, as ceramics such as zirconia and hafnia have a very small radius. In the case of scandia doped ceria, scandia has a smaller ionic radius than ceria and is not as good a conductor as gadolinia, which is approximately the same size and ceria). It is believed that the mismatch between the host and the dopant cation creates a strain energy which contributes to the association energy of the defect pair. Thus, the closer the dopant radius is to the major electrolyte component and the larger the channel radius, the better the performance. This is marked by a much better ionic conductivity observed in doped-ceria and bismuth oxide over stabilized-zirconia and hafnia (Trubelja and Stubican, 1991; Hufschmidt et al., 1996).

The maximum conductivity occurs at an anion vacancy concentration of around 3.5 to 4% (about 8 mol% M_2O_3) for trivalent dopants and 6 to 7% (13 mol% MO) for divalent dopants (Badwal and Foger, 1997). Incidentally, in zirconia, these values are the minimum dopant concentrations required to fully stabilize the fluorite phase. At a vacancy concentration of 2.9% (6.3 mol% Y_2O_3) interaction among defects starts to appear, which results in an increase in the activation energy. The conductivity, however, continues to increase as the number of vacancies remains a dominant factor. (Ioffe et al., 1978). A decrease in conductivity is experienced to a minimum at 8 mol% M_2O_3 dopant concentrations and is believed to be due to defect ordering, vacancy clustering or electrostatic interaction. The basis for this is generally classified into one of three reasons as follows (Trubelja and Stubican, 1991):

- vacancy hopping is limited by repulsive interaction of the vacancies,
- vacancy transport is highly preferred along certain coordination units,

and

- oxygen vacancy-dopant cation associates are formed which effectively reduce the number of mobile vacancies.

Molecular dynamics studies by Chaba and Ngoepe, 1997, have shown that ionic conductivity decreases with an increasing number of nearest neighbour Y^{3+} - Y^{3+} pairs. The local structural environment of Y^{3+} ions is more disordered than that of the Zr^{4+} ions. The Y^{3+} ions are found to have smaller coordination numbers than the Zr^{4+} cations. This indicates that oxygen vacancies are nearest neighbours of Y^{3+} ions. The simulation results strongly suggest that oxygen vacancies are trapped by the Y^{3+} ions and nearest and next-nearest neighbour Y-Y pairs can form clusters at high Y_2O_3 concentrations. The bigger the Y-Y neighbour clusters are, the more vacancies they will trap. As a consequence, the ionic conductivity will decrease rapidly with further yttria addition (Xiaoyun and Hafskjold, 1995).

In a binary oxide solid solution system, such as AO-BO₂, that is a predominantly ionic conductor with a small partial electronic conductivity, a galvanic cell can be constructed (Goto et al., 1990):



and isobaric conductivity variations with temperature conform to Arrhenius type relationships of the form (Patterson, 1971):

$$\sigma = \sigma^\circ \exp^{-Q/RT} \quad (3.4)$$

where σ° is a constant and the effective activation energy Q is a temperature independent constant whose value depends on the mechanism of conduction. The total conductivity of AO-BO₂ is the sum of the partial conductivities due to the migration of A^{2+} cations, B^{4+} cations, O^{2-} anions and excess electrons or holes (Goto et al., 1990):

$$\sigma_{total} = \sigma_{A^{2+}} + \sigma_{B^{4+}} + \sigma_{O^{2-}} + \sigma_e + \sigma_h \quad (3.5)$$

When the solid electrolyte is an oxygen anion conductor with a small electronic conduction, the electromotive force of the galvanic cell is represented by (Goto et al., 1990):

$$\mathcal{E} = \frac{RT}{4\mathcal{F}} \ln \frac{P''_{O_2}}{P'_{O_2}} - \int_{P'_{O_2}}^{P''_{O_2}} t_e \frac{RT}{4\mathcal{F}} d \ln P_{O_2} \quad (3.6)$$

where R is the gas constant, T is the absolute temperature, \mathcal{F} is Faraday's number and t_e is the transference number of electrons or positive holes as follows (Goto et al., 1990):

$$t_e = \frac{\sigma_e}{\sigma_e + \sigma_h + \sigma_{A^{2+}} + \sigma_{B^{4+}} + \sigma_{O^{2-}}} \quad (3.7)$$

The migration of cations is not a factor in fluorite oxides and is assumed to be negligible, and the ion, electron and hole conductivities are represented by the following equations (Patterson, 1971):

$$\begin{aligned} \sigma_{ion} &= \sigma_{ion}^{\circ} \exp\left(\frac{-Q_{ion}}{RT}\right) \\ \sigma_h &= \sigma_h^{\circ} \exp\left(\frac{-Q_h}{RT}\right) P_{O_2}^{1/4} \\ \sigma_e &= \sigma_e^{\circ} \exp\left(\frac{-Q_e}{RT}\right) P_{O_2}^{-1/4} \end{aligned} \quad (3.8)$$

The log of the ionic, electronic and hole conductivities plot as planar sheets in a three-dimensional log P_{O_2} and $1/T$ versus log σ graph as illustrated in Figure 3.3. A plot of the total conductivity surface on the same graph demonstrates that, in regions where one conduction mechanism is dominant, the log of the total conductivity becomes incident with that planar sheet. In region A, for example, hole conductivity is the dominant conduction mechanism and

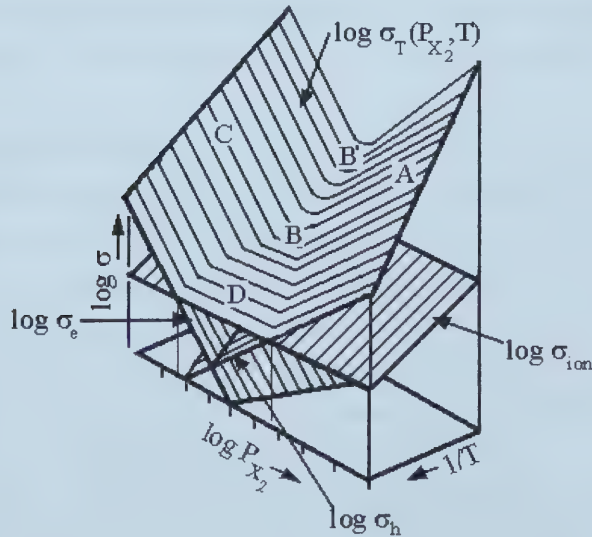


Figure 3.3 - Schematic representation of log σ surfaces over log P_{X_2} and $1/T$ space (Patterson, 1971).

the total conductivity is coincident. The electrolytic domain is contained in region D and is defined as the region where the ionic conductivity is greater than the sum of the hole and electron conductivities by at least 100 times (Patterson, 1971).

The locus of points that forms the boundary between positive hole conduction and excess electron conductivity domains is represented by the following equation (Patterson, 1971):

$$\log P_{X_2} = -\frac{n}{2} \cdot \frac{Q_e - Q_h}{2.303RT} + \frac{n}{2} \log \frac{\sigma_e^\circ}{\sigma_h^\circ} \quad (3.9)$$

where n is the number of electrons. This boundary plots as a straight line with a slope of $-(n/2)(Q_e - Q_h)/2.303R$ and an intercept of $(n/2)\log(\sigma_e^\circ/\sigma_h^\circ)$. Introducing a factor of 100 to the above equation produces electrolytic domain boundaries as follows (Patterson, 1971):

$$\begin{aligned} \log P_{X_2} &= -n \left(\frac{Q_{ion} - Q_h}{2.303RT} \right) + n \log \left(\frac{\sigma_{ion}^\circ}{100\sigma_h^\circ} \right) \\ \log P_{X_2} &= +n \left(\frac{Q_{ion} - Q_e}{2.303RT} \right) - n \log \left(\frac{\sigma_{ion}^\circ}{100\sigma_e^\circ} \right) \end{aligned} \quad (3.10)$$

These boundaries are critical in the evaluation of a given mixed conductor for use as a solid electrolyte. Figure 3.4 shows the relationships among the various domain boundaries. In this representation, σ° and Q values are assumed to be known with certainty.

3.3.1 Zirconia-Based Electrolytes

Zirconia based materials offer the best possible choice at this stage in terms of conductivity (ionic transport close to unity, although it does not have the best conductivity), cost, stability in both oxidizing and reducing environments in the 800 to 1000°C temperature range (10^5 to 10^{-13} Pa oxygen partial pressure), relative inertness, good thermal and mechanical shock resistance and excellent mechanical properties. On account of these benefits, stabilized zirconia is ideal for use in electrolyte applications (Schoonman et al., 1991; Liu and Khandhar, 1992; Minh, 1993; Badwal and Foger, 1997).

Zirconia has three distinct phases between room temperature and the melting point of 2680°C. Below 1170°C, a monoclinic (m) structure exists, which transforms into a tetragonal structure (t) over a temperature range of approximately 100°C above this temperature. This transformation is extremely deleterious to components, as it is associated

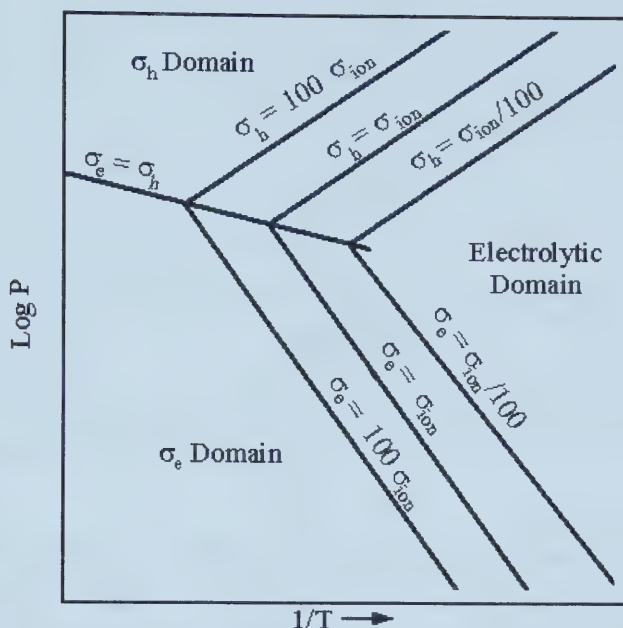


Figure 3.4 - Relationship between electrolytic and ionic domain boundaries in the $\log P_{X_2}$, $1/T$ plane (Patterson, 1971).

with a large (3% to 5%) volume change (contraction on heating) that can lead to cracking or spalling. The fluorite type cubic phase exists from 2370°C to the melting point (Shubbarao, 1981; Minh, 1993; Bradford, 1993).

By stabilizing the cubic structure to room temperature with the addition of CaO, MgO, Y_2O_3 , Sc_2O_3 or certain rare earth oxides that exhibit relatively high solubility, the anion conductivity is enhanced. Although scandia has better conductivity than yttria, yttria is the most widely studied element for use as a stabilizer for zirconia because of its availability and cost and, therefore, will be the focus of most of the discussion (Schoonman et al., 1991; Minh, 1993).

The activation energies for electron and hole conduction are not very sensitive to the amount and type of dopant. In comparison, the ionic conductivity between 700 and 900°C ranges from 10^{-3} to 10^{-2} S/cm and the activation energy varies with yttria content as in Figure 3.5. Up to about 6 mol% YSZ, the activation energy is practically constant, but after that it increases sharply with increasing concentration of stabilizer. The reasons for this and for the continued increase in conductivity up to 8 mol% YSZ were discussed in detail in Section 3.3 (Ioffe et al., 1978). At high oxygen partial pressure ($P_{O_2} > 10^{-5}$ Pa at 900°C) p-type conduction occurs, while at low oxygen partial pressure n-type conductivity occurs. Because

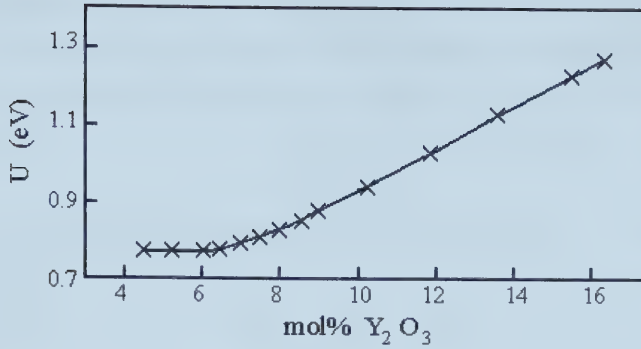


Figure 3.5 - Activation energy from 950 to 1050°C versus molar yttria content (Ioffe et al., 1978).

the activation energy of the holes is lower, the oxygen partial pressure for the transition from p- to n-type conductivity increases with increasing temperature (Weppner, 1977). The following empirical equations were derived for ion, electron and hole conductivity (in S/cm) for 8 mol% YSZ by Park and Blumenthal, 1989:

$$\begin{aligned}
 \sigma_{ion} &= 1.63 \times 10^2 \exp\left(\frac{-0.79eV}{kT}\right) \\
 \sigma_h &= 1.31 \times 10^7 \exp\left(\frac{-1.67eV}{kT}\right) P_{O_2}^{1/4} \\
 \sigma_e &= 2.35 \times 10^2 \exp\left(\frac{-3.88eV}{kT}\right) P_{O_2}^{-1/4}
 \end{aligned} \tag{3.11}$$

Grain boundary resistance is often higher for poorly defined (micro inhomogeneous) electrolyte microstructures, increasing with impurity level and porosity and decreasing with increasing grain size. In the absence of poorly conducting grain boundary phases, the conductivity is influenced by the dopant level, grain size, porosity and, at low temperatures, by dopant cation-vacancy interactions. Arrhenius plots of the conductivity consistently show a change in slope towards a higher activation energy at low temperatures. Both grain boundary resistance and dopant cation-vacancy interactions dominate increasingly at low temperatures and thus can influence the shape of these plots. Single crystal examinations support the theory that dopant cations and vacancies form neutral defect pairs and the activation enthalpy for conduction consists of contributions for enthalpies of defect pair

association and vacancy migration. With increasing temperature, the defect pairs begin to dissociate and the conductivity is determined mainly by the charge carrying defects that are controlled by the concentration of the aliovalent dopant and interactions between defects (Badwal, 1984).

Tetragonal Zirconia Polycrystals. Yttria-tetragonal zirconia polycrystals (Y-TZP) exhibit excellent mechanical properties and have been the subject of extensive study for engineering applications. The high strength (>1 GPa) and fracture toughness (>4 -6 MPa $\sqrt{\text{m}}$) in materials containing 2 to 3 mol% Y_2O_3 results from stress induced phase transformation of the metastable tetragonal phase to the monoclinic phase (Badwal, 1990). The ionic conductivity of 3 mol% yttria-zirconia is lower than fully stabilized zirconia by a factor of about three at 1000°C. At temperatures below 500°C, the bulk conductivity of t- ZrO_2 is greater than that for YSZ and at a temperature of 700°C, the lattice resistivity of Y-TZP was greater than that of fully stabilized zirconia (Badwal and Foger, 1997).

Although there is a small electronic conductivity which is not desirable for electrolytes in fuel cell applications, the conductivity remains reasonably constant for several thermal cycles and for a reasonable length of time. With long term exposures at high temperatures, however, TZP electrolytes can suffer mechanical degradation resulting from growth and subsequent transformation of the metastable tetragonal phase to monoclinic with associated mechanical stress (Patil et al., 1992).

Additionally, a pronounced conductivity aging behaviour results from enhancement of the grain boundary blocking effect. The grain boundary resistivities of TZP samples are consistently higher than that of PSZ or FSZ, resulting in a higher total resistivity. The value of the grain boundary resistivity is sensitive to the grain size and the presence of grain boundary phases. The inherently small grain size illustrated in Figure 3.6 and resultant large grain-boundary surface area of the tetragonal phase necessary for better mechanical properties accumulates impurity phases. The contribution of grain boundary resistivity was large and the total resistivity of TZP, in comparison with fully stabilized zirconia, was much higher as outlined in Table 3.2 (Badwal and Swain, 1985; Badwal, 1990; Minh, 1993).

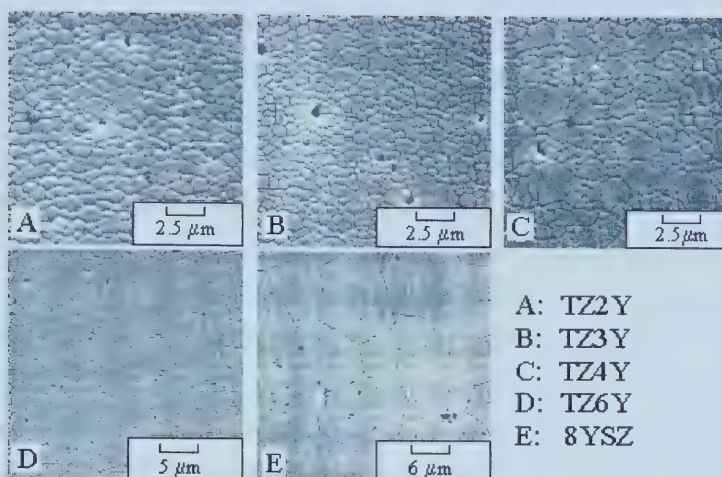


Figure 3.6 - SEM micrographs illustrating the variation in grain size distribution as a function of yttria content. All materials sintered at 1600°C for 2 h (Badwal, 1990).

Table 3.2 - Bulk grain and grain boundary resistivity values measured at 300°C for samples of zirconia with varying yttria contents (Bonanos et al., 1984).

Sample	Composition (mol% Y_2O_3)	Resistivity ($\Omega \cdot \text{cm} \times 10^5$)		
		ρ_{bulk}	ρ_{gb}	ρ_{total}
TZP (0.8 μm grain size)	3.0	1.7	4.6	6.3
TZP (0.5 μm grain size)	3.0	1.3	6.1	7.4
PSZ	4.7	2.6	1.4	4.0
FSZ	6.0	1.8	0.8	2.6

Mixed conductors. While in the search for the best electrolyte materials, it is best to have the lowest electronic transference number possible, mixed conductors are of interest for electrode materials, as it is thought that partial ionic conductivity will increase the reactive area as will be discussed further in Section 4.4.3. It has long been known that electronic conductivity can be increased by the addition of multivalent transition metal cations into the cubic-fluorite phase. The addition of 4 mol% Mn in YSZ, for example, increases the hole conductivity by a factor of 10 (Kawada and Yokokawa, 1997). The increase in electronic conductivity is due to small polaron electron hopping conduction via the Me^{3+} and Me^{4+} cations. In addition to manganese, cerium oxide (Patil et al., 1992), titanium oxide (Colomer

et al., 1996), terbium oxide (Xia et al., 1998) and iron oxide (Van Hassel and Burggraaf, 1992) can be used to enhance the electronic conductivity.

Difficulties can arise if the dopant precipitates a second phase that is deleterious to grain boundary conduction. In the case of titania doping, the cubic phase is stable for additions of up to 15 mol% as long as there are no impurities present. Sintering aids such as silica and alumina cause the precipitation of $\text{Al}_4\text{Ti}_2\text{SiO}_{12}$ in the grain boundaries. The electronic transference number increases with increasing titania and decreasing temperature. The temperature variation reflects the fact that the activation energy (0.9 eV) for oxygen ion conductivity is higher than that for electronic conductivity (0.73 eV). Thus, increasing the temperature produces a larger increase in the ionic conductivity than in electronic conductivity (Worell, 1992). A strong dependence of the electronic conductivity on the oxygen partial pressure and temperature, however, prevents optimal levels of electronic conductivity except under limited conditions (Xia et al., 1998).

A second class of mixed conducting oxides are two phase materials composed of ionic and electronic conductors. Doping (single phase) often results in a reduction of the ionic and total conductivity of mixed conductors, although excellent chemical and mechanical compatibility of YSZ electrolytes have been cited as a major advantage. With dual phase materials, such as NiO-YSZ (Park and Choi, 1999) and Ag-YSZ (Xia et al., 1998), the combined properties are often superior to single phase mixed conductors and properties not seen in an individual phase may appear in the composite.

3.3.2 Bismuth Oxide-Based Electrolytes

Bismuth oxide, a predominantly electronic conductor, exists in the monoclinic form at room temperature and, as with zirconia, the phase change is associated with a large volume change. Yttria, dysprosia, erbia, gadolinia, niobia and tantala are the primary oxides used to both stabilize the cubic fluorite phase (δ) and increase the oxygen vacancy concentration (Badwal and Foger, 1997). In stoichiometric δ -phase bismuth oxide, 25% of the anion sites are vacant. Under atmospheric conditions, Bi_2O_3 is an excellent oxygen ion conductor with very little electronic conduction when present in the δ -phase, which is stable between 730°C and the melting point of 825°C (Joshi et al., 1990).

Bismuth oxide electrolytes have a relatively high conductivity at low temperatures in comparison with zirconia based electrolytes. They also have the advantage that they can be sintered at lower temperatures (1300 K) to greater densities (>90%). However, the oxygen dissociation pressure is high (10^{-5} Pa at 700°C) and decomposition into bismuth metal occurs

at oxygen partial pressures of about 10^{-8} Pa at 600°C , severely limiting practical applications of this material. Above this temperature, these materials are corrosive and can react quickly with other materials, including platinum (Keizer et al., 1979; Joshi et al., 1990; Minh, 1993).

Additionally, under a d.c. current mode, the current density in both yttria- and niobia-stabilized bismuth oxide continually decreased, with the decrease being considerably greater in the yttria-stabilized bismuth oxide. Subsequent investigations with x-ray diffraction show that a second phase is clearly evident in the pattern, with the kinetics of transformation and grain growth increasing with temperature. Although yttria-stabilized electrolytes have a much greater initial conductivity (approximately 5 times higher), the degradation rate is much slower in niobia-stabilized electrolytes in comparison with yttria stabilized bismuth oxide (Joshi et al., 1990).

The values of the ionic conduction in $\text{Bi}_2\text{O}_3\text{-Er}_2\text{O}_3$ ($1\ \Omega\cdot\text{m}$ at 720 K) are 2 times higher than in $\text{Bi}_2\text{O}_3\text{-Y}_2\text{O}_3$, and is one of the best oxygen ion conductors known. However, high densities were difficult to obtain as grain boundary mobility was too rapid during sintering. Samples containing 17.5 to 45.5 percent erbia contained a monophasic FCC structure with a lattice constant ranging from 0.550 to 0.540 nm with increasing erbia content (Keizer et al., 1979).

3.3.3 Ceria-Based Electrolytes.

Several researchers have demonstrated that CeO_2 doped with alkaline earth or rare earth oxides exhibits ionic conductivity up to two orders of magnitude higher than zirconia based electrolytes at comparable temperatures. The conduction in undoped ceria is largely electronic (ionic transference = 0.4) and, although small additions of dopants sharply increase the ionic transference number, the electronic transference number increases in the presence of a reducing atmosphere (Virkar, 1991) accompanied by mechanical weakening (Mishima et al., 1998). At 800°C , the lowest oxygen partial pressure limit is about 10^{-5} to 10^{-7} Pa at best. The addition of some electron trapping agents have been reported to further the extent of the ionic domain, but the lower value of oxygen partial pressure is still significantly higher than that experienced by the electrolyte in fuel environments (Badwal and Foger, 1997).

Calcium, yttria, samaria, gadolinia and a number of other rare earth oxides are commonly used to dope ceria electrolytes (Badwal and Foger, 1997). For cerium oxide doped with various M^{3+} cations, the experimentally determined association enthalpies show a minimum between Y^{3+} and Gd^{3+} dopants. The ionic radius of these two materials are 1.018 Å and 1.053 Å, respectively, which are close to Ce^{4+} which has an ionic radius of 0.97 Å

(Trubelja and Stubican, 1991).

The mixed oxide $(\text{CeO}_2)_{0.9}(\text{Gd}_2\text{O}_3)_{0.1}$ was found to be the best conductor of oxygen ions. The relative stability under a reducing atmosphere allows it to be considered for high temperature fuel cell applications. The solid solution has an ionic conductivity of 0.45 S/cm at 700°C (Overs and Riess, 1982). Other more comprehensive investigations obtained similar results (Kudo and Obayashi, 1976; Eguchi et al., 1986).

The high ionic conductivity of calcia-doped ceria is exceptional in that the conductivity decrease is very gradual even up to the solubility limit, eliminating the need for precise composition control and allowing more of the cheaper calcia to be used. Even the precipitated calcia crystals (23 to 50 mol% calcia), which are insulating to both electron and ion conduction, scarcely interfere with the diffusion of oxygen ions in the solid solution (Eguchi et al., 1986). Preda and Dinescu, 1976, reported that there was some perovskite type CaCeO_3 formed upon heating at 1400 to 1500°C, but this was scarcely detected at any composition in the study conducted by Eguchi et al., 1986.

Composite Electrolytes. An array of dopants and dopant concentrations have not successfully suppressed departures from stoichiometry and n-type electronic conductivities in doped ceria to the extent that is required, necessitating the use of new approaches. Thin electron blocking layers have been studied to try to overcome significant cell voltage drop when loaded. A thin coating of zirconia prevents the reducing environment from contacting the doped ceria while substantially lowering the overall internal resistance when compared to all stabilized zirconia electrolytes at equivalent temperatures. The stability of ceria then becomes dependent on the partial pressure of oxygen at the zirconia/ceria interface which, in turn, depends upon the transport characteristics, especially the electronic conductivity, of CeO_2 . High electronic conductivity and ionic conductivity on the CeO_2 side ensures high oxygen partial pressure at the interface and, thus, high thermodynamic stability (Minh, 1993; Hartmanova et al., 1999).

Experimental results using zirconia membranes to protect the doped ceria demonstrated a significant enhancement in the open circuit voltage and power density over uncoated ceria. Analysis by Virkar, 1991, demonstrated that composite electrolytes used instead of all zirconia electrolytes result in lowered operating temperatures (600 to 800°C) with adequate conduction properties. Typically, 4-8 μm of yttria doped ceria with 1 to 1.5 μm of YSZ on the anode side provide a power density of 210 mW/cm² at 600°C (Mishima et al., 1998).

Problems can include incomplete adhesion (space between layers) (Virkar, 1991), reactions between ceria and YSZ, and thermal expansion mismatches ($\alpha=10.5\times10^{-6} \text{ K}^{-1}$ for YSZ compared with $\alpha=12.5\times10^{-6} \text{ K}^{-1}$ for ceria). While the overall resistance of the cell decreased, the open circuit voltage was reduced in the mixed conducting electrolyte. Similarly, ceria has been shown to form a solid solution with zirconia after high temperature processing, leading to both reduced ionic conductivity and electronic conduction (Mishima et al., 1998; Tsai and Barnett, 1998).

3.3.4 *Thoria Based Electrolytes*

The limits of applicability of YSZ electrolytes with a cubic fluorite structure are determined by partial electron conductivity, especially at high temperatures. An increase in electron conductivity is observed with decreasing oxygen partial pressure. Although doped thoria develops p-type conductivity in oxidizing environments ($>10^{-8} \text{ atm}$ at 1000°C) and the conductivity is not particularly high (.0048 S/cm at 1000°C with 8 mol% yttria), thoria based solid solutions exhibit a stable fluorite structure up to the melting point and offer a higher degree of chemical stability in ultra low oxygen partial pressure environments ($<10^{-22} \text{ atm}$ at 1000°C). Thus, these electrolyte systems can fill a niche as, for example, sensors in extremely low oxygen partial pressure and high temperature systems, such as steel melts (Etsell and Flengas, 1970; Hufschmidt et al., 1996; Badwal and Foger, 1997).

The atomic radii of the rare earth ions Nd^{3+} ($r = 1.04 \text{ \AA}$) and Sm^{3+} ($r = 1.00 \text{ \AA}$) are very similar to that of Th^{4+} ($r = 1.02 \text{ \AA}$) and are considered to be the most suitable stabilizers and dopants for thoria based solid electrolytes. Nd_2O_3 is especially suited as it has the lowest electronic conductivity parameters and the sintering treatment exerts a significant influence on the measured electrical properties (Hufschmidt et al., 1996).

3.3.5 *Hafnia Based Electrolytes*

Fluorite type hafnia has long been known to be a fast ion conductor, although much less attention has been given to its solid solutions as solid electrolytes. The reason is most likely that zirconia and hafnia behave similarly: they have the same structure and show the same type of phase transitions, etc. Hafnium oxide, however, is considerably more expensive, making it less attractive for most applications (Trubelja and Stubican, 1991).

Similar to zirconia, hafnia has the monoclinic phase structure at room temperature, with the fluorite-type crystal structure at high temperatures and the cubic structure can be stabilized with the addition of certain aliovalent cations (Trubelja and Stubican, 1991). The

ionic radius of Hf^{4+} ($r = 0.83 \text{ \AA}$) is smaller than most of the dopants typically used to stabilize the cubic structure. Typical behaviour is observed for $\text{HfO}_2\text{-M}_2\text{O}_3$ systems in regards to the relationship of electric conductivity to ionic radius of the dopant. The exceptions to the rule were yttria and holmia. The ionic conductivities of yttria solid solutions are higher at all investigated temperatures but the lattice parameters for holmia solid solutions are larger. The ionic radius of Ho^{3+} is reported to be 1.015 \AA and that of Y^{3+} is 1.019 \AA . Trubelja and Stubican, 1991, speculated that this may indicate that the ionic radius of Ho^{3+} may be larger than Y^{3+} . Data provided by Etsell and Flengas, 1970, indicate that the ionic radii are approximately equal (0.91 to 1.07 \AA depending on the source).

In principle, all fuel cells operate as continuous batteries: fuel and oxygen are combined in the presence of a catalyst to generate a dc current. The fuel is composed of either pure hydrogen or a hydrocarbon obtained by conditioning natural or process gas, naphtha or one of several other petroleum distillates available, depending on the fuel tolerances of the fuel cell system used (Wheat, 1979). Fuel cells, then, are defined by Grubb and Niedrach, 1966, as “an electrochemical device that directly converts the chemical energy of a fuel oxidation reaction into electrical energy.”

The direct conversion of chemical potential into heat and electricity with fuel cells eliminates a series of steps and stages necessary in most energy cycles and should, therefore, result in much better efficiency (Grubb and Niedrach, 1966). Whether using the Carnot heat cycle in heat engines, which converts thermal energy into mechanical energy, which is then converted into electrical energy with a conventional electrical generator; the Rankine cycle

in steam power plants, where the work of an expanding gas is used to turn a steam turbine; the Brayton cycle in reciprocating gas power plants, where piston compressors and expanders work in conjunction with heat exchangers to heat and cool the working gas; the Otto cycle in spark ignition engines, where a fuel-air mixture is ignited leading to a constant volume expansion to deliver mechanical work; or one of several other power generating cycles available, several steps are required and each is subject to its own efficiency losses. Established technologies with combined steam and gas turbine cycles with efficiencies of up to 58% are in direct competition. These heavy-duty machines are very complex with 23 different components consisting of 16 different materials (Kettani, 1970).

When compared to conventional power generation, fuel cells offer the following advantages (Oniciu, 1976):

- low environmental impact with respect to SO_x and NO_x emissions,
- high efficiency leading to a reduction of greenhouse gas emissions,
- diversity of fuel feedstocks including natural gas, methanol and coal gas, and
- modularity which leads to faster installation and small stepwise expansion of power output.

The efficiency can be further improved by using the waste heat of high temperature fuel cell reactions in a Carnot cycle (cogeneration) to produce more electrical energy or for reforming the fuel. Fuel cells also have the non-environmental advantages of silent functioning, the possibility of long life, simplicity of use, high energy and power density to weight ratio and the ability to be used as a remote power source.

However, before fuel cells become a commercial reality, a major cost reduction in the power plant system is still needed (Sheppard, 1987). In order to realize this goal the reaction mechanisms involved in each particular fuel cell type must be understood. The components of fuel cells operate in hostile environments with a highly oxidizing cathode atmosphere and a highly reducing anode atmosphere (Minh, 1993). High operating temperatures or expensive noble metal catalysts are necessary to maintain favourable reaction kinetics and mass transfer of reactants to the triple phase boundary layer (Schoonman et al., 1991).

4.1 Fuel Cell Operation

The principles of the fuel cell reactions are identical to batteries. The most outstanding difference is that, in fuel cells, the fuel is constantly replenished to the triple phase boundary. In batteries, a metal or metal compound is reacted at the two phase interface to

form an ion, transported through the electrolyte and reacted again to form another metal compound. Once the reactant is exhausted, the battery is considered to be “dead.” In secondary batteries, a reversed current can be applied to recharge the battery.

In fuel cells, the reaction begins with the adsorption and dissociation of oxygen molecules on the cathode surface. If the electrolyte is an anion conductor, these adsorbed atoms, reduced with the addition of electrons, migrate through the electrolyte to the anode. At the anode the oxygen ions react with the fuel and release the electrons. The interconnect conducts the electrons from the anode to the cathode of the next cell, allowing the electrons to react with more oxygen atoms and complete the circuit. This process is illustrated in Figure 4.1 (Minh, 1993; Kawada and Yokokawa, 1997). Hydrogen cation conducting fuel cells are similar to oxide anion conducting fuel cells, except the oxidized hydrogen ions migrate through the electrolyte. These proton conducting fuel cells (PEM’s or proton exchange membranes), however, will not be discussed here in detail.

Thermodynamically, a fuel cell converts the Gibb’s free energy change (ΔG) of a chemical reaction to electrical energy according to the following equation:

$$\Delta G = n\mathfrak{F}\mathcal{E}_r \tag{4.1}$$

where \mathcal{E}_r is the reversible potential of the cell, n is the number of electrons and \mathfrak{F} is Faraday’s constant. Considering the most common reaction of the fuel cell, i.e. the reaction between hydrogen and oxygen to form water ($\text{H}_2 + \frac{1}{2} \text{O}_2 = \text{H}_2\text{O}$), ΔG° is 237 kJ/mole, n is 2 and therefore, E_r is 1.23 V under standard conditions ($T=25^\circ\text{C}$, $P_{\text{H}_2}=P_{\text{O}_2}=1$ atm, liquid H_2O)

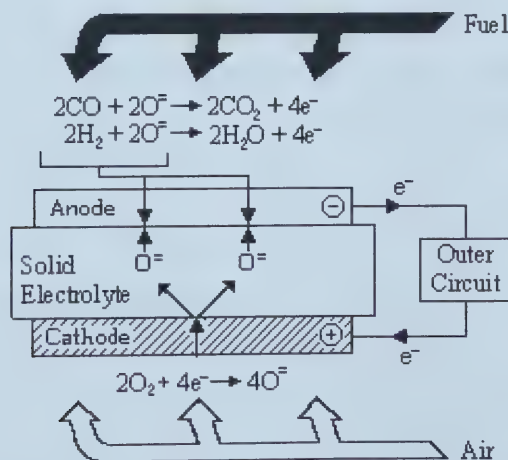


Figure 4.1 - Schematic diagram of the fuel cell reaction (Minh, 1993; Kawada and Yokokawa, 1997).

(Raissi et al., 1997). Since the enthalpy of this reaction is $\Delta H = -285.5 \text{ kJ/mol}$, the maximum electrical energy available is 83% ($\Delta G/\Delta H \times 100$) of the enthalpy change of the fuel oxidation reaction. The maximum percentage that can be converted into electrical energy decreases as the temperature increases for hydrogen oxygen cells (Grubb and Niedrach, 1966).

Fuel cells have two general requirements: reactivity and invariance. Increasing reactivity maximizes the electrical energy released by the reaction by maintaining the proper reactant stoichiometry (ie. only 2 Faradays of electricity are released for the reaction of one mole of carbon to carbon monoxide compared to 4 Faradays for reaction to carbon dioxide). In addition, high reactivity provides high current densities, minimizing the mass and size of the fuel cell stack. Reactivity is controlled in large part by the rates and mechanisms of electrode reactions. By increasing the porosity of the electrodes, pressure or temperature through the use of catalysts, the reactivity is improved (Angrist, 1982).

Invariance entails that a fuel cell should convert energy with little or no change throughout its lifetime. Corrosion, side reactions, sintering, diffusion, catalyst poisoning and pore clogging are deleterious to cell operation and lead to variations in fuel cell performance. Invariance requirements are dealt with by proper materials selection and optimizing operating conditions (Angrist, 1982).

4.1.1 Fuel cell Performance

If all of the reaction steps of the fuel cell reaction were thermodynamically reversible, the potential would remain at 1.23 V over the full operating range. The losses which take place at the electrodes are generally attributed to some form of polarization, which is classified into three categories as illustrated in Figure 4.2: chemical polarization, concentration polarization and resistance polarization. When a load is applied to a fuel cell and a current is drawn, the output voltage drops below the theoretical voltage to an actual value which is written as follows (Angrist, 1982):

$$V_{ac} = V - \Delta V_{conc(c)} - \Delta V_{chem(c)} - \Delta V_{conc(a)} - \Delta V_{chem(a)} - \sum IR \quad (4.2)$$

where c denotes the cathode and a the anode.

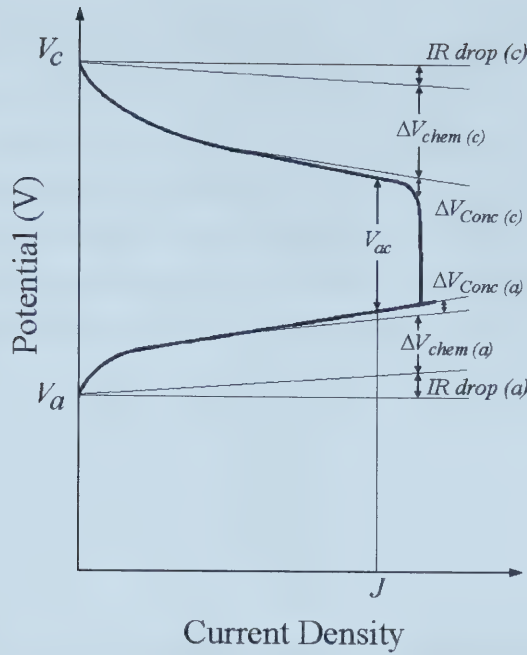


Figure 4.2 - Potential versus current density graph illustrating the various polarizations that affect fuel cell performance (Angrist, 1982).

Resistive Polarization is the result of electrode and electrolyte resistivities. For these types of polarizations, typical material resistivities can be used to calculate the voltage drop as follows (Kettani, 1970):

$$\Delta V_R = \frac{l_{eq} J}{\sigma_{eq}} \quad (4.3)$$

where l_{eq} and σ_{eq} are the equivalent length and conductivity, respectively, and J is the current density. Resistive polarization can only be reduced by minimizing the cell element resistivities through materials selection or cell design. The main contribution to the resistive polarization is due to the electrolyte, especially in electrolyte supported cells. With electrode supported cells, the thickness of the electrolyte can be reduced to 10 to 40 μm and the ohmic resistance due to the electrolyte is significantly reduced (Virkar et al., 2000).

Chemical Polarization, also referred to as activation polarization or overvoltage, is a surface reaction phenomenon for which all reaction and charge transfer steps are included. The magnitude depends on how the ions are discharged at the electrodes and in part upon the rate at which they are discharged and, therefore, depends on the nature of the electrolyte-electrode interface. Energy is required for the chemisorption of the fuel, breaking bonds with the release of electrons and reaction with the electrolyte ion to form a product. This energy must be subtracted from the total energy that is available. The voltage drop due to chemical polarization is represented by the Tafel equation as follows (Angrist, 1982):

$$\begin{aligned}\Delta V_{chem} &= a' + b' \ln J \\ a' &= -\frac{RT}{\alpha n \mathfrak{F}} \ln J_0 \\ b' &= -\frac{RT}{\alpha n \mathfrak{F}}\end{aligned}\tag{4.4}$$

where α represents the fraction of chemical polarization that aids a reaction in proceeding and J_0 is the exchange current density, which are intimately related to the energy barrier. In order to minimize the effects of chemical polarization, it is necessary to maximize the reactive area of the electrolyte-electrode-gas phase boundary or the triple phase boundary (TPB) (Angrist, 1990; Kettani, 1970).

Concentration polarization arises when the fuel is oxidized at the anode and oxidizer is reduced at the cathode. If the surrounding material is unable to maintain the initial ion concentration, “back electromotive force”, which opposes the reversible fuel cell voltage, may be created. Assuming that the diffusion layer thickness is independent of the rate of diffusion, the concentration at the interface can be related to the current density. The voltage loss due to the change in concentration is given by a similar equation to that used to predict the voltage of an electrochemical cell with transference. Assuming that migration of the potential determining ion is negligible and that the ions in the bulk fluid and near the electrode have the same activity coefficients, the concentration polarization is (Angrist, 1990; Kettani, 1970):

$$\Delta V_{conc} = \frac{RT}{n \mathfrak{F}} \ln \frac{c_{if}}{c_b}\tag{4.5}$$

where c_{if} is the concentration at the interface and c_b is the concentration in the bulk. In terms of the limiting current density, J_l (Angrist, 1990):

$$\Delta V_{conc(c)} = \frac{RT}{n\mathfrak{F}} \ln \left[\frac{J_l}{J_l - J} \right] \quad (4.6)$$

This equation refers to a consumptive electrode process where ions are being removed from the electrolyte. At the anode, where the ions are being discharged into the electrolyte and a concentration buildup may occur, the concentration potential is given by (Angrist, 1990):

$$\Delta V_{conc(a)} = \frac{RT}{n\mathfrak{F}} \ln \left[\frac{J_l + J}{J_l} \right] \quad (4.7)$$

Concentration polarization is therefore related to the transport of gaseous species through porous electrodes and, specifically, to the volume percent porosity, the pore size and the tortuosity. Only by increasing the limiting current density can the concentration polarization be reduced. This can normally be accomplished by vigorously stirring the electrolyte or by increasing the temperature (Virkar et al., 2000).

4.1.2 *Electrochemical Impedance Spectroscopy in Fuel Cells*

Electrochemical impedance spectroscopy (EIS) is now a well established technique for investigating electrochemical and corrosion systems. Most of these electrochemical processes involve more than one elementary reaction, often including several adsorbed surface intermediates. EIS is capable of detecting these intermediates because of the precision attainable by signal averaging in the steady state and over a wide range of frequencies with simple instrumentation. As the potential or the current is modulated, the surface coverages (analogous to concentrations) undergo sinusoidal variations with time that ultimately modify the impedance characteristics of the interface, usually allowing the separation of bulk and grain boundary contributions to the overall ionic conductivities of electrolytes (Göpel and Wiemhöfer, 1990; MacDonald, 1991; Wiemhöfer, 1993).

A.c. impedance measurements are made by sweeping the frequency over a specific range (normally 0.1 Hz to 80 kHz). Higher frequencies (> 20 kHz) are required to close the electrode arc to the real axis as the temperature increases above 800°C with the output voltage set to lower than a 10 mV peak allowing analysis with a linear response assumption (Van Herle and Thampi, 1994; Sridhar et al., 1997; Kawada and Yokokawa, 1997). Data analysis is readily performed by plotting the real and imaginary components of the impedance as a function of frequency. Semicircles result in connection with almost all combinations of charge transfer, mass transport, adsorption and homogeneous or heterogeneous reactions,

where the capacitances are of the same order of magnitude (Kurzweil et al., 1989). Even diffusion dominated interfacial reactions can be detected with this technique (MacDonald, 1991; Wiemhöfer, 1993)

A three electrode configuration is used to isolate the impedance response of a single electrode/electrolyte interface: a working electrode to be tested, a counter electrode for current flow and a reference electrode for detecting the equilibrium potential, which is an imaginary line where the ohmic drops of the anode and cathode add equally to give the total ohmic drop. The reference electrode must be reversible to the surrounding gas to get a stable equilibrium potential. The working and counter electrodes should be prepared in a symmetrical way; otherwise, part of the polarization voltage at the counter electrode will contribute to the detected voltage at the working electrode. For a simple and easy setup, the entire cell can be put into an atmosphere in which the working electrode is to be tested. When the behaviour of the counter and reference electrodes in the test gas are not well known, they are exposed to an air flow in order to get a sufficient current and a stable reference voltage (Van Herle and Thampi, 1994; Kawada and Yokokawa, 1997).

The impedance of an R-C circuit is described by the following equation (Kawada and Yokokawa, 1997):

$$Z = \frac{R}{1 + i\omega CR} \quad (4.8)$$

where ω is the angular frequency, $2\pi f$, and the real and imaginary parts of the impedance are as follows (MacDonald, 1991; Kawada and Yokokawa, 1997):

$$\begin{aligned} Z &= Z' + iZ'' \\ Z' &= \frac{R}{1 + (\omega CR)^2}; Z'' = \frac{\omega CR}{1 + (\omega CR)^2} \\ \tan \phi &= -Z''/Z' \end{aligned} \quad (4.9)$$

where ϕ is the phase angle. If ac impedance is measured at variable frequency, a semicircle is obtained on the complex impedance plane as $R^2 = (Z' - R)^2 + Z''^2$. The resistance is obtained from the real axis intersects and the capacitance from the frequency, where the frequency at the top of the circle is $\omega_0 = 1/CR$.

EIS measurements result in a set of semicircles (and straight lines) on Z' versus Z'' plots and the first step of the analysis is to ascribe each of them to bulk properties or

interfacial phenomena. If the difference among relaxation times are large enough, the three processes in the circuit will give three separated semi-circles in the complex impedance plane; otherwise a combined arc results. Usually, the electrode impedance on YSZ or other solid oxide electrolytes have a relaxation time much larger than the bulk and the grain boundary impedance of the electrolyte. Thus, the ohmic loss in the electrolyte can be separated from the electrode impedance (Kawada and Yokokawa, 1997).

Porous electrodes are a complicated system for interpreting frequency dependent impedances and current-voltage relations. Important factors include the geometry and reversible geometrical changes of the porous structure, for instance, due to changes in the ratio of TPB lines to closed two-phase boundaries (Wiemhöfer, 1993). In the case of extremely distorted arcs, the value of R_{gb} and R_e cannot be obtained independently from the loci due to the overlapping situation of two arcs (Matsui, 1992). The electrode impedance is not a single semicircle if more than two reaction steps are included (Kawada and Yokokawa, 1997).

The second step is to apply an equivalent electrical circuit to the system. Equivalent electrical circuits have been used extensively to represent corroding interfaces because the impedance functions often display many of the features exhibited by passive electrical circuits (MacDonald, 1991). A double layer capacitance is commonly used as an explicit element in impedance analysis. This capacitance is placed in parallel with elements which represent different faradaic processes at the electrode. The double layer capacitance of the porous platinum/YSZ interface, measured by potential step chronoamperometry by Robertson and Michaels, 1991, was determined to increase linearly from $0.2 \mu\text{F}/\text{cm}^2$ at 550°C to $1.3 \mu\text{F}/\text{cm}^2$ at 695°C (insensitive to oxygen partial pressure and electrode potential).

Interface phenomena in Ni/YSZ cermet anodes typically consist of two semicircles, with a smaller high frequency loop, whose relative magnitude increases for electrodes with reduced coverage (Kleitz et al., 1981). Primdahl and Mogensen, 1997, deconvoluted their impedance spectra with an $LR_s (R_1Q_1) (R_2Q_2) (R_3C_3)$ scheme. The bulk or solution resistance can be estimated by the following equation (Mogensen and Lindegaard, 1993):

$$R_s = \frac{l}{\sigma A} \quad (4.11)$$

where σ represents the conductivity of the YSZ disk, A the effective electrode areas and l the disk thickness. The conductivity and l are invariant; therefore, the different R_s can be accounted for by the effective Ni electrode area. Even though the apparent electrode area and

Ni content in both electrodes are the same, the effective Ni surface area depends on the microstructure of the cermet electrodes.

Q_{CPE} is the constant phase element (CPE) and is represented in the following equation:

$$Z(f) = \frac{1}{Q_{CPE} \cdot (i\omega)^n} \tag{4.10}$$

where n is a frequency power. If $n = 1$, then Q_{CPE} is a capacitance with $C = Q_{CPE}$, if $n = 1/2$, the Q is a Warburg diffusion impedance, if $n = 0$, then Q_{CPE} is a resistance and if $n = -1$, then Q_{CPE} is an inductance. For Ni/YSZ electrodes (n_1, n_2) = (0.8, 0.75) (Primdahl and Mogensen, 1998). Matsui, 1991 and 1992, used a Warburg impedance ($n_1 = n_2 = 1/2$) for Pt/YSZ cells and the equivalent circuit is easily obtained as a combination of the circuits shown in Figure 4.3.

The higher frequency components R_1Q_1 and R_2Q_2 are closely related with three-phase boundary sites while the lowest frequency component R_3C_3 is relatively insensitive to them. Also, their results indicated that the R_3 values are much smaller than $R_1 + R_2$. The R_3C_3 component has been assigned to the reaction resistance associated with OH^- ions on the YSZ surface. Further, the TPB insensitive behaviour of R_3C_3 has been accounted for with a

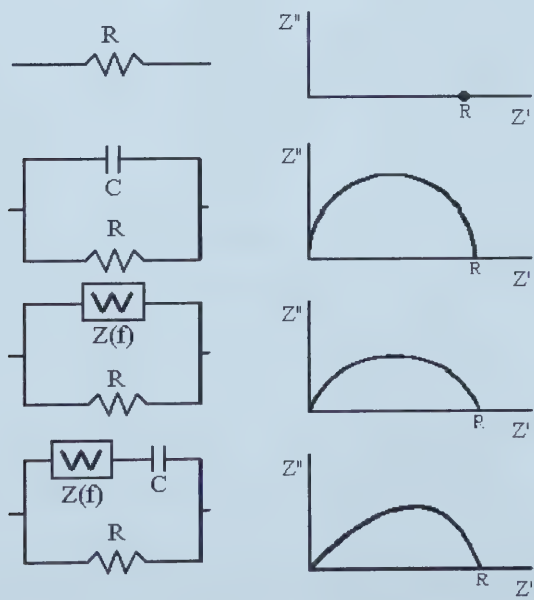


Figure 4.3 - Complex impedance loci for R-C-Z(f) circuits (Matsui, 1992).

premise that this reaction step is not necessarily related with TPB sites since the reaction may take place on the external surface of YSZ next to the TPB sites (Primdahl and Mogensen, 1998).

Lee et al., 1997, found a disagreement where R_3 also sensitively varied with the TPB sites. Thus, it was decided to adopt an $R_b (R_1Q_1) (R_2Q_2)$ scheme, with an expectation that neglect of the R_3C_3 component would not really influence the data analysis because the values are small enough to be ignored. R_1Q_1 and R_2Q_2 components can be assigned to the parallel combinations of the electrode reaction resistance and the constant phase element, based on the fact that the resistance values sensitively vary according to the TPB sites and also to the P_{H_2} in the anode chamber. However, a possible assignment for R_1Q_1 to the impurity phases segregated at the YSZ grain boundary cannot be totally excluded since the time constant for this semicircle is well matched with reported values (Lee et al., 1997).

The occurrence of inductive loops, under electrode polarization, is a known phenomena in wet electrochemistry. It can be modelled by a two step electron transfer process where the intermediate species compete for adsorption sites (Boukamp et al., 1993). It is important not to attach too much physical significance to the inductance observed in

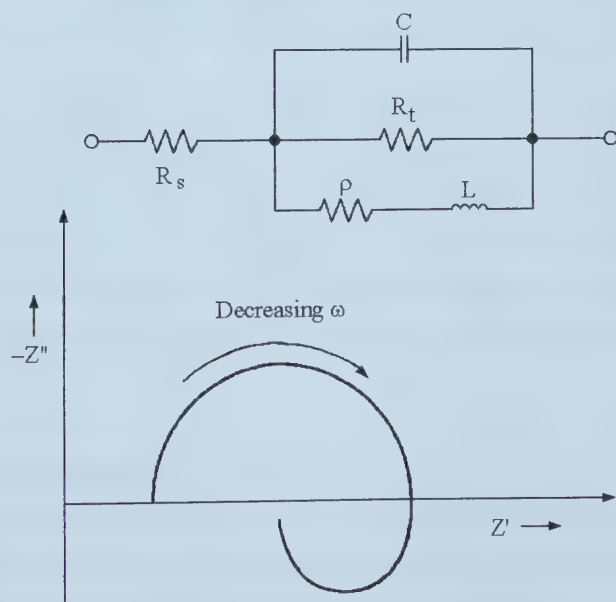


Figure 4.4 - Equivalent circuit and schematic of the complex plane plot where R_s is the solution resistance, C the double layer capacitance, R_t the transfer resistance, ρ the faraidic resistance and L the self inductance (MacDonald, 1991).

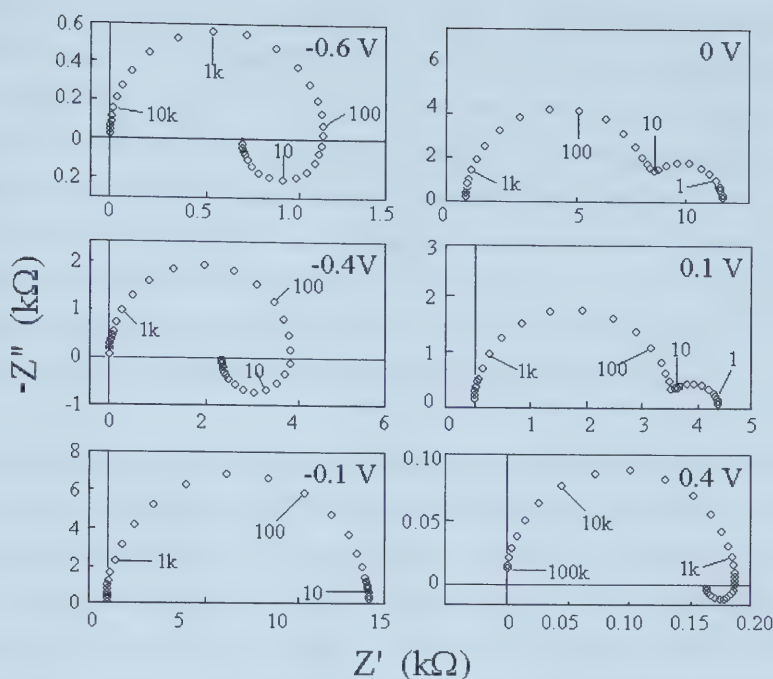


Figure 4.5 - Impedance spectra calculated with stepwise charge transfer model, as a function of polarization (Boukamp et al., 1993).

these systems since induction refers to energy storage in a magnetic field. The inductances of the lead wires affect the impedance arc in the high frequency range. A more realistic interpretation of the fourth quadrant behaviour as seen in Figure 4.4 is in terms of a negative capacitance, but such an element does not exist among passive devices (MacDonald, 1991). Boukamp et al., 1993, determined that inductive loops appeared in O_2 Au/Fe-YSZ systems when anodic or cathodic polarizations are greater than 0.1 V as illustrated in Figure 4.5.

4.2 Fuel Cell Classification

The fuel cells available for use today have great diversity in electrolyte materials, fuel gas utilization and operating temperatures making classification very difficult. They have been classified by some authors according to the method of fuel supply: direct, indirect or regenerative (Papic and Roosdahl, 1986); the operating temperature: low, medium, high, ultrahigh, etc (Breiter, 1969); the physical state or type of fuel used: gaseous hydrogen, lower hydrocarbons, liquid alcohols, hydrazine, higher hydrocarbons, solids, metals, etc; or even by

a combination of electrolyte temperature and materials (Bockris and Srinivasan, 1969; Kettani, 1970). However, these categories do not lend themselves to an adequate description of the diversity inherent in fuel cells. A low temperature fuel cell could define any of the acid, alkaline or polymer based electrolytes, each of which has its own fuel gas limitations and impurity tolerances. High temperature fuel cells can include molten carbonate or solid oxide electrolytes, which are capable of using several reaction gases. By describing these electrochemical devices according to their base electrolyte materials, a broad definition of temperature range and fuel tolerances comes to mind. The variety of fuel cells available is therefore described here according to their primary electrolyte species.

Acid Fuel Cells (PAFC's) typically consist of electrodes composed of finely dispersed platinum catalyst on carbon paper, an SiC matrix containing the phosphoric or sulphuric acid and a bipolar graphite plate with flow channels for fuel and oxidant. The operating temperature ranges between 60 and 220°C and it can use either hydrogen, hydrogen produced from hydrocarbons (reformed natural gas) or alcohols as the anodic reactant. In the case of hydrogen produced from an air reformer as the anodic reactant, a temperature of 200°C and a pressure of 8 atm are required for better performance (Papic and Roosdahl, 1986; Raissi et al., 1997).

PAFC's are advantageous from a thermal management point of view. The rejection of waste heat and product water is very efficient in this system and the waste heat at 200°C can be used efficiently for the endothermic steam reforming reaction. However, this system is extremely sensitive to CO and H₂S, which are commonly present in reformed fuels. Also, PAFC's are subject to slow start up (preheating), liquid electrolyte management problems, high costs and excessive weight. PAFC's work best at constant output requiring the use of hybrid systems, where a battery meets any high energy demands on the system (Papic and Roosdahl, 1986; Raissi et al., 1997).

Alkaline Fuel Cells (AFC's) are the oldest and most widely used fuel cell systems in the U. S. space program and have been onboard most manned space missions. A 30% to 75% aqueous solution of potassium hydroxide or saturated solutions of potassium carbonate-bicarbonate are used as the electrolyte with hydroxyl ions as the conducting species (Papic and Roosdahl, 1986). The operating temperature is between 60 and 120°C, which is relatively low compared with other types of fuel cells with atmospheric operating pressures. In space shuttles, closed loop hydrogen circulation as well as dielectric liquid circulation is

used for heat management. Terrestrial fuel cells are process air-cooled. (Raissi et al., 1997).

AFC's have the advantages of cold start capabilities, high power density and, because of the nature of the alkaline electrolyte, no noble metal catalyst is required reducing the associated costs. However, removal of product water and heat is difficult at these low temperatures. In addition, AFC's can only operate with pure H_2 and O_2 . Even a small level (<250 ppm) of CO_2 is sufficient to carbonate the electrolyte and spoil the electrode. Several processes for cleaning the electrode after contamination are available (physical adsorption-Selexol process, Fluor solvent process, pressure swing adsorption), although they are expensive and never completely effective (Raissi et al., 1997).

Molten Carbonate Fuel Cells (MCFC's) possess molten alkali (lithium or potassium) carbonate mixture electrolytes, retained in a porous lithium aluminate matrix, which conduct carbonate ions. Oxygen and carbon dioxide are combined at the cathode with available electrons to form the carbonate ions which react at the anode with hydrogen. Operating temperatures range from 600 to 800°C, producing suitable quantities of high quality waste heat (Papic and Roosdahl, 1986).

MCFC's normally have 75% hydrogen utilization. The advanced form of MCFC referred to as internal reforming molten carbonate fuel cell has the potential to consume lower hydrocarbons (CH_4) directly. It is intrinsically efficient (>50%) since the heat produced at the anode is used for reforming hydrocarbons, for cogeneration, or for a bottoming cycle. MCFC's have the advantage that they do not suffer from CO poisoning and, in fact, use CO in the anode gas as the fuel. They are extremely sensitive (1 ppm) to the presence of sulphur in the reformed fuel or oxidant gas stream. The presence of HCl, HF, HBr, etc. causes corrosion, while trace metals can spoil the electrodes. The presence of fine particulates of coal and ash in the reformed fuel can clog the gas passages (Raissi et al., 1997). Other concerns typical of MCFC's are anode sintering, cathode dissolution, electrolyte evaporation, stack mechanical design and thermal cycling (Papic and Roosdahl, 1986).

Solid Polymer Fuel Cells or proton exchange membrane fuel cells (PEMFC's) use a proton (hydrogen ion) conducting membrane which stays sandwiched between two platinum catalysed porous electrodes. Initially, these membranes were based on polystyrene, but at present, a Teflon-based Nafion™ is used, offering high stability, high oxygen solubility and high mechanical strength. The cell operating temperature is quite low - 80 to 90°C - and operating pressures can range from 1 to 8 atmospheres of humidified hydrogen and oxygen.

Operation at high pressure is necessary to attain high power densities, particularly when air is chosen as the cathodic reactant (Khandkar and Joshi, 1993; Raissi et al., 1997).

The main practical advantage of the polymer electrolytes is that they can be tailored to yield materials that are a good compromise between liquid and solid electrolytes. Due to their high power density, small size, rapid startup and variable power output, PEMFC's have a great advantage over other types of fuel cells. The main drawbacks are the relatively low ambient temperature ionic conductivity, CO intolerance, limited fuel variability (only pure H₂) and relatively high anion mobility (which is akin to electron transport). Even a trace amounts of CO can drastically reduce performance, precluding the use of reformed fuels (Khandkar and Joshi, 1993; Raissi et al., 1997).

Solid Oxide Fuel Cells (SOFC's) are solid state power systems that most commonly use fluorite-type oxides, as discussed in Section 3.3, as electrolyte materials. The SOFC system has the simplest design of all of the fuel cells, but because of the high operating temperatures (750-950°C), it is still mostly on a laboratory scale. Slow start-up, thermal stresses created by different thermal expansion coefficients of the cell components between ambient and high operating temperatures, and complex materials problems, including electrode sintering, interfacial diffusion and reactions between components cause difficulties in the assembly and long term operation of fuel cell stacks (Watanabe et al., 1996; de Souza et al., 1997a; Raissi et al., 1997).

High operating temperatures provide several advantages that are unique to SOFC's and MCFC's. Primarily, severe restrictions on the type and purity of fuel are reduced, as the need to prevent catalyst poisoning or the formation of reaction products is eliminated. Catalysts are not required and the electrolyte is highly stable, lessening concern over fuel impurities. SOFC's operate equally well on dry or humidified hydrogen (no pore flooding), carbon monoxide fuel or on fuel mixtures. The foremost poisoning factor is H₂S and even then the tolerance level is two orders of magnitude greater than other fuel cells (up to 80 ppm) (Julien, 1990; Raissi et al., 1997; Antonucci et al., 1997). There are even some SOFC's which have been developed which use H₂S as the primarily fuel, although they are more for environmental purposes than for high power density (Peterson and Winnick, 1998).

Although there are benefits to high temperature operation, by lowering the operating temperature to between 500 and 700°C, a wider selection of materials are available to be used as electrodes and interconnects to improve the relatively high electrode resistivity, while maintaining the advantages of a high temperature fuel cell. Approaches to minimize resistive

losses across the electrolyte have included replacing YSZ by alternative electrolyte materials with higher ionic conductivities, and/or reducing the thickness of the electrolyte from that in conventional cells of 100 to 200 μm to approximately 10 μm (Papic and Roosdahl, 1986; de Souza et al., 1997b).

The YSZ IR drop is estimated from the known conductivity and thickness of the electrolyte. Even at very high current densities, the voltage drop due to a 10 μm YSZ electrolyte film is almost negligible. The remainder of the ohmic drop is probably due to contact resistance at the cathode/electrolyte interface as well as minor losses across the current collectors. Polarization of the electrodes (η_a and η_c) account for about 40% of the total voltage drop. Cathodic polarization was larger than the anodic polarization, which was almost negligible for current densities below 2.0 A/cm². The YSZ electrolyte IR drop represents about 18% of the total voltage drop. Current interrupt methods indicate the majority of the voltage loss at high current density is due to ohmic losses, most likely associated with cathode/electrolyte contact resistance (0.1 $\Omega\text{ cm}^2$) (de Souza et al., 1997a).

4.3 Materials for Solid Oxide Fuel Cells

4.3.1 Interconnect

In the design of fuel cell stacks, individual cells must be interconnected through a material that acts as both a fuel/oxygen separator and as an electron conductor. Interconnection materials have several requirements that put strong limitations on the materials that can be used. They should (Minh, 1993; Lindroth et al., 1996):

- be pure electronic conductors (very little ionic conduction can be tolerated)
- be chemically stable in both oxidizing and reducing atmospheres,
- be gas tight to both oxygen and the fuel,
- have a thermal expansion coefficient that closely matches those of the other fuel cell components, especially the electrolyte, from room temperature to the operating temperature,
- not be chemically reactive with the other fuel cell components, and
- be inexpensive.

Titanium and chromium oxides meet most of these requirements, with the appropriate valence stability over the oxygen potential range for SOFC's. CaTiO_3 and SrTiO_3 do not achieve sufficient electronic conductivity with doping. Presently, LaCrO_3 (doped with CaO , SrO or MgO) is the leading candidate for use as the interconnect. LaCrO_3 is a p-type

semiconductor and, although its conductivity is not high enough on its own, doping does improve the conductivity. Strontia doping provides more stability, but requires a higher sintering temperature (1700°C) to achieve acceptable densities (Winkler and Keoppen, 1996) and an inert atmosphere to prevent CrO_3 vaporization. (Kawada and Yokokawa, 1997).

Calcia doping has been found to suppress vaporization, allow densification in air, and reduce the sintering temperature (around 1300°C) through the formation of low melting temperature Ca-Cr-O_x compounds. Alkaline earth dopants also result in a close thermal expansion match with YSZ. LaCrO_3 doped with the alkaline earth oxides exhibit enhanced p-type conductivity due to the fact that substitution of La ions with alkaline earth ions gives rise to the formation of Cr^{4+} . However, with decreasing oxygen potential, tetravalent chromium ions reduce to form oxide ion vacancies at the expense of electron holes. This change in the valence state causes electronic conductivity to decrease, volume expansion due to oxide ion vacancy formation and oxygen permeation due to the increase of ionic conductivity (Kawada and Yokokawa, 1997).

There are several reasons why interconnect materials should preferably be made of alloys as follows (Linderroth et al., 1996):

- much lower materials costs,
- greater strength and workability,
- improved electrical conductivity (approximately three orders of magnitude higher than LaCrO_3), and
- a higher thermal conductivity, reducing thermal stresses due to temperature gradients within the fuel cell stack and the need for cooling with excess gas flow.

Several alloys and composites have been tested, including $\text{Cr-5Fe-1Y}_2\text{O}_3$, H-230, IN601, IN657 and APM (Fe-22Cr-5.8Al-Ce). Two major problems have been pointed out in the use of alloy separators. Contact resistance increases due to the formation of surface oxide layers (usually chromia, silica or alumina) and the difficulty in obtaining a thermal expansion match with the other cell components. APM (an alumina former) exhibits the best corrosion resistance at 850 and 1000°C, but poor electrical conductivity even though the oxide layer is thin makes them unattractive (Linderroth et al., 1996).

From a thermal expansion coefficient standpoint, chromium alloys appear to be the best candidate, but modifications of the alloys must be made to reduce the chromia formation rates and to improve the conductivity of the resulting layer. Like lanthana chromate, the most severe materials problem related to the chromia forming alloys is CrO_3 vaporization, which

can migrate to the cathode-electrolyte interface and deposit, degrading cathodic activity (Kawada and Yokokawa, 1997).

4.3.2 *Electrodes*

As a result of recent advances in deposition technologies that have significantly reduced the ohmic resistance of electrolytes, the oxygen electrode reaction is now the rate limiting step in the oxygen transfer process (Boukamp et al., 1993). An electrode can be defined as a “location in a chain of electric conductors where the conductivity changes in nature from ionic to an electronic conductivity.” This transition can occur either as a discontinuity at a phase boundary or as a gradual change in a single-phase material (Kleitz, 1981). Electrodes should have the following properties to be effective (Hammoche et al., 1993; Verweij, 1998; Wilkenhoener et al., 1999):

- a fully connected electrode network with high electronic conductivity,
- long term functionality (i.e. resistance to sintering),
- physical compatibility with the other cell components (i.e. similar thermal expansion coefficient as the electrolyte and interconnect),
- chemical compatibility with the other cell components (i.e. no reaction byproducts with the electrolyte and interconnect),
- a fully interconnected porosity with a high permeability to both the fuel or air and reaction products,
- good electrocatalytic ability with an abundance of active sites for the electrode reactions to take place, and
- ionic conductivity, while not essential, has recently been demonstrated to enhance the electrode reactive area.

Lowering the SOFC operating temperature to below 700°C is of interest in allowing the use of low cost, high performance materials for the cell and the balance of the power plant (such as ferritic stainless steels for interconnects discussed in Section 4.3.1), reducing the stack thermal insulation requirements and increasing cell life through reduced thermal degradation and thermal cycling stress. Moreover, there are indications that direct oxidation of methane is possible without carbon deposition at temperatures below 650°C, removing the need for fuel reforming (Tsai and Barnett, 1997). However, the temperature dependence of electrode polarization is reported to be very large, especially at the cathode, which becomes the dominant factor in efficiency loss as the operating temperature is reduced (<800°C) (Kawada and Yokokawa, 1997).

If the bulk materials are found to be chemically and physically stable under SOFC operating conditions, electrode kinetics and electrocatalysis are the next parameters of importance (Göpel and Wiemhöfer, 1990). Electrocatalysis is the acceleration of an electrode reaction by a substance that is not consumed in the overall reaction and is mainly concerned with the search for materials that have a high exchange current density for electrode reactions. Electrocatalysis is a special case of heterogeneous chemical catalysis, but with the one major difference that one or more of the intermediate charge-transfer steps is in the overall reaction. Adsorption, charge transfer and surface reactions are the three main processes in which the catalyst can play a role in electrochemical reactions (Bockris and Srinivasan, 1969).

The work function, or the energy required to remove an electron from the bulk of the metal to a point well outside of it, is primarily a bulk property of the solid, although it is strongly affected by the nature of the surface. Even in the case of a pure metal, the work function depends on the crystal plane. It is affected by surface impurities that create surface dipoles which affect the potential gradient through which the electron must pass. If the negative end of the dipole is away from the surface, the work function is increased (Bockris and Srinivasan, 1969). In general, increasing the work function weakens the chemisorptive bond of electron acceptor adsorbates such as oxygen. Over wide ranges of catalyst work function, the catalytic rate is exponentially dependent and catalytic activation energy is linearly dependant on the work function (Vayenas et al., 1995).

Upon varying the catalyst potential via a potentiostat, not only are the electrocatalytic (net charge transfer) reaction rates affected, but also the catalytic (no net charge transfer) reaction rate changes in a dramatic, controlled and reversible manner. The steady state increase in the catalytic reaction rate can be at least a factor of 100 higher than that of the open circuit (unpromoted) catalytic rate and up to 3×10^5 times higher than the rate of ion supply to the catalyst via the solid electrolyte. This is why this effect has been termed the non-Faradaic electrochemical modification of catalytic activity (NEMCA) effect (Vayenas et al., 1995). Zipprich et al., 1995, confirmed that the work function (NEMCA effect) is indeed at least partially controlled by the electrode potential. The steady state surface concentration of oxygen species is determined by the balance between transport in the bulk, desorption and reaction at the surface.

It has been proposed that the NEMCA effect is due to an electrochemically induced and controlled spillover of ions, which are less reactive than chemisorbed oxygen, from the solid electrolyte onto the catalyst surface. The spillover ions are accompanied by their compensating charge in the metal, thus forming spillover dipoles. The presence of spillover

dipoles and the concomitant change in work function alter the strength of the chemisorptive bond of covalently bonded reactants and intermediates, thus changing activation energies and reaction rates. In the case of NEMCA, the distances covered by spillover ions are surprisingly long (1-40 μm); yet the spillover ion hypothesis was consistent with the measured work function changes and catalytic rate relaxation time constant upon constant current application. Spillover ions establish an effective electrochemical double layer which, via electrostatic or through-the-metal interactions, affects the chemisorptive bond strengths causing the observed dramatic changes in catalytic rates. It thus appears that the physicochemical origin of NEMCA is closely related to the very interesting electrical polarization and work function change-induced effects on the chemisorption. On the basis of these observations and similar conclusions reached for Na^+ conductors via Na/Pt initial dipole moment measurements, one can conclude that, in general, solid electrolytes can act as dopant donor phases to significantly enhance metal catalyst performance. In the case of YSZ, the resulting catalyst material, i.e. Pt “decorated” with O^{2-} (or O^-) is unique in that gas-phase supplied O_2 cannot produce the same surface species. This then can explain its remarkable catalytic properties (Ladas et al., 1993; Vayenas et al., 1995).

Cathode. As discussed in Section 4.1, oxygen at the cathode passes through the porous structure of the cathode and is supplied to the electrolyte by the dissociative adsorption of oxygen molecules on the electrode. The mechanisms involved in the reduction of oxygen molecules to O_{ads} and then to O^{2-} are in dispute. Liu and Khandkar, 1992, maintain that the reduction of oxygen molecules to oxygen anions involves four elemental steps as follows:

1. Adsorption of oxygen molecules at the gas/electrode interface,
2. Dissociation of adsorbed oxygen molecules to oxygen atoms,
3. Surface diffusion of the oxygen atoms from the adsorption site to the triple phase boundary (TPB), and
4. Reduction of the oxygen atoms to oxygen anions (this step may involve two reaction steps with two electron charge transfers).

Boukamp et al., 1993, contend that the electron transfer step may take place at either of the adsorption or dissociation steps. The model developed by Suzuki et al., 1994, is similar to the model above except that some of the adsorbed O_2 on the cathode surface dissociates and reduces to O^{2-} and transports through the cathode bulk phase. In this model, it is assumed that the electrode has some ionic conductivity. In a study by Mizusaki et al., 1987a and

1987b, on platinum electrodes, it was determined that above 600°C the two mechanisms take place in parallel. However, below 500°C, the surface diffusion rate slows and most of the oxygen atoms are supplied by the direct adsorption of oxygen atoms at the TPB, as the activation energy for surface oxygen atom diffusion is high.

The surface of the cathode is the dominant factor in the electrode reaction, which suggests oxygen adsorption is the rate limiting step. The charge-transfer electrochemical step is relatively rapid and, therefore, remains near equilibrium during current flow. The current then depends on the rate at which oxygen adsorbs and desorbs and varies with the surface coverage of oxygen (Isaacs et al., 1981).

It has been claimed that up to 65% of the total ohmic loss can be attributed to the cathode in SOFC's (Shi-Zhen et al., 1994). Most recent efforts have concentrated on improving cathode performance through refinement of the morphology and electric properties. Materials selection for cathodes faces extreme limitations, as the cathode environment is highly oxidizing (Hammouche et al., 1989; Kawada et al., 1992a; Labrincha et al., 1993). While most metals oxidize too quickly in the cathode environment, noble metals can be used. Silver, platinum and gold have good catalytic activity, in that order, with silver being by far the best cathode material. The calculated activation energies for all of the air electrode materials (except for silver) are all larger than those for the electrolyte resistivity. Consequently, lowering the fuel cell operating temperature is more detrimental to the cathode reaction rate than to the electrolyte ohmic drop, with cathode polarization becoming the dominant factor in the efficiency loss as the temperature decreases below 800°C (Baker et al., 1997).

Silver is a highly desirable alternative to conducting oxides for the air electrode, since it combines the good catalytic activity of the noble metals with high oxygen solubility and excellent conductivity properties, such that a 1 μm thick electrode would be sufficient to eliminate ohmic losses. Silver electrodes show a reversible oxygen electrode reaction on YSZ down to room temperature. Chemisorbed oxygen dissolves as interstitial oxygen in the bulk of the silver electrode, diffuses through the bulk towards the YSZ/silver interface where it is reduced. The bulk diffusion of oxygen atoms through the silver, which is effectively a mixed conductor, is the rate limiting step for oxygen reduction in the temperature range of 650 to 900°K (Zipprich et al., 1995). However, despite its advantages, silver has always been disqualified for use in high temperature fuel cells because of its high volatility (Kawada and Yokokawa, 1997). After one year of operation, 2 μm would be lost at 800°C, although extrapolations based on vapour pressure show that only about 50 nm of material would be

lost at 700°C and about 300 nm at 750°C in the same time period. It would be necessary to apply a cap to minimize vaporization and codeposit an oxide to minimize sintering even at these lower temperatures (Barnett, 1990).

Outside of the noble metals, the most promising materials are the perovskite-type oxides which have an ABO_3 structure. These oxides have high stability in oxidizing environments and good electronic and, in some cases, ionic conducting properties. The electrocatalytic activities of the perovskite materials for the dissociation of oxygen and hence lowest polarization proceed in the order $LaCoO_3 > LaFeO_3 > LaMnO_3 > LaCrO_3$. $LaCoO_3$ and $LaFeO_3$ based perovskites should, therefore, be the best materials for the air electrode. However, at high temperatures they demonstrate strong reactivity with YSZ, forming an electrically insulating layer at the interface in addition to having large thermal expansion mismatches (Takeda et al., 1987; de Haart et al., 1991a; Kawada and Yokokawa, 1997).

$La(Sr,Ca)MnO_3$ (LSM or LCM) has been confirmed as the most suitable perovskite material for use as a cathode in SOFC in the absence of a better alternative. Suzuki et al., 1994, affirm that there is a general dispute as to whether diffusion occurs only on the surface or on the surface and through the bulk of this material, although most now agree that oxygen ion motion to the TPB proceeds by a combination of both mechanisms. In measuring the interfacial capacitance (measured at 35 F/cm² with 0.5 mV and 17.5 mC/cm²), the diffusion rate (5×10^{16} oxygen ions/cm²) is too high to be attributed entirely to ions which were adsorbed on the surface. Therefore, although surface roughness may be taken into account, it is not the only cause of such a large interfacial capacitance.

LSM, while not as reactive as Co and Fe based perovskites, still has undesirable reactions which can occur with the electrolyte. The fundamental reactions can be categorized into: dissolution of oxides into the electrolyte, precipitation of yttrium complex oxides, precipitation of zirconium complex oxides and the permeation of oxygen molecules through the electrolyte. These reactions can occur either during operation (up to 1000°C) or during fabrication (sintering at 1200°C to 1500°C) (Yokokawa et al., 1990; Stochinol et al., 1995). At high temperatures, MnO_2 slowly diffuses into the electrolyte. Manganese oxide doping of yttria stabilized zirconia can reduce the ionic and increase electronic conductivity, but in practical cell operation, the diffusion of Mn into the electrolyte may not be a serious problem (Kawada et al., 1992a).

While the diffusion of Mn into the electrolyte may not have serious adverse affects on the performance of YSZ electrolytes, it does result in an increase in the activity of lanthana and strontia at the interface, leading to the formation of $La_2Zr_2O_7$ and $SrZrO_3$, which have a

conductivity two to three orders of magnitude lower. Interfacial chemical reactions are the leading cause of degradation in fuel cell performance (Ivers-Tiffée et al., 1991; Kawada et al., 1992a; Chiodelli and Scagliotti, 1994; Stochinol et al., 1995).

If reducing the fabrication temperature is not sufficient to reduce the diffusion of manganese oxide, there are two other means to reduce the chemical reactions that take place at the interface. First, excess manganese oxide can be added to prevent increased lanthana and strontia activity (Kawada et al., 1992a). This also has the benefits of improving the conductivity, adhesion, thermal expansion compatibility and sinterability of the perovskite to a maximum occurring at 10 % A site reduction (Shi-Zhen et al., 1994; Claussen et al., 1994). Second, strontia doping of the A-site has also been found to reduce interfacial reactions. $\text{La}_2\text{Zr}_2\text{O}_7$ reaction products resulted when $x < 0.3$ and SrZrO_3 reaction products formed when $x > 0.3$ in $\text{La}_{1-x}\text{Sr}_x\text{MnO}_3$. No reaction products could be detected by X-ray diffraction when $x = 0.3$. The lowest level of reaction products was observed when a combination of Sr doping and A-site substoichiometry was used. $\text{La}_{0.65}\text{Sr}_{0.3}\text{MnO}_3$ did not display any evidence of reaction products after annealing at 1670 K for 200 h (Shi-Zhen et al., 1994; Stochinol et al., 1995).

Anode. Most recent research has concentrated on the cathode, as it is responsible for most of the electrode polarization. As a result, the elementary steps of the anodic reaction are less investigated and understood. In addition, the use of different fuel gases leads to a multitude of electrocatalytic reactions adding to the complexity of the system (Sridhar et al., 1997). The materials selection of an appropriate SOFC anode for hydrogen oxidation is less crucial than that of the cathode material, as there is a much narrower variation in electrochemical performance (Baker et al., 1997).

The reducing conditions created by the electrochemical reaction of oxygen with the fuel permits the use of metals as anode material. The ordering of the specific current in humidified hydrogen is $\text{Fe} > \text{Co} > \text{Cu} > \text{Ni} > \text{Pt} > \text{Mo} > \text{Au} > \text{Ag}$ and can be used as an index of catalytic activity (Isaacs et al., 1981). Nickel is most commonly used because of its high catalytic activity, high temperature stability and low cost in comparison with platinum, cobalt and palladium (Minh, 1993). It is interesting to note that under anodic atmospheres, silver is a poor electrode material - even worse than gold. Silver exhibits very high overpotential and enormous capacitive effects, which are related to the high oxygen diffusivity and solubility in the material. This simply confirms that the elementary processes of hydrogen oxidation are different from those of oxygen reduction (Baker et al., 1997).

In order to keep the metal from sintering over time at high temperatures and becoming impermeable to the fuel, or separate from the electrode bulk, resulting in unconnected metal islands, a ceramic-metal composite or cermet is commonly used. With cermets, sintering of the metal phase and the thermal expansion differences between the anode and the electrolyte can be reduced. In the case of yttria stabilized zirconia (YSZ) electrolytes, a Ni/YSZ cermet is used, because the thermal expansion coefficient of the electrolyte and the cermet are very close (Minh, 1993; Kawashima and Hishinuma, 1996). The ideal Ni content is 45%. Total resistances decrease with the Ni content in the range of 25% to 45%. The minimum resistance occurs at 45%; then the resistance begins to increase once again. The minimum at 45% suggests that at this composition the chance for Ni/YSZ contact and channel formation is the most probable with an increase in the number of active sites (the morphology will be discussed further in Section 4.4.2). Poor wetting of solid electrolyte grains by the metal, however, may still result in the spontaneous sintering of neighbouring metal particles. While electrode resistance observed with the 25% and 35% Ni are initially higher, they tend to stay at the initial values even after prolonged operation. In 45% to 65% cermets, however, the resistance steadily increases with time, with the rate of increase most apparent in the 65% Ni cermet (Lee et al., 1997; Ioselevich et al., 1997; de Boer et al., 2000).

Several attempts have been reported to improve the stability and the performance of the cermet anode by adjusting the Ni content, particle size and Ni dispersion in the cermet, and by control of the preheating and heating temperatures (Nakagawa et al., 1999). The key factor for successful results with these cermets seems to originate from a proper selection of the powder mixture. Utilization of NiO and YSZ powders of a similar size provides a well developed network structure along with many TPB sites for electrode reaction which are easily accessible to the gas (Lee et al., 1997). Coarse YSZ particles are essential for the formation of a YSZ frame which keeps the volume unchanged. Even so, coarse YSZ particles alone are not adequate to achieve long term stability, since slight changes in the volume and the porosity were still observed. The addition of fine YSZ particles is effective in achieving more stable anodes without any substantial decrease in the electrical conductivity and altering of the microstructural configuration (Itoh et al., 1997; Jang et al., 2000).

Platinum. Since platinum is the primary electrode material used in this study, it is important to understand its properties in both electrode environments. The measured impedance responses of Pt electrodes on YSZ can be accounted for in a Randles type of circuit. The circuit may be described through the following equation: $LR_{B+GB}(Q_{dl}(R_T(R_DQ_D)))$

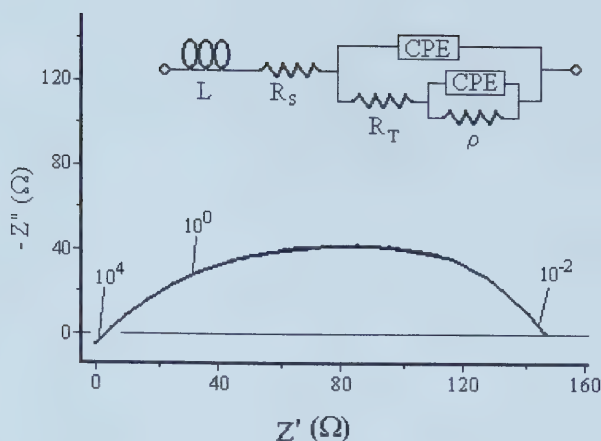


Figure 4.6 - Measured impedance Spectrum at 700°C and 1 atm O₂ and its equivalent circuit (Velle et al., 1991).

as illustrated in Figure 4.6 where L is an inductor, R is a resistor and Q the constant phase element (Velle et al., 1991). The geometry of the electrode interface changes reversibly with the electrode potential. At high electrode potentials corresponding to high oxygen partial pressures, small platinum clusters are formed whereas, for low oxygen partial pressures, platinum spreads out, covering a large part of the electrolyte and reducing the number of reactive sites. Oxygen deficient interfaces under low oxygen partial pressures are characterized by partially reduced zirconia, bonding more strongly to the platinum metal. This explains why the adhesion of platinum and other electrode materials on YSZ is improved by a preceding reduction of the YSZ surface (Wiemhöfer, 1993).

Upon passing a current over a long period of time, the electrode impedance increases irreversibly by a factor of about two. An even bigger increase (by a factor of 10) was obtained after treating the cell in a hydrogen atmosphere. SEM observations of the platinum electrode before and after exposing the electrode to reducing atmospheres reveals that the Pt particles have sintered to a considerably denser structure, thereby closing pores and contracting the TPB. This has made the average diffusion distance for the adsorbed oxygen atoms longer. Figure 4.7 illustrates impedance plots of platinum before and after exposure to a hydrogen environment. After exposure, the arc is no longer symmetrical and shows a lagging tail at the low frequency end. The original equivalent circuit can no longer be retained. In general, the impedance increases with decreasing pressure of air or oxygen (200 mbar to 0.01 mbar), but always retains the arc shape (Van Herle and McEvoy, 1993).

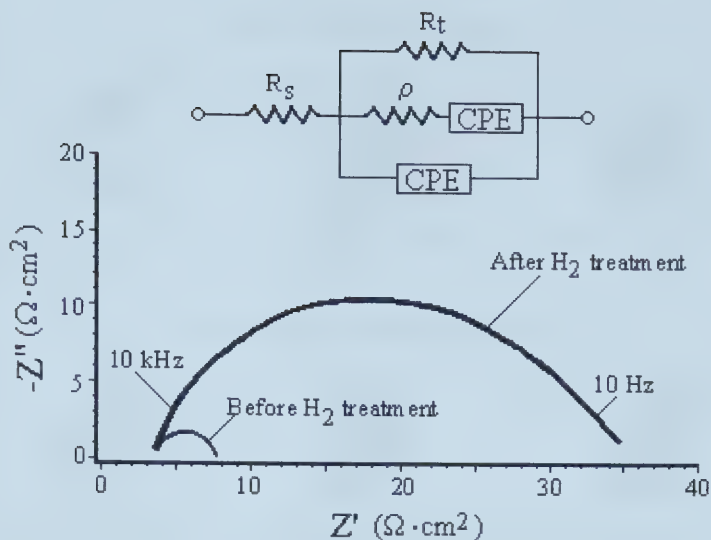
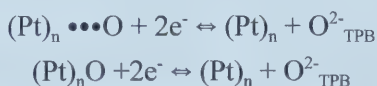


Figure 4.7 - Impedance spectrum at 800°C of platinum electrodes for YSZ fuel cells before and after reduction in a hydrogen environment (van Herle and McEvoy, 1993).

Sridhar et al., 1997, proposed that O_{ads} species can be loosely and reversibly bound at certain sites on Pt electrodes, including the TPB's, depending on the oxygen partial pressure in the gas phase. Current passage will change the local oxygen concentration at the TPB, which may also change the concentration of the reversibly bound oxygen ($(Pt)_n \bullet\bullet\bullet O$) and partially oxidized species ($(Pt)_nO$) according to the following reactions:



When these oxygen structures are present at the TPB, the number of effective charge transfer sites is decreased, thereby increasing the interfacial impedance. From the above equations, it is seen that an anodic current (oxygen is supplied to the TPB from the direction of the YSZ electrolyte) leads to a decrease in the number of charge transfer sites, thereby inhibiting the oxygen-transfer reaction. A cathodic current (oxygen is extracted from the TPB and incorporated into the YSZ electrolyte) increases the concentration of charge-transfer sites and leads to electrocatalysis. The proposed model is described in Figure 4.8 and agrees with observed impedance spectra in oxygen rich atmospheres. Similarly, the chronoamperometry results of Robertson and Michaels, 1991, indicate that after current interruption the transient response seems dominated by the adsorption of oxygen. The currents used by them were an order of magnitude higher than that of Sridhar et al., 1997.

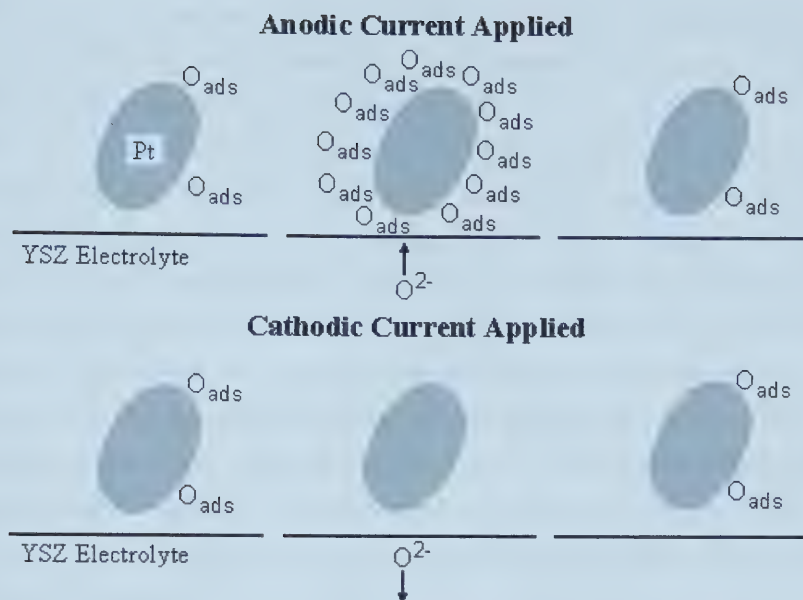


Figure 4.8 - Reversible surface adsorbed oxygen coverage on a platinum cathode due to anodic and cathodic current. Coverage is shown for before, during and after current passage (Sridhar et al., 1997).

In an argon environment, the impedance spectra decreased immediately after the interruption of an anodic current which apparently contradicts the model presented above, but in oxygen poor atmospheres the concentrations of oxygen species is low and the steady state polarization resistance is accordingly fairly large. Since an anodic current leads to a local increase in P_{O_2} , polarization resistance in oxygen poor atmospheres decreases. Sintering of the porous platinum is avoided by using much lower current densities and significantly shorter exposure times.

4.4 Electrode Morphology

The broad performance characteristics reported for conventional electrodes clearly indicate that the electrode processing and microstructure are also decisive parameters (Baker et al., 1997). SOFC electrode kinetics are largely determined by the density of the TPB and the defect chemical condition of the region near the TPB including the build up of space charge, segregation of impurities, and deviations from bulk electronic structure (Verweij, 1998). Despite low ohmic contributions, area specific resistance (chemical and concentration

polarization) may be several times larger. A reduction in the overall area specific resistance of cells and a concomitant improvement in cell performance can be achieved only through improving electrode morphology (Virkar et al., 2000).

The design of an electrode microstructure for low overpotential is one of the most important technologies, because the overpotential is sensitive to electrode/electrolyte contact, particle size, porosity, surface roughness, etc., and directly affects the energy efficiency of the cell. The sensitivity of the microstructure mainly arises from the electrode reaction that occurs at the TPB (Nakagawa et al., 1999). Comparisons of electrical conductivity and the H_2/H_2O partial pressures between compact and pattern electrodes determined conclusively that the reaction site for the rate determining process (adsorption or surface diffusion) was the nickel surface close to the TPB layer (Mizusaki et al., 1994). One may identify the length of this boundary layer as the single most important geometrical parameter affecting electrode kinetics (Sunde, 1995). The optimal structure of the electrodes is a competitive interplay of five functions as follows (Abel et al., 1997):

- A voluminous metal/solid electrolyte/pore space for reaction events,
- Continuous electronic conductivity passage through metal clusters from the TPB to the current collector,
- Continuous transport of oxygen anions through the solid electrolyte clusters in the electrode from the electrolyte to the TPB,
- A large TPB to facilitate a large number of reaction acts (i.e. current generation) per unit volume, and
- Mechanical stability of the junction between the current collector and the electrolyte.

To obtain minimum ohmic losses with a constant layer thickness, the electrode layers should have a low porosity, but dense electrode layers block gas phase mass transport, resulting in high concentration polarization losses. Bonds between the metal and electrolyte sites are active only if they have a neighbouring pore which belongs to a continuous cluster of pores connected to the current collector/gas channel side of the anode (Abel et al., 1997). de Haart et al., 1991a, determined that the optimum performance is expected for electrode layers with the longest TPB with a constant porosity.

Performance drop in SOFC's is mostly attributed to formation of interfacial reaction layers at the cathode and to anode degradation caused by the agglomeration of Ni particles and the resulting compaction of the anode layer. Metal agglomeration at the anode leads to a diminishment of reaction sites, cutting off current paths, reducing gas permeability and

increasing contact resistance between the electrode and current collector (Itoh et al., 1997; Wilkenhoener et al., 1999). The degradation is catastrophic when the initial metal component or porosity content is close to the percolation threshold. The most important point in the processing of Ni-YSZ electrodes is to keep the Ni to Ni contacts. Although an excessive Ni loading provides a higher electrode conductivity, it does not always guarantee high anodic activities because the TPB length is not directly proportional to the Ni content. Also, considering the fact that Ni coalescing is more probable and the thermal expansion mismatch between the Ni and YSZ components becomes serious in Ni-rich cermets, higher Ni loading may actually have negative effects on electrode performance (Lee et al., 1997; Kawada and Yokokawa, 1997; Ioselevich et al., 1997).

4.4.1 Two-Dimensional Interface

A two dimensional interface refers to a flat electrolyte surface coated by an electronic conductor (or mostly electronic). Traditionally, cathodes have been deposited in this morphology and it may not be a coincidence that a majority of the electrode impedance occurs on the cathode. The preferred methods used for the fabrication of an LSM layer on the YSZ substrate are plasma spraying and sputtering. Good contact conditions and a thin homogeneous layer are achieved, because they are gas phase processing methods. However, they are very expensive, on account of the specialized equipment needed to produce a thin film and, in the case of plasma spraying, can lead to thermal shock of the substrate. Several solid phase methods are used, including conventional ceramic processing, drip pyrolysis, coprecipitation and sol-gel. These methods are more affordable, but, because they are solid phase methods, good contact conditions are more difficult to achieve (Nagata et al., 1994).

It is common to use self-supporting cathodes with the electrolyte deposited on it. The electrolyte penetrates the pore structure of the cathode and essentially increases the length of the TPB, thereby increasing the cathode activity. If the penetrating YSZ it is not connected to the electrolyte bulk, however, then it acts as a barrier to oxygen diffusion (Suzuki et al., 1994).

4.4.2 YSZ/Metal Cermet Mixtures

Anode overpotentials are normally so much lower than those at the cathode, that they are inconsequential. Typically, in zirconia SOFCs, a Ni/YSZ cermet is commonly used with YSZ electrolytes to obtain improved adhesion and thermal expansion properties of the electrode at high operating temperatures as discussed in Section 4.3.2 (Virkar et al., 2000).

Cathodes continue to employ pure LSM even though it is recognized that a porous mixture of nickel and 8 YSZ is a much better anode for SOFC's than simply painted nickel powder (Tanner et al., 1997). Recent investigations have focussed on the morphology of the anode in hopes of using the knowledge to improve the performance of the cathode. Kenjo and Nishiya, 1992, demonstrated that cathode performance could be enhanced by mixing YSZ with LSM. Deleterious interface reaction products were the primary concern for this electrode morphology, but were prevented with an A-site deficiency.

Porous mixtures of electrocatalyst and electrolyte materials should increase the length of the triple phase boundary line by extending the active zone further into the cermet layer by supplying oxygen ions far from the electrolyte and lead to enhanced performance (Tanner et al., 1997). A uninterrupted YSZ phase contributes to a continuity of the ionic path, while the metallic nickel provides the anode with as high an electronic conductivity as possible. Greater than 30 vol% of interconnected porosity allows the transport of reactant and byproduct gases (Marinsek and Macek, 1997). This electrical behaviour can be styled as a random percolation model envisaging the cermet as a mixture of black and white sites on a regular lattice, representing the solid electrolyte and metal particles, respectively, as seen in Figure 4.9 (Ioselevich et al., 1997).

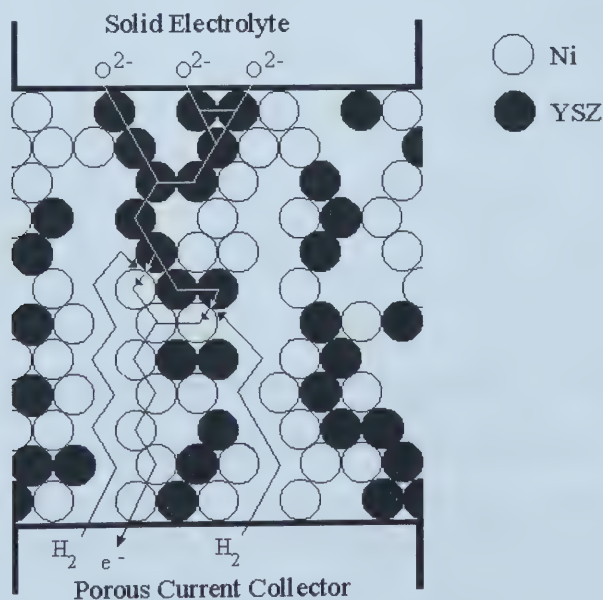


Figure 4.9 - Schematic diagram of the reaction zone of an SOFC cermet anode (Ioselevich et al., 1997).

An effect of the ionic conductivity of zirconia occurs in the electrocatalytic activity of the electrode reaction at the active TPB zone made with the zirconia. Using the same electrolyte and modifying the ionic conductivity of the zirconia in the cermet, it was determined that as the conductive effect of zirconia in the cermet decreased, the catalytic effect also decreases, because the catalytic effect must occur on the TPB. Based on this result, the TPB is expected to be increased with increasing ionic conductivity of the zirconia in the cermet. Impedance studies by Nakagawa et al., 1999, resulted in decreasing semicircle sizes with increasing yttria content in the zirconia powder of the cermet. In other words, with increasing ionic conductivity of the zirconia powder, the semicircle was decreased. The interfacial conductivity increased with increasing ionic conductivity of the zirconia in the cermet and the interfacial conductivity of the 8 YSZ cermet was almost 3.5 time larger than that of the pure zirconia cermet. The tendency for an increase in the exchange current density of the cermet appears concave in Figure 4.10. A concave trend may be explained by a combination of the conductive effect and the catalytic effect, although Nakagawa et al., 1999, had some reservations about the experimental accuracy.

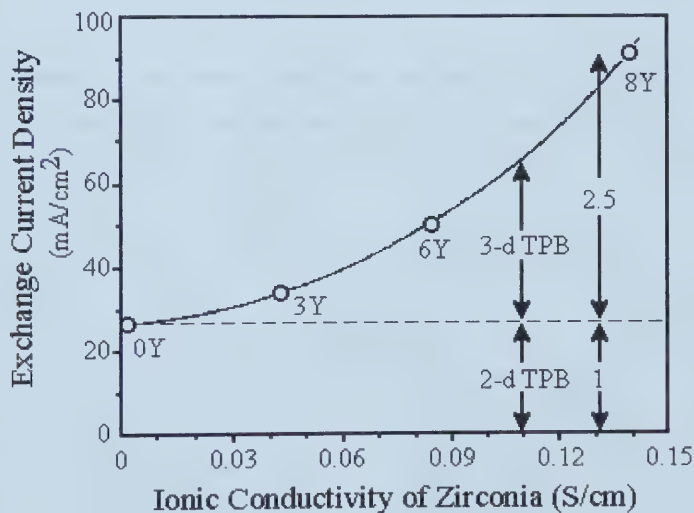


Figure 4.10 - Effect of YSZ conductivity in the cermet on the exchange current density at 1000°C (Nakagawa et al., 1999).

4.4.3 Mixed Conducting Electrodes

Mixed ionic-electronic conductors (MIEC) are, in principle, considered promising electrode candidates. The ionic conductivity can facilitate oxygen ion transport to any part of the surface of the electrode and the surface electronic conductivity facilitates electrocatalysis. This therefore results in a spacial extension of the electrochemically active zone from the electrode/electrolyte interface deep into the electrode (Wang et al., 1999). This should significantly decrease the electrode overpotential losses. The electrocatalytic activity does not necessarily have to be as good as metals, as the reactive area is much larger (van Hassel and Burggraaf, 1992). Figure 4.11 illustrates the difference between a pure electronic conductor and a mixed (ionic and electronic) conductor and the hypothetical reaction model at the anode (Colomer et al., 1996).

In a single phase MIEC electrode, the electrode kinetics could be suppressed if the electrode parameters are unfavourable, since the charge transfer occurs predominantly at high energy sites, such as grain boundaries and defects in the MIEC/gas phase interface. A microstructure that is too coarse or an ionic conductivity that is too low can reduce its effectiveness. The surface oxygen exchange rate and the electrode polarization are strongly dependent on the presence of electronic conductivity (Boukamp et al., 1993; Virkar et al., 2000).

The YSZ electrolyte surface exhibits little surface exchange activity on its own, so a mixed conducting oxide sandwiched between the Ni-YSZ anode and the electrolyte should expand the electrochemical reaction zone since reactions are free to occur over the entire free

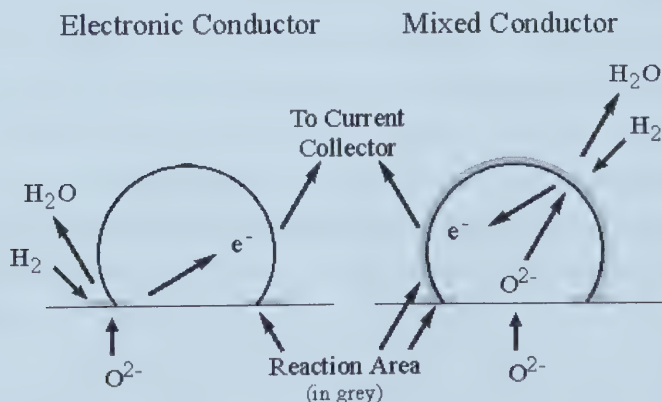


Figure 4.11 - Illustration of a purely electronic conducting electrode with a two-dimensional reaction interface (left) and a hypothetical mixed conducting electrode with a three-dimensional reaction zone (Colomer et al., 1996).

surface of the oxide. The Ni-YSZ anode serves both as a catalyst for CH₄ activation (to break down the C-H bond) and as a current collector to reduce contact resistance. Wang et al., 1999, modified the surface of the YSZ electrolyte by Fe-implantation to provide some mixed conductivity in a thin layer. The power outputs of MIEC interlayered anodes improved significantly in comparison with those of the MIEC oxides as anodes alone. Studies by Tsai and Barnett, 1998, demonstrated that inserting TZP and YDC (yttria doped calcia) layers at the electrode/electrolyte interface reduced the total size of the electrode impedance arcs. YDC interlayers (0.5 μm thick) on YSZ produced the lowest interfacial resistance of 0.13 Ω·cm² at 750°C and 0.29 Ω·cm² at 600°C (compared with 0.15 to 0.3 Ω·cm² at 750°C and 1 Ω·cm² below 650°C in Ni-YSZ anodes).

The deposition of tin-doped indium oxide films is of interest for use as air electrodes in zirconia based solid oxide fuel cells. At low Sn concentration (0.1 mole%), Sn enters indium oxide substitutionally and acts as an electron donor (n-type conductor) (Enloe and Wirtz, 1986). Fully dense indium oxide films are grown by EVD and transported via an interstitial or an interstitialcy mechanism (In₂O₃ changes to InO₂ and back to In₂O₃ on deposition) in the range of 1000 to 1300 K at atmospheric oxygen pressure (Wirtz and Takiar, 1981).

SrFeCo_{0.5}O_x, SrCo_{0.8}Fe_{0.2}O_{3-δ} and La_{0.6}Sr_{0.4}Fe_{0.8}Co_{0.2}O_{3-δ} are among those with both high oxygen ion and electron conductivities that have been used as membranes for separation of O₂ from air due to simultaneous conducting of electrons and oxygen ions. Results show that these oxides are not only active but also selective as anodes for SOFC's for producing syngas with the spontaneous generation of electrical energy. Previously, SFC_{0.5} has been used as a membrane in conjunction with an Rh catalyst for partial oxidation of methane. These mixed conducting oxides, when used as anodes, give modest electrochemical activities for both H₂ and CH₄ as fuels. In particular, the cell performance on CH₄ is comparable to that on H₂, showing the perspective for anodes of SOFC's running on dry methane; in fact they possess the high ionic conductivity, oxygen mobility and activity toward methane. However, the electrochemical performances of mixed oxide anodes are, in general, inferior to the Ni-YSZ anode (Wang et al., 1999).

4.4.4 Two-Layer Cermet Electrodes

An inherent disadvantage of solid state ionic devices is the poor interfacial contact between components, which inevitably leads to electrode polarization (Tang et al., 1996). Liquid-based electrochemical devices utilize pure electronic conductors for the electrodes; yet the performance of the electrodes is much better than for solid electrolytes. This performance is attributed to electrolyte “wetting” of the solid electrode particles. Hydrexpellants control the electrolyte wetting so that a continuous film is formed over the entire electrode surface, while maintaining open pores for gas diffusion. The continuity of the film guarantees an adequate ionic conduction and improves the performance by increasing the effective reaction area. In this way a very large three-dimensional TPB is formed, almost equal to the overall effective area per unit volume of the solid phase. (Kenjo and Nishiya, 1992; Costamagna et al., 1998).

Optical evidence for stable films of electrolyte on polished silver and nickel electrodes which were partially immersed in alkaline solutions have been reported. Pshenichnikov, 1963, suggested that the electrochemical reactions occur in the film of electrolyte covering the walls of the macropores of a two layer electrode represented by Figure 4.12. Since many micropores intersect the macropores, the electrolytic resistance of the solution film is shunted by the much smaller electrolytic resistance of the micropores which are completely filled with electrolyte (Breiter, 1969).

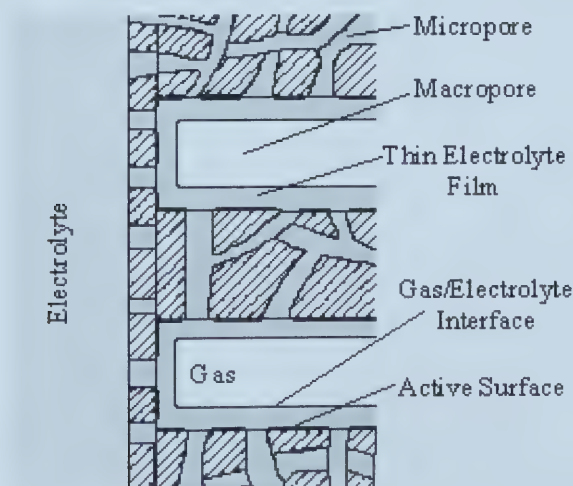


Figure 4.12 - Schematic representation of a two-layered electrode (Breiter et al., 1969).

Sasaki et al., 1992, formed cermet anodes by depositing YSZ using the EVD method after coating the electrolyte with a Ru powder slurry. Although it was not clear exactly what the morphology of the electrode was after deposition, it is assumed that a ceramic coating is attained over the surface of the metal electrode. The maximum power density of the cell was 1550 mW/cm^2 (0.516 V , 3.0 A/cm^2). The reasons for the high performance of the cell were attributed to a fine anode structure provided by the high T_m ruthenium, the thin electrolyte ($10 \text{ }\mu\text{m}$) and a very low cathode polarization.

In a patent by Isenberg and Zymboly, 1986, the EVD process was used to partially coat the metal electrode particles with the same materials as the electrolyte to approximately 1 to $5 \text{ }\mu\text{m}$ thickness. The metal electrode particles in contact with the ceramic coating are oxidized by pumping oxygen through the electrolyte with an inert anode environment (N_2) to fracture the ceramic coating. In the final step, the metal oxide layer is reduced to metal that is highly porous. When electrodes that do not have the ceramic coating are reduced in this manner, severe flaking of the electrodes was observed, indicating that the ceramic coating securely attaches the electrode to the electrolyte.

Lee et al., 1997, however, did not have favourable results. A NiO ($12.5 \text{ }\mu\text{m}$) and YSZ ($0.21 \text{ }\mu\text{m}$) layer were screen printed on a YSZ electrolyte. Sintering (1400°C for 1.5 h in air) results in the smaller YSZ particles being sintered around the larger NiO particles. The Ni channels were not well developed due to the intervening YSZ layer and the surface coated YSZ components were cracked severely due primarily to the large volume shrinkage associated with the transformation of NiO to metallic Ni.

Two different types of self supporting YSZ disks were used for the purposes of these experiments. The first, supplied by Westaim (4 mol% yttria), were prepared by the “Doctor Blade” technique. The slip was cut to a diameter of 25 mm and four layers were pressed at 10 MPa for 15 minutes. Following the burnout and sintering program outlined in Table 6.1, the final dimensions of the disks were 15 mm in diameter by 0.5 mm thick. The second type of disks used (Ceraflex 8Y, Marketech International Inc.) contained 8 mol% yttria and had the dimensions 25 mm in diameter by 0.2 mm thick.

The electrolyte disks were calcined at 500°C for 2 h and stored in a desiccator prior to electrode deposition. Platinum electrodes (5544, 5545 and 5542-J-1, Electroscience Laboratories, Inc) were screen printed on the surface of the disks ($d = 12$ mm). Several layers were applied and sintered (500°C for 15 min after each coat) to attain an appreciable thickness (> 10 μm), followed by sintering at 975°C for 15 min after the final coat was

applied. Platinum gauze was attached to the cathode on the final sinter, while a single wire was attached to the anode.

Table 5.1 - Burnout and sintering program used for 4 YSZ electrolytes by the Doctor Blade technique.

Ramp Rate (°C/hr)	Temperature (°C)	Dwell Time (hrs)
60	133	1
6	142	1
6	161	1
6	180	1
6	218	1
30	377	1
90	975	2
Step	0	END
600	1000	0.5
300	1475	2
300	800	0.1
Step	23	END

The zirconia disks were then cemented to the end of an alumina tube (McDanel) with a high temperature ceramic adhesive (Ceramabond 503, Aremco Products Inc.) as illustrated in Figure 5.1. The ceramic tube had a 15 mm hole in the end of it for the disk and two 1 mm

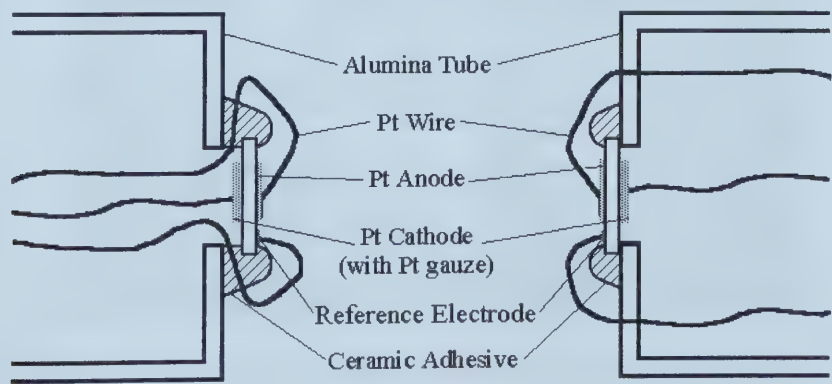


Figure 5.1 - Schematic diagram of two designs used for the PEVD reactor.

holes for the wires to pass. Vendor specifications stipulated drying at room temperature for 12 h, oven drying at 100°C for 2 h, then heat curing at 121°C for 2 h, followed by firing at 250°C for 2 h. The process was modified to allow a minimum of 12 h of oven drying at 80°C, followed by curing and firing as specified.

5.1 PEVD Deposition

The experimental setup is presented in Figure 5.2 and illustrated schematically in Figure 5.3. A Lindberg tube furnace surrounds a 75 mm diameter ceramic tube containing the PEVD reactor, which has a natural temperature profile throughout it. On either end of the tube furnace were fittings to maintain the vacuum and allow the alumina and the glass tubes to penetrate. The glove box maintains a water vapour free environment to prevent reactions with the chlorides which are highly reactive with water.

The temperature was raised to 750°C with 5% H₂/Ar flowing through the anode chamber at atmospheric pressure (to significantly reduce the oxygen partial pressure). The chambers were then evacuated simultaneously by a rotary pump (Welch 1400, Franklin Electric) to less than 5 Torr on the anode side, while maintaining a slightly higher cathode atmosphere pressure (10 to 25 Torr), as measured by a McCleod gauge, by drawing the vacuum through a bubbler with the air tube inserted to a slightly greater depth. Humidified air was then flowed to the cathode at 25 cm³/min, while in the anode chamber the hydrogen/argon mixture was turned off and pure argon turned on.

The substrate temperature was raised to 950°C, after which the ZrCl₄ and YCl₃ temperatures were raised to 170°C and 720-745°C, respectively, by moving the crucibles into

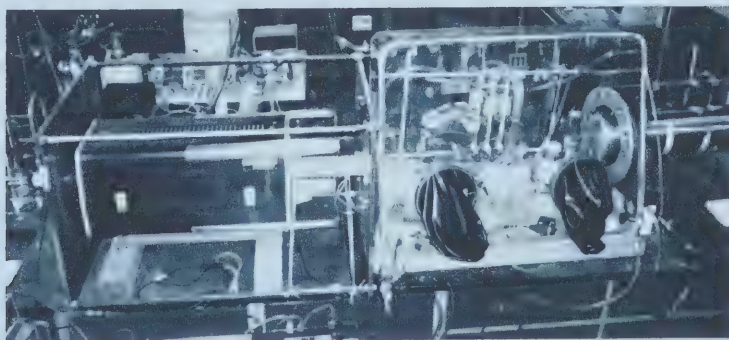


Figure 5.2 - Apparatus used for PEVD deposition. Anode reactants and gases enter through the glove box on the right and cathode gases enter on the left of the tube furnace.

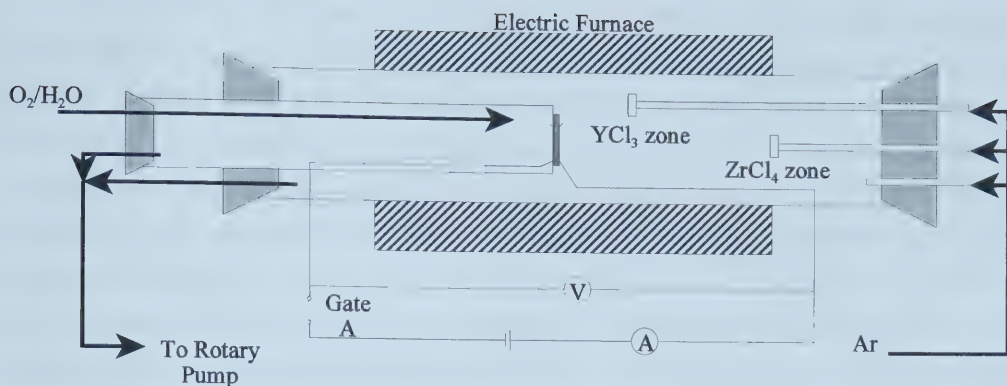


Figure 5.3 - Schematic diagram of PEVD reactor design.

their respective temperature zones. The argon gas flows through a Drierite/anhydrous column before passing into the system through the ZrCl_4 , YCl_3 and back-pressure tubes at 5, 5 and 15 cm^3/min , respectively. A d.c. potential of between 200 and 600 mV was applied to the cathode by a galvanostat/potentiostat (Model 371, Princeton Applied Research), while the current (Fluke 345) was measured in series and the voltage (Keithly 616 electrometer) was measured in parallel with the power source. Current was plotted with a dual channel analog recorder (Brinkman 2742-3).

5.2 Microstructure and Composition Studies

The microstructure was analysed using a scanning electron microscope (SEM) (Hitachi H-2700), and the composition with energy dispersive x-ray analysis (EDX) (Princeton Gamma Tech, Prism IG, intrinsic germanium detector with thin film window and PGT Imix analysis) and wavelength dispersive x-ray analysis (WDX) (JEOL JXA-8900R, 20 kV accelerating voltage, 15 nA beam current). For microstructure and EDX studies, plan and cross section views were analysed. Cross sections were viewed simply by fracturing the fuel cell in half. For WDX analysis, the specimens were prepared by mounting sections in epoxy (> 0.5 cm in thickness), grinding with 600 grit paper and polishing with 6, 3 and 0.25 micron diamond paste. All samples were carbon coated prior to examination by the above techniques.

5.3 Electrochemical Studies

For electrochemical studies, the procedure above was modified in order to minimize thermal shock of the cement and electrolytes. At 750°C, instead of passing 5% H₂/Ar and applying a vacuum, a variety of environments (including 5% H₂/Ar, 3% H₂O/H₂ and pure H₂) were applied to the anode at atmospheric pressure and air was flowed over the cathode at 25 cm³/min, also at atmospheric pressure. I-V characterization was executed with a voltmeter in parallel with an ammeter (Fluke 345) and a variable resistor (50 to 500,000 Ω). I-V data were recorded as the resistance was altered for temperatures of 750, 850 and 950°C. At 950°C and after completion of I-V characterization, EIS characterization was carried out with a three-electrode configuration in a variety of anode environments and a 25 cm³/min cathode air flow rate as used for I-V characterization. A lock-in amplifier (Gamry Instruments CMS 100 SR 810 DSP) was used for measurement and analysis.

Upon the conclusion of the initial electrochemical testing, dry 5% H₂-Ar was flowed through the system to again reduce the oxygen concentration and to significantly reduce water vapour before adding the metal chlorides to the system. Immediately following deposition, the vacuum was turned off and the pressure slowly increased by beginning the flow of anode and cathode gases. The above electrochemical tests were then carried out in reverse order: EIS characterization followed by I-V characterization at 950, 850 and 750°C.

The polarized electrochemical vapour deposition (PEVD) process was first studied as a possible solution to some of the problems experienced with Na^+ - β -alumina CO_2 sensors, including slow response, lack of sensitivity for low CO_2 concentrations and poor long term stability. It was thought that, by covering the electrode and electrolyte in an ultrathin film, most of these problems would be overcome. Most available processes, however, tend to produce films that are too thick or have insufficient adhesion to both the electrode and electrolyte. Conventional vapour deposition techniques have good film properties, but they are unable to deposit products at the base of high aspect ratio and irregularly shaped substrates (Tang and Etsell, 1996).

The PEVD process makes use of an ion conducting electrolyte, which can transport reactants through it under an electrochemical potential gradient that originates from an externally applied dc potential. In Na^+ - β -alumina sensors, the sodium ions migrate from the

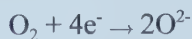
source electrode (anode) to the product electrode (cathode), obtain electrons from the Pt electrode and react with CO_2 and O_2 gas to form an Na_2CO_3 auxiliary phase (Tang and Etsell, 1997a; 1997b). As well as covering the entire surface of the electrode in an ultrathin film, the product phase is in intimate contact with both the electrolyte and electrode (Tang et al., 1998).

SOFC electrodes deposited with this technique result in two-layer cermet electrodes as described in Section 4.4.4. This results from the very low electronic transference number of the YSZ film being deposited (~ 0.01 for 8 YSZ). At the anode/electrolyte interface region, the deposited YSZ phase forms a dense layer encompassing the surface of the Pt electrode. This provides extra wetting for the metallic electrode/electrolyte contact. The deposited zirconia phase coats the entire metallic electrode surface from its contact with the solid electrolyte to the top of the cermet anode in a thin continuous layer (Tang et al., 1998).

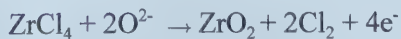
Coverage by the ceramic phase protects the metallic electrode from vapour loss, sintering and poisoning in the harsh SOFC operating environment in addition to improving the contact between the electrolyte and the electrode. Since the deposited phase is thin, the porosity of the anode does not decrease significantly, ensuring that all three phases for the SOFC anode reaction coexist in a three-dimensional electrochemically active anode. Unlike slurry coating of cermet anodes, formation of ionic conducting paths in PEVD cermet anodes should reduce the overpotential loss without sacrificing the electronic conducting path. Thus, the sheet resistance of the PEVD cermet anode should remain virtually the same as the pure metallic anode without degradation (Tang et al., 1998).

The PEVD process for YSZ cermet anode deposition proceeds as illustrated by the schematic diagram in Figure 6.1. The reactions which take place are the same as those that occur in EVD as follows:

Cathode Reaction:



Anode Reactions:



The difference is the supply source for electrons as illustrated in Figure 6.2. In EVD, the required electrons must be transported to the cathode through the film as it is being deposited. In PEVD, the electrons required are provided by a dc source and the electrons travel from the anode to the cathode through an external circuit (Tang et al., 1998).

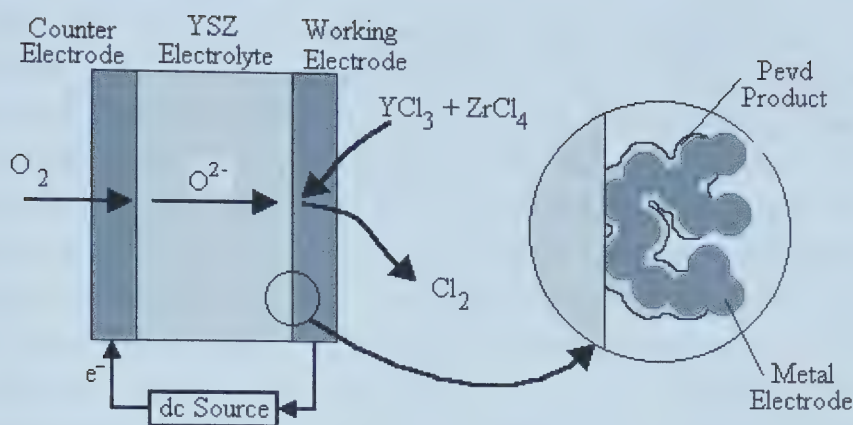


Figure 6.1 - Schematic diagram of the PEVD process.

There are two main advantages to using the PEVD process for thin film deposition, besides the resultant film properties. First, the process can be easily monitored and controlled by the electrical current and applied potential, respectively, as at least one of the reactants is transported through an ionic conductor in a solid electrochemical cell. The PEVD reaction rate is proportional to the rate of ionic transport, which can be measured by the electrical current in the external circuit (Tang and Etsell, 1997a; 1997b). Since a dc potential is applied, the thermodynamic driving force for PEVD reactions is not solely based on oxygen partial pressure differences. Tang et al., 1998, suggest that, since isolation of the anode and cathode environments may not be necessary, the design of the deposition apparatus can be simplified. Second, nucleation takes place primarily at the TPB and can proceed in one of two directions (along the metal electrode or along the YSZ electrolyte). By modifying the electrical properties of the depositing film, the morphology of the film can be controlled.

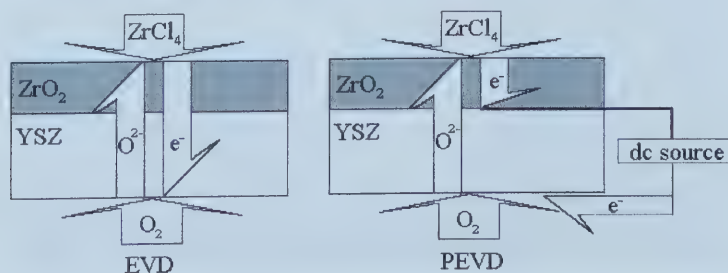


Figure 6.2 - Schematic representation of electron flow in the EVD and PEVD process.

6.1 Deposition Parameters

Three different platinum pastes, used for electrodes in this experiment (5544, 5545 and 5542-J-1, Electroscience Laboratories, Inc.), showed no significant differences in observed results. The 5544 paste used by Tang et al., 1998, however, had significant barium impurities (although the vendor would not specify which elements were added for improved sintering properties, etc.). The barium rich impurities tended to migrate to the electrolyte on the anode side when a negative potential was applied to the cathode, precipitating as an interlayer and weakening the bonding strength of the electrode to the electrolyte. No such impurities were detected in the 5545 and 5542-J-1 pastes, however, and similar sintering properties were observed in both. After sintering for 15 min, the platinum had a fine microstructure with an average particle size of 1 μm and a high porosity (~60 percent) as observed in Figure 6.3. However, after a week at a high fuel cell operating temperature (950°C) in air, the platinum tended to sinter to a coarser microstructure as seen in Figure 6.4.

In initial experiments, the wires passed through the cement between the electrolyte and the alumina tube to the anode and reference electrode. But, with so many cracks observed in the ceramic adhesive, 1 mm holes were drilled into the alumina tube as shown in Figure 5.1. The adhesive had more success with this design, as it could be much thinner and the higher thermal expansion coefficient of the platinum was no longer inducing failure. However, small cracks were observed to propagate from the holes in the alumina tubes after

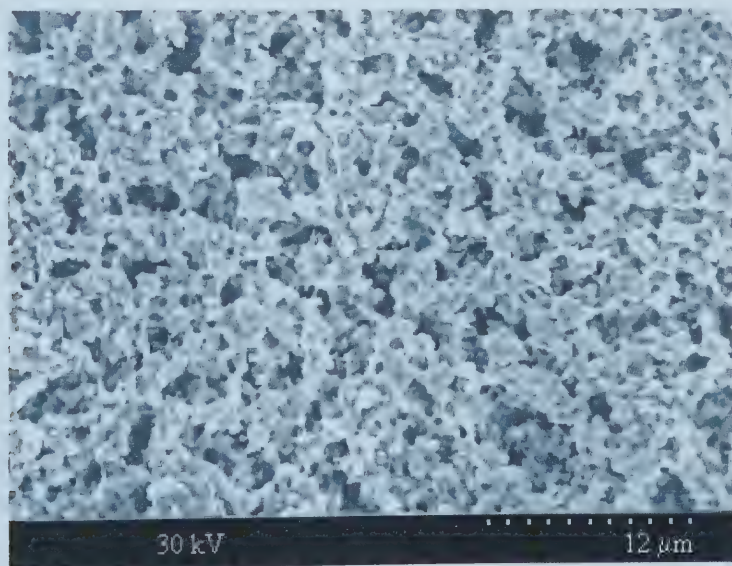


Figure 6.3 - SEM micrograph of a plan view of a platinum electrode after sintering at 975°C for 15 minutes.

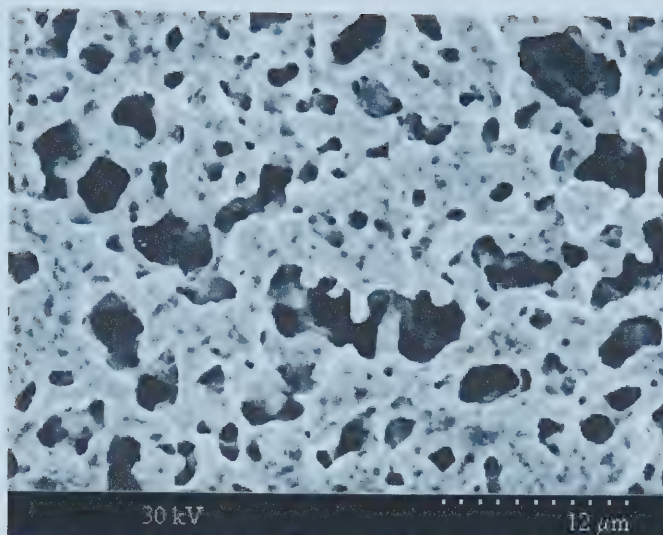


Figure 6.4 - SEM micrograph of a plan view of a platinum electrode after sintering in air for 7 d at 950°C.

only a few thermal cycles. In addition, a stress point was created in the platinum leads, causing them to fatigue and break easily (in the initial design, the wires were recemented each time exposing a different part of the wire to the stress concentration). This problem was severe with alloyed and small diameter wires. Thicker wire with no alloying elements had the best results with this design.

Several different cements and glasses were attempted in order to achieve a gas tight seal with enough strength to secure the fuel cell to the tube. Heraeus SG683K and IP9105HT sealing glasses, with high temperature resistance, were attempted with little success. Both products had poor strength and failed to secure the zirconia disks to the alumina tube, particularly at room temperature where they tended to be brittle. Several cements and ceramic adhesives (Durapot 801, OmegaCC, Fisher Alundum, Aremco 569, Aremco 516 and Aremco 503) were attempted, with the greatest success using Ceramabond 503 (Aremco Products) cement. It is alumina based, giving it good thermal expansion match with the tube and cell. Difficulties arose with the remainder the of products were caused mainly by poor thermal expansion matches, high sintering temperatures and high permeability to hydrogen.

Although Ceramabond 503 (Aremco Products) had the best results, it had to be treated with care. Vendor specifications were initially used, but the surface had a bubbly appearance after treatment, suggesting that it was not completely dry before raising the temperature to 120°C or that the 100°C drying temperature was too high. The process was

modified to allow all drying to take place at 80°C for 12 h, although it still required repairs after 4 hours to fix any cracks that had formed while drying. This modification of the procedure improved the success rate to better than 75%.

The cathode potential was varied between 200 and 600 mV and while it is not yet clear what, if any, morphology or property changes take place, it is clear that 200 to 300 mV provides the best deposition rates. As the voltage was increased to greater than 500 mV, deposition appeared to cease. No discernable deposit could be observed in the SEM after several days of deposition. The theoretical voltage for zirconium oxide deposition from zirconium chloride (standard temperature and pressure) was calculated using Equation 4.1 and $\Delta G_f = -205$ kJ/mol to be 0.531 V, which decreases as the temperature increases. Thus, as the voltage is increased to greater than 0.531 V, zirconia deposition is prevented. Thermodynamic data is not available for gaseous yttrium chloride. However, since zirconia is the major component and the two elements are so similar, it is expected that the open circuit voltage will not be significantly affected by the yttria component.

Once the conditions of very low water vapour partial pressure and low pressure are met, film growth ensues at an appreciable rate at 950°C. The presence of water vapour is detrimental to film growth and the argon gas must pass through a desiccant column to remove as much as possible. Vacuum pressure was not as critical to film growth, as long as the mean free path and diffusivity of the reactant are high enough. Film growth proceeds at appreciable rates in operating pressures of up to approximately 675 Pa (5 Torr).

6.2 Film Composition Analysis

Determining the yttria composition was exceedingly difficult, as the film was so thin and the yttria concentrations were relatively small. Most available processes require ample amounts of material, or for it to be dissolved into solution (as in atomic absorption spectroscopy, for example). The sample sizes that could be removed from the electrolyte surface were too small for most composition analysis tests. In addition, some methods, such as x-ray diffraction (XRD), as used by Tang et al., 1998, can only reveal the crystal structure present. In the case of YSZ, XRD indicates if the membrane was fully stabilized or not and the relative amounts of cubic and monoclinic phases, which can give an estimate of the yttria content up to 8 mol% yttria. Beyond 8 mol% yttria, however, the composition cannot be determined, as there is only one phase present.

EDX is a common and reliable technique for determining the chemical compositions of unknown solids. However, the energy difference between the major zirconium and yttrium

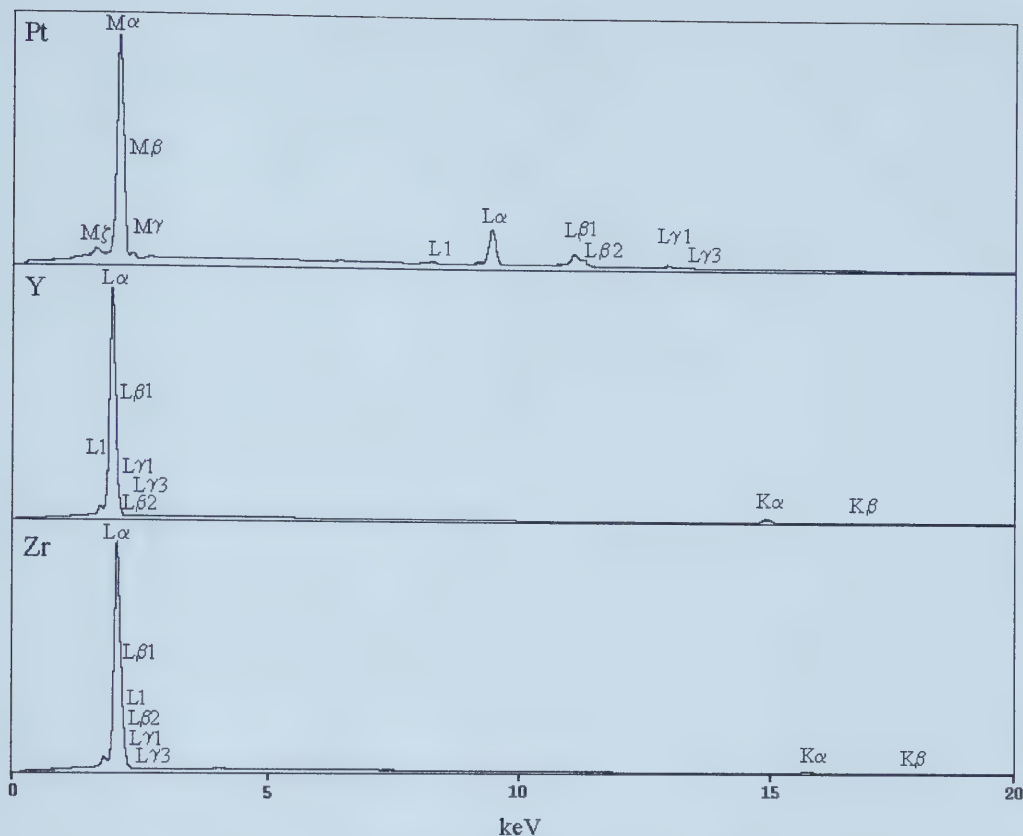


Figure 6.5 - Pt, Y and Zr standards at 20 kV accelerating voltage in EDX.

$L\alpha$ peaks in the spectrum is only 120 eV, making them unresolvable. Figure 6.5 illustrates the problem of overlapping peaks with an accelerating potential of 20 kV. Higher energy $K\alpha$ peaks (820 eV apart) need to be used to distinguish Zr and Y, necessitating the use of an accelerating potential of 30 kV to perform EDX analysis, as illustrated in Figure 6.6. The difficulty with this technique is that the YSZ film is very thin and any composition analysis results in greater than 60 mol% platinum. The result is that at 30 kV the output errors for yttrium concentration are as high as the reported yttrium content. Another technique is, therefore, needed to determine the yttria concentration with accuracy.

Wavelength dispersive x-ray analysis (WDX) is not as commonly used as EDX, since it has poor collection efficiency and cannot detect x-rays simultaneously over a wide energy range without mechanical motion. WDX does, however, have some advantages, which include better energy resolution (5-10 eV) to unravel peak overlaps, better peak to

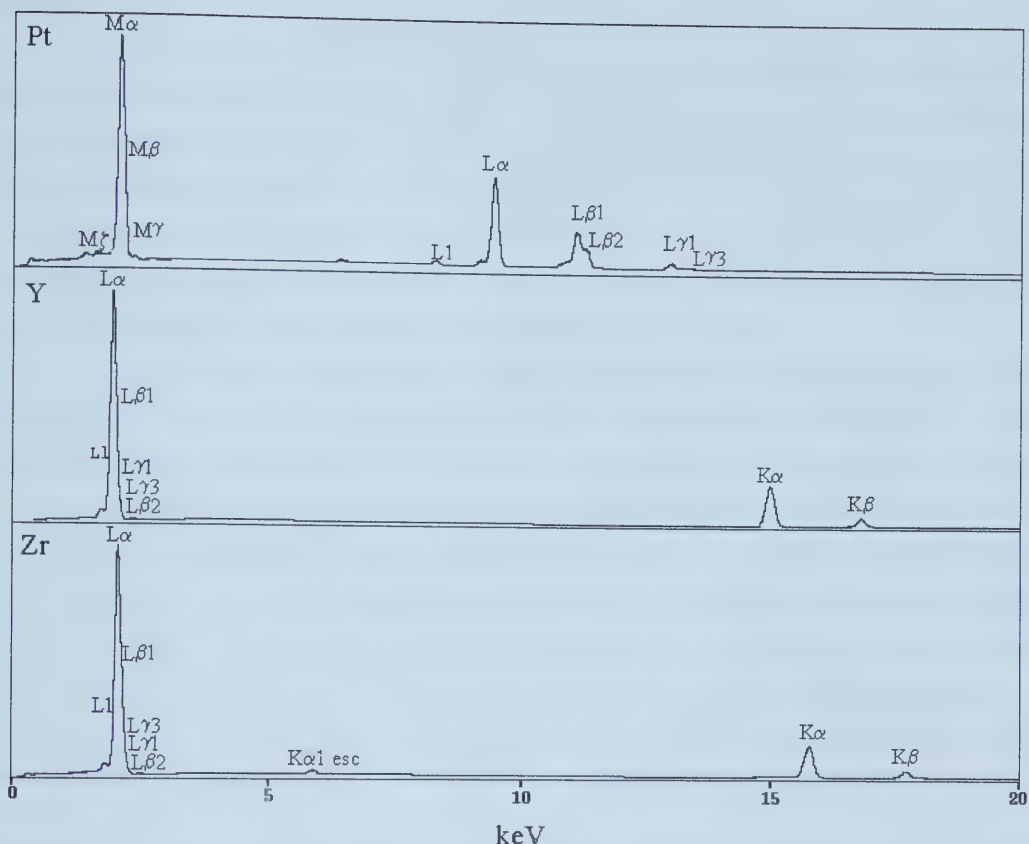


Figure 6.6 - Pt, Y and Zr standards at 30 kV accelerating voltage in EDX.

background capability to detect smaller concentrations of elements, better detection of light elements and no artifacts in the spectrum from the detection and signal processing (except for higher order lines from fundamental reflections) (Williams and Carter, 1996). Excessive peak interactions between Y, Zr and Pt and low yttria concentrations make it necessary to use this technique to obtain the yttria concentration in the film.

The requirements for a perfectly flat sample, however, was not without difficulties. After grinding, the surface was flat, but at least a 1 micron polish is required and, on polishing, the surface did not abrade evenly. The epoxy and electrode abrade easily in comparison with the electrolyte meaning the profile of the YSZ electrolyte becomes convex. Thus, minimal polishing was carried out to obtain a 0.33 micron finish and, even then, there was still a slight bulge in the electrolyte. Additionally, the electrode is porous and the film of interest coating the platinum is very thin (as will be discussed in Section 6.3), making it

difficult to get a good reading of the relative concentrations.

Table 6.1 presents the WDX peaks of the standards as summarized in Figure 6.7 It can be seen that there are no severe peak overlaps between yttria and platinum or zirconia. However, when the pure platinum standard was tested, there was 2.46 wt% zirconia and 0.39 wt% yttria detected, and 10.91 wt% platinum in the zircon standard due to peak overlaps between zirconia and platinum as shown in Table 6.1. Sample st-zircon* shows the WDX reading after correcting for the overlap. There was, however, still a 2.46 wt% error on the zirconia readings, as correcting for both elements was not possible.

Table 6.1 also summarizes the yttria concentrations determined using WDX (Appendix 1 shows all WDX tests carried out). As can be seen in Appendix 1, if the specimen is not perfectly flat or if there is a pore just below the surface, the total weight percent is typically lower than 90 % and the yttria content becomes exaggerated to two or three times the average yttria concentration of the remainder of the tests. This is especially true of sample 6.3-4, where the average concentration is 21 mol% until all of the tests outside a 90 % standard deviation are eliminated, resulting in a much more reasonable yttria concentration of only 14 mol%. Results from sample 6.3-5 has one listing in Appendix 1 because the films were too thin at this point ($< 0.5 \mu\text{m}$) and consistent concentrations were not achieved. The total weight percent in this case was typically about 65 wt%.

Table 6.1 - Measured chemical contents by WDX and the yttria content in the YSZ membranes (wt%). * represents the zircon standard after correcting for Pt/Zr peak overlap.

Specimen Number	Measured Chemical Content					Thin Film Yttria	
	ZrO ₂	Y ₂ O ₃	Pt	Other	Total	average	90 std.
st-YPO ₄	0.00	59.51	0.00	0.00	59.51	N/A	N/A
st-Pt	2.46	0.39	113.5	0.00	116.4	N/A	N/A
st-Zircon	65.50	0.09	10.91	32.77	109.2	N/A	N/A
st-Zircon*	65.93	0.06	0.00	32.74	98.73	N/A	N/A
6.3-1 (720°C)	59.39	2.24	5.56	26.34	93.53	3.64	3.14
6.3-2 (725°C)	48.98	3.14	13.76	27.31	93.19	6.04	5.96
6.3-3 (730°C)	55.65	6.35	0.73	27.40	90.13	10.23	10.23
6.3-4 (735°C)	51.05	13.49	0.43	20.40	85.37	21.06	13.98
6.3-5 (740°C)	19.16	36.93	0.36	8.81	65.29	65.84	-

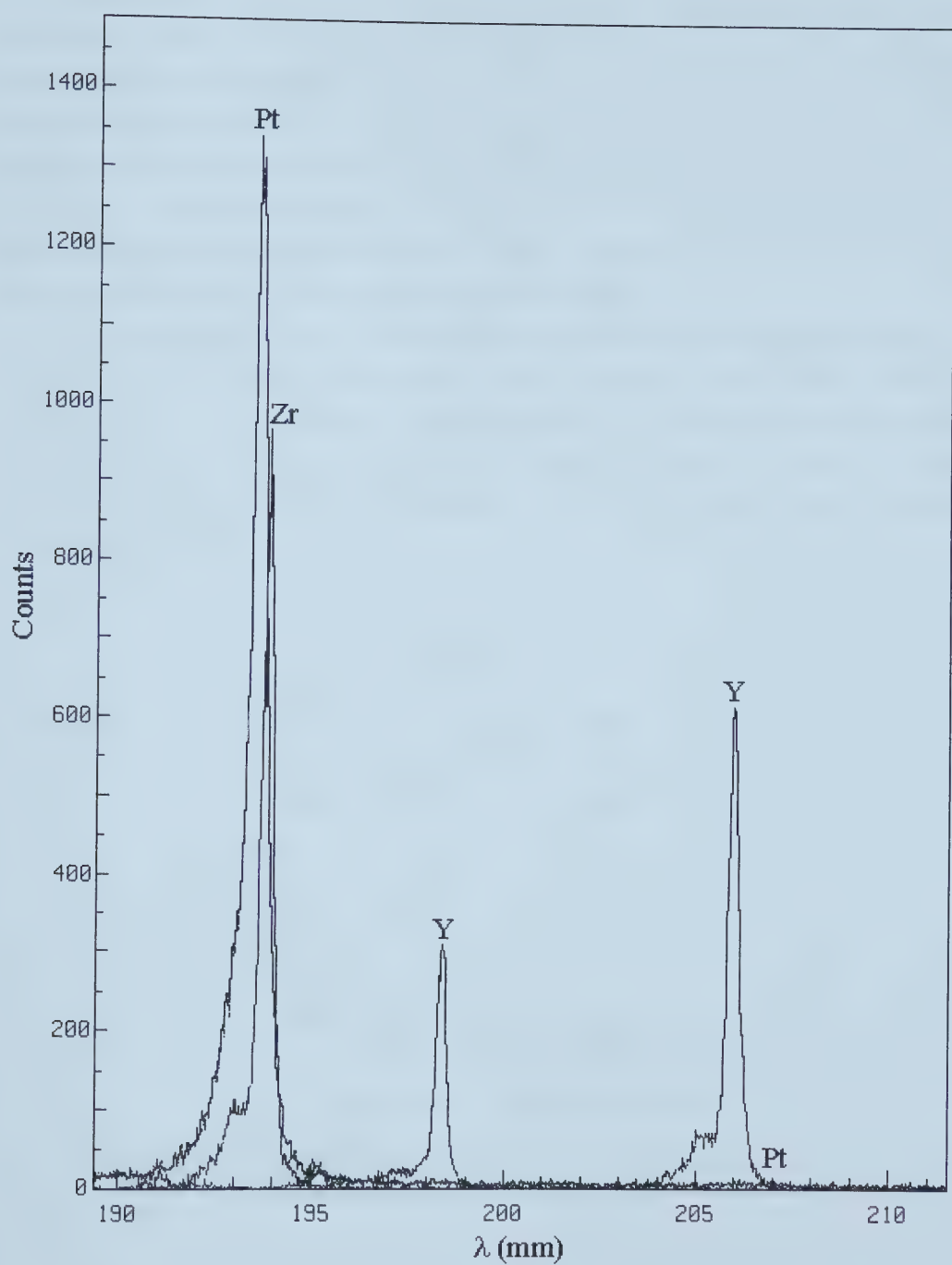


Figure 6.7 - Platinum, yttrium and zirconium standards at 20 kV accelerating voltage in WDX.

As the film on sample 6.3-1 was thick and uniform throughout the sample, reliable composition readings were easily obtained. Sample 6.3-3 had very good, smooth and consistent coverage, although there were some Al, Ba, Zn and Bi impurities and the source of these impurities was most likely from the ceramic adhesive. In sample 6.3-2, impurities tended to occur near the electrolyte, but improved as readings moved away from it. Samples 6.3-4 and 6.3-5 had very thin films and taking readings was very difficult. There was very little impurity present in these two samples. All of the samples had 25 to 30 wt% of Si, which can be attributed to the sample preparation (rough sanding).

The composition of the film varied with the yttrium chloride temperature as shown in Figure 6.8. Accordingly, a temperature of 727°C is required to obtain a fully stabilized 8YSZ film. This was much lower than that predicted by theoretical data (determined thermodynamically, Barin, 1989), which is also plotted in Figure 6.8. There are several possible reasons for this, such as some oxidation of the YCl_3 or a higher chamber pressure than the theoretical data.

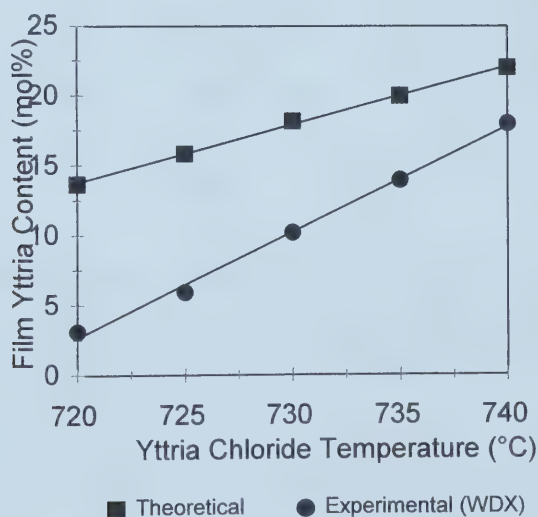


Figure 6.8 - Theoretical and experimental yttria content versus yttrium chloride temperatures while maintaining a constant $ZrCl_4$ temperature of 170°C.

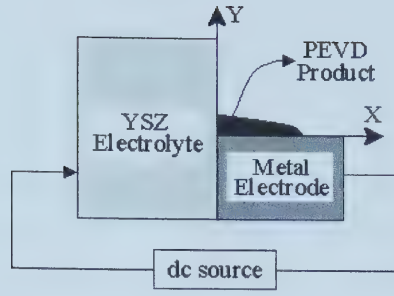


Figure 6.9 - Preferred growth direction of an ionic conducting layer over electronically (metal electrode) and ionically (YSZ electrolyte) conducting layers.

6.3 Film Morphology

Film growth in electrochemical systems is dependent not only on the diffusion of reactants and products and the reaction kinetics, but also on the movement of ions and electrons through the film. Film growth in electrochemical systems is often described by the Wagner scaling process. For film growth to advance in the X direction in Figure 6.9, i.e. along the surface of the electronically conducting material, the reaction limiting step must be ion transport through the product phase and can be expressed as follows (Ilschner-Gensch and Wagner, 1958; Tang and Etsell, 1997a; 1997b):

$$X = \frac{4}{\pi} \left(\frac{V_{product} \sigma_{ion} \Delta G t}{\mathfrak{I}^2} \right)^{1/2} \quad (6.1)$$

where $V_{product}$ is the molar volume of the product and t is the time of deposition. In the Y direction, i.e. along the surface of the ionically conducting material, the reaction limiting step is electron transport in the product phase and can be expressed as (Ilschner-Gensch and Wagner, 1958; Tang and Etsell, 1997a; 1997b):

$$Y = \left(\frac{V_{product} \sigma_e \Delta G t}{\mathfrak{I}^2} \right)^{1/2} \quad (6.2)$$

For a product phase with oxygen ions providing the ionic contribution, the ratio of the ion and electron conductivities can be used to determine its growth characteristics as follows (Ilschner-Gensch and Wagner, 1958; Tang and Etsell, 1997a; 1997b):

$$\frac{X}{Y} \approx \frac{1.265 \sqrt{\sigma_{O^{2-}}}}{\sqrt{\sigma_{e^-}}} \quad (6.3)$$

or

$$\frac{X}{Y} \approx \frac{1.265}{\sqrt{t_e}} \quad (6.4)$$

By equation 6.3, if the conduction of the product phase is primarily ionic, then the surface of the electronic conductor in the X direction will be coated in a thin layer of product phase. Conversely, if the conductivity of the product film is primarily electronic, film growth is favoured along the electrolyte, or the Y direction. There are, of course, other factors that must be considered, such as the location of electrochemically active reaction sites and adsorption sites, and the reactant (metal chlorides) surface diffusion rates. For example, if the active site for reaction is at the TPB between a mostly electron conducting film and the electron conducting metal electrode or if this is the site of reactant adsorption and the surface diffusion rates are too low, then film growth along the ionic conductor (Y direction) is not guaranteed.

Initially, the goal was to replicate the procedure used by Tang et al., 1998; thus the deposition conditions were, as much as possible, as published. After 12 h with chloride temperatures of 160 and 720°C for zirconium and yttrium, respectively, an oxide film coated the platinum as observed by secondary and backscattered electron images in Figure 6.10 A and B. It was reported that there was still tetragonal phase present and WDX results in Table 6.1 reveal that films deposited under these conditions contain 3 wt% yttria. It can be seen in both images that the YSZ film coats the entire exposed surface of the electrolyte. In Figure 6.10 B, the dark phase represents the YSZ and the platinum is represented by the white phase. It is difficult to determine the exact thickness of the film but, from these micrographs, it appears that the film is approximately 2 µm thick. There is also evidence in Figure 6.10 A that there is some film deposition over the surface of the electrolyte, although it is difficult to determine how complete this coating is. If the electrolyte is completely covered, it opens the technique to use for the fabrication of composite electrolyte.

There was a time dependence of film growth observed for these films. After 12 h (0.300 V), the film was not detectable throughout the entire platinum surface. It was concentrated around the platinum lead. However, after 24 h, the entire surface of the platinum anode was coated as illustrated in Figure 6.11 A to an estimated thickness of 1 to 2 µm. After three days, full density is achieved through most of the sample as indicated by Figure 6.11 B. The fact that the YSZ film is relatively thick, while not completely covering the entire surface of the platinum electrode, suggests that the film has a high electron conductivity and explains why, in Figure 6.11 B, the coating appears fully dense. Very few

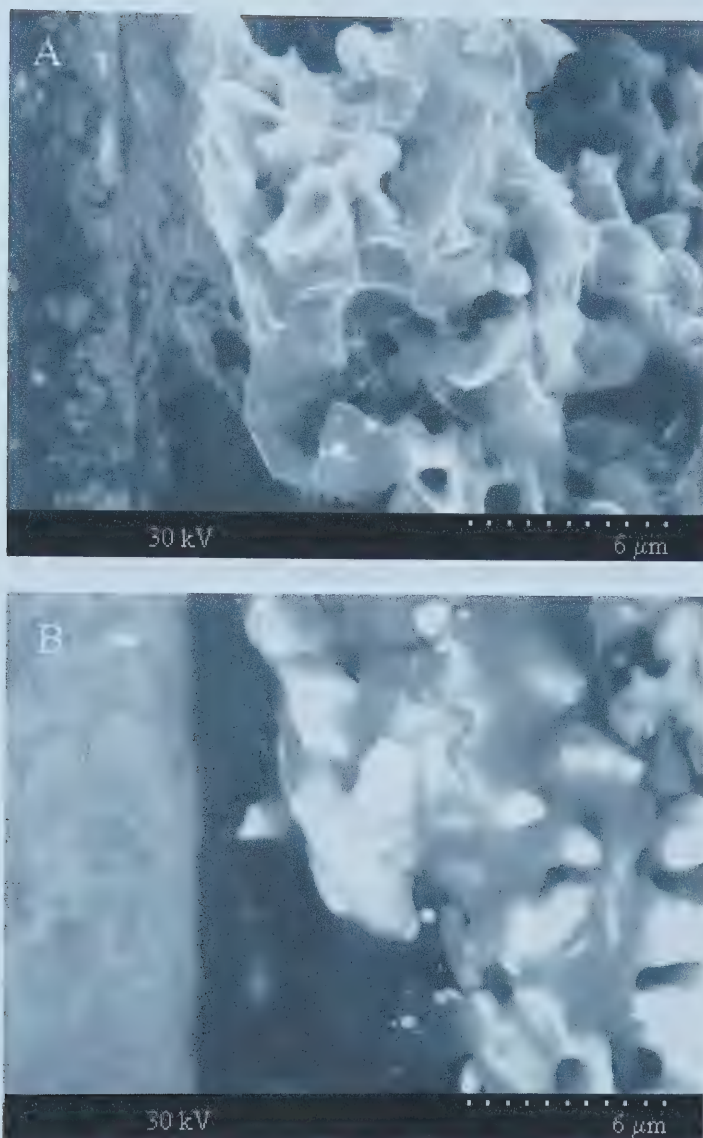


Figure 6.10 - PEVD membrane over porous platinum in both (A) secondary and (B) backscattered electron images. The dark phase is the PEVD membrane and the white phase is the platinum.

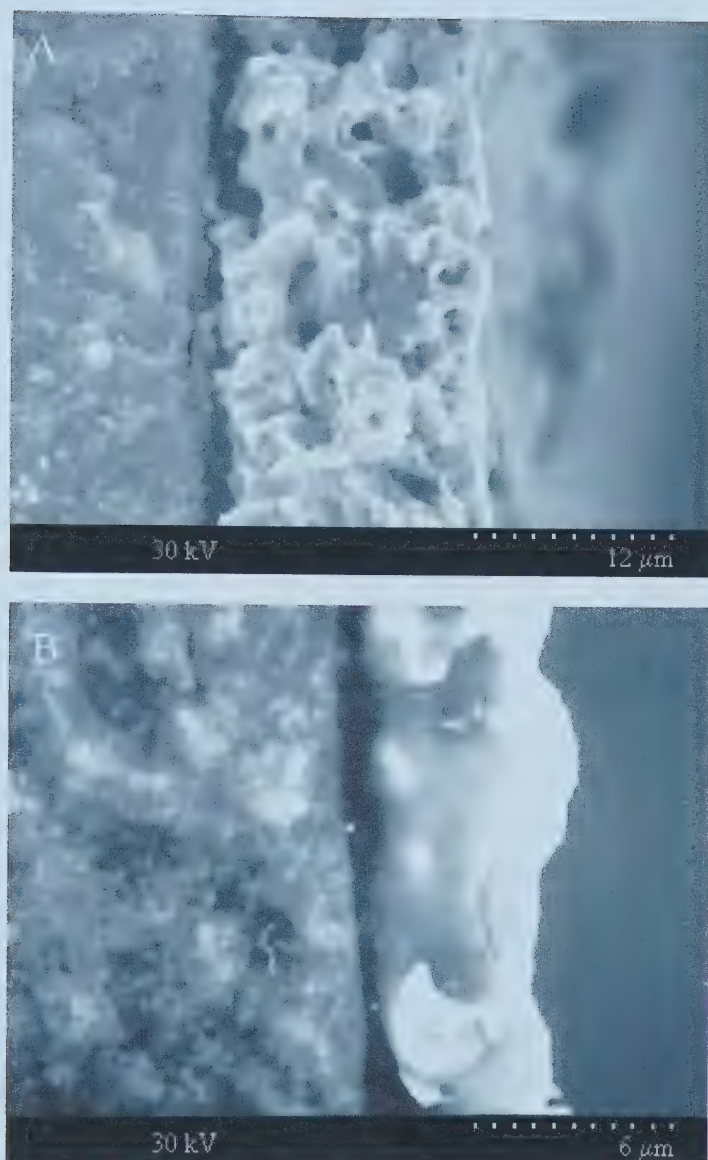


Figure 6.11 - Secondary electron images of membranes deposited over (A) 24 h and (B) 72 H containing 3 mol% yttria.

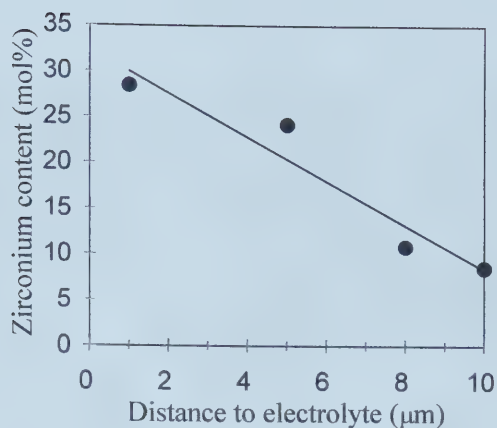


Figure 6.12 - Zirconium content over the film thickness.

pores were left closed off on the surface of the electrode and those that were tended to be quite large.

EDX was performed on the film at distances of 1, 5, 8 and 10 μm . Although the yttria content measured was smaller than the error values, the zirconia content (as compared with the platinum) gives an idea of how thick the film is. At 1 μm distance, it is expected that there would be some error caused by the proximity to the electrolyte. However, at 5 μm , there should not be any further interference. The results are illustrated in Figure 6.12. Readings were taken on areas that appeared flat enough for EDX tests to be reliable. The platinum just below the surface of the film makes up the rest of the composition. Yttria concentrations are 3 mol% throughout. This test is accurate on the assumption that the thicker the membrane is, the greater the zirconia content will be.

Films with compositions greater than 12 mol% behaved very differently during deposition. Coverage is very quick, with full coverage after only 12 h, and the film is very thin, but film growth in the thickness direction after complete coverage was extremely slow. After 168 h, it was not obvious whether there was any increase in the thickness beyond that after 24 h. The film thickness is estimated to be 0.5 to 1 μm . A comparison of high yttria films and low yttria films is given in Figure 6.13 A and B. As can be seen, the high yttria films in 6.13 B are very thin (possibly less than 500 nm) and the porosity is still quite high.

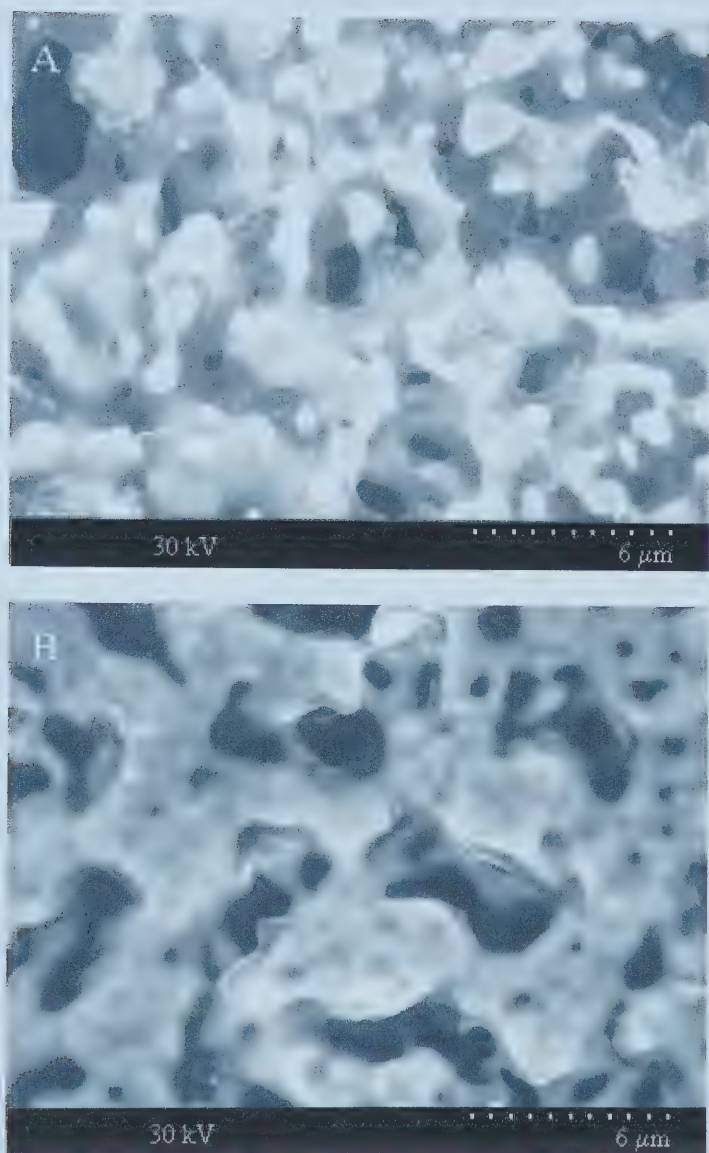


Figure 6.13 - Morphology of zirconia membranes containing (A) 3 mol% yttria and (B) 12 mol% yttria.

6.4 Current Characteristics During Deposition

As discussed at the beginning of this chapter, one of the main advantages of the PEVD process is that it can easily be monitored and controlled by the electrical current and applied potential. The amount of YSZ that is to be deposited can be determined by calculating the coulombs of electricity required to deposit the film and then monitoring the current and length of time that current flows through the cell. In addition, observations of the current characteristics over time can reveal the state of the deposit.

The current characteristics have been observed to vary with the electrical properties of the film. For fully stabilized zirconia films (> 8 mol% yttria), the current constantly increases over time (~ 15 to 16 mA) until the surface of the platinum is completely covered. At this point, the deposition current drops 3 - 5 mA from to approximately 12 mA. For partially stabilized films with a relatively high electronic conductivity (less than 6 mol% yttria), there was no observable current drop at any single point. The current, however, did decrease 2 to 3 mA slowly over a long period of time from approximately 15 mA to 13 mA.

6.5 Electrochemical Characterization

6.5.1 Current-Voltage Characteristics

The two-layer electrode morphology achieved with the PEVD technique should have a number of benefits to fuel cell longevity including protection from sintering and vaporization of low melting temperature materials resistance of low melting temperature materials and improved performance due to increased electrode wetting and TPB area as discussed in Section 4.4.4. This increase of the surface active area should result in improved power and current densities. Thus, an uncomplicated method for evaluating this electrode morphology is to compare the current-voltage characteristics before and after YSZ deposition over the surface of the Pt electrode.

All electrochemical testing (I-V and impedance) was carried out on electrodes containing fully stabilized zirconia (~ 8 - 10 mol% yttria) PEVD membranes over porous platinum for no other reason than a starting point was necessary. The anode environment was varied between 5% H_2/Ar and 97% $\text{H}_2/\text{H}_2\text{O}$. At high hydrogen concentrations, the cell tended to break down (low voltage and current). Severe polarization or hydrogen leakage (which is more likely since the voltage decreases, but brings into question the permeability of the ceramic adhesive to hydrogen) are thought to be the cause of this breakdown. After discontinuing hydrogen flow, the cell slowly recovered and the open circuit voltage would again exceed 0.9 V. A low H_2 mixture (5% H_2/Ar) was used for the I-V curves presented

here.

The maximum power density outputs for the as-deposited platinum electrodes was 2.5 and 12 mW/cm² for 4 YSZ and 8 YSZ electrolytes, respectively, with electrode areas of 1.13 cm². This is much lower than published results, which includes the following examples: 1500 mW/cm² at 1000°C by Suzuki et al., 1994; 1550 mW/cm² at 1000°C by Sasaki et al., 1992; and 1900 mW/cm² at 800°C by de Souza et al., 1997, and Virkar et al., 2000. Comparison of the present experimental values to the literature is not tenable, however, as the materials used (Ni) have superior catalytic ability in a fuel environment as discussed in Section 4.3.2 and a better morphology (slurry coated Ru, for example, used by Sasaki et al., 1992) affords a finer microstructure than screen printed Pt paste. This is not a problem, however, as a comparison of the current densities before and after PEVD deposition will reveal any benefits or detriments to the initial electrode morphology.

Figures 6.14 and 6.15 chart the I-V characteristics of the 4 YSZ electrolyte fuel cells before and after PEVD deposition at 750, 850 and 950°C. The most notable change is a significant decrease (by 5 or 10 times) in the power density after deposition. Similar observations were made using 8 YSZ electrolytes as illustrated in Figures 6.16 and 6.17. The result was much more dramatic, however, as the pre-deposit performance was much better. The post-deposition performance of both fuel cells were very similar, with the 4 YSZ electrolyte having double the power density of the 8 YSZ sample. This slightly improved performance is most likely related to the cathode performance. As discussed in Section 4.4.3, sandwiching a layer of mixed conductor between the electrode and electrolyte has the effect of improving electrode performance. After the anode side of the electrolyte is coated by the PEVD layer and since the 4 YSZ has a higher electronic transport number than 8 YSZ, the cathode performance would be improved without necessarily improving the PEVD coated anode.

A large increase in electrode polarization is observed in the I-V curves in Figure 6.14 although, without using the current interruption technique, a distinction between anode and cathode polarization is not possible. Figure 6.18 A and B, however, demonstrates that there is more sintering occurring in the reducing anode environment. This phenomenon of increased platinum sintering in a reducing environment was discussed in Section 4.3.2. Since the polarization increases with temperature, it should not be a result of concentration polarization, but further sintering as the temperature increases closes off more pores preventing gas diffusion. Following deposition, polarization appears to remain constant, suggesting that all electrode sintering has ceased. SEM evidence in Figure 6.13 B in

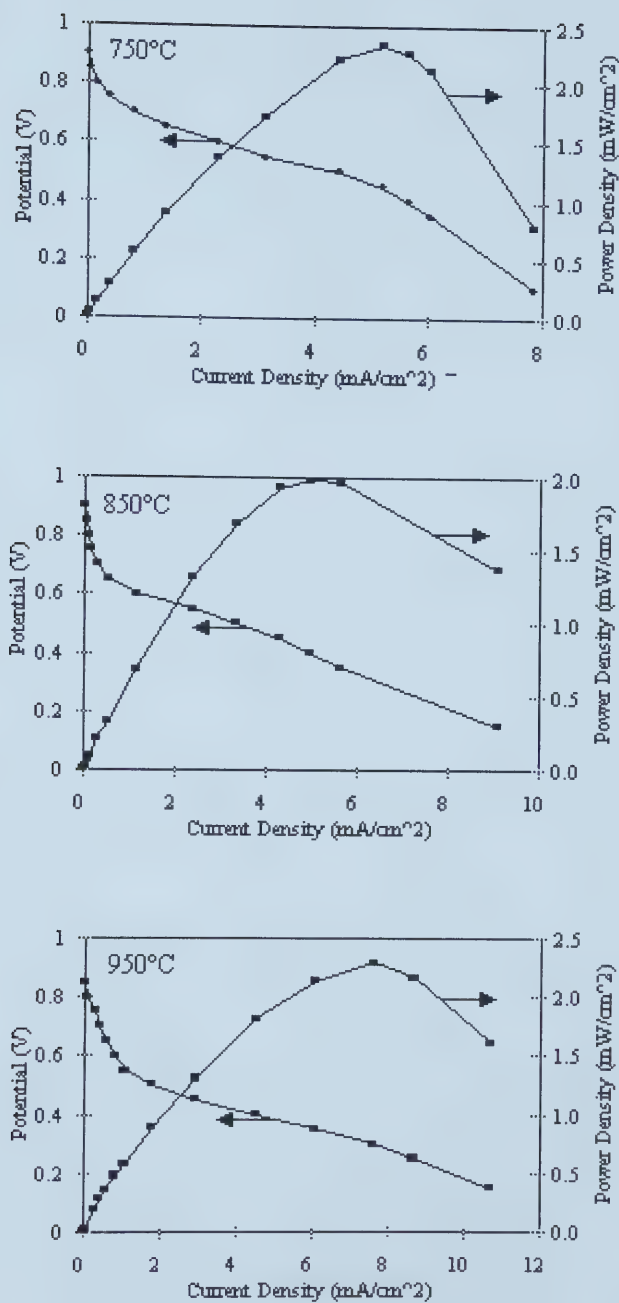


Figure 6.14 - I-V characterization of Pt electrodes before PEVD deposition of 8 YSZ using 4 YSZ electrolytes.

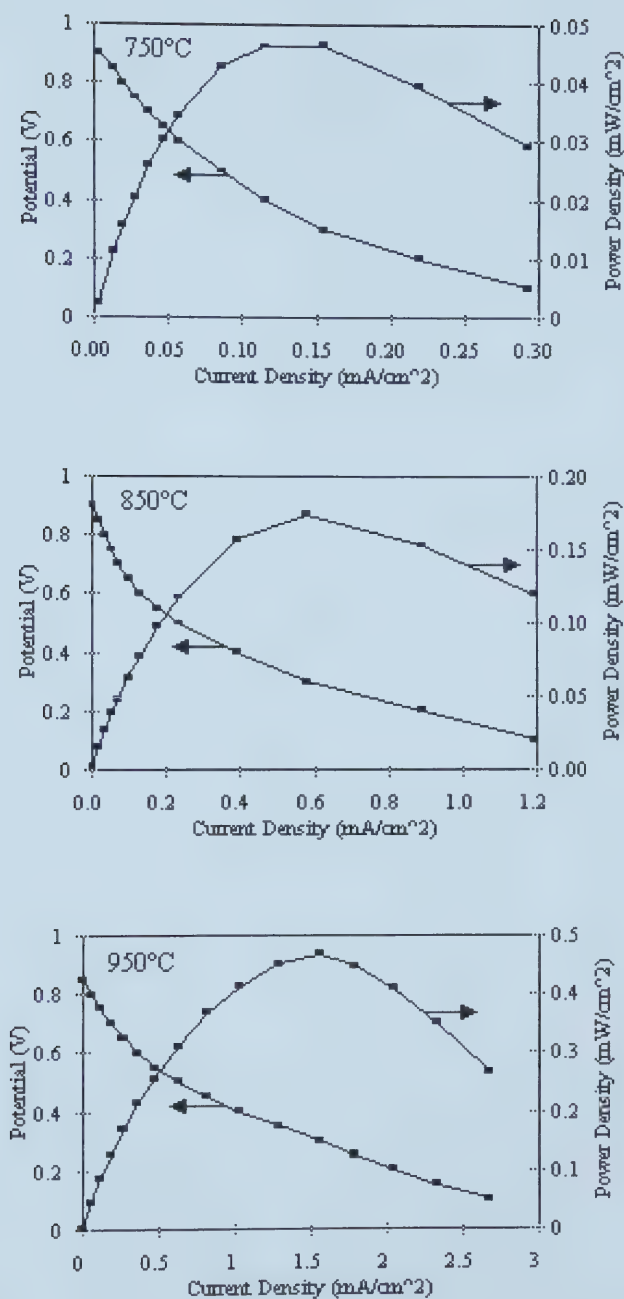


Figure 6.15 - I-V characterization of Pt electrodes after PEVD deposition of 8 YSZ using 4 YSZ electrolytes.

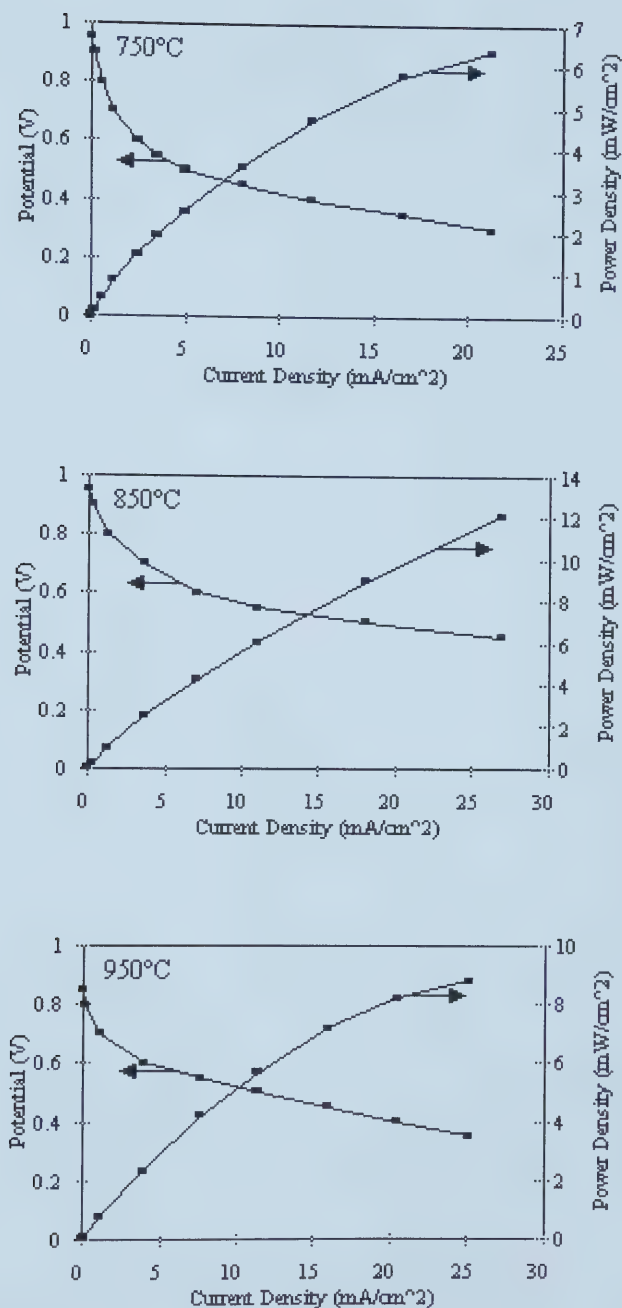


Figure 6.16 - I-V characterization of Pt electrodes before PEVD deposition of 8 YSZ using 8 YSZ electrolytes.

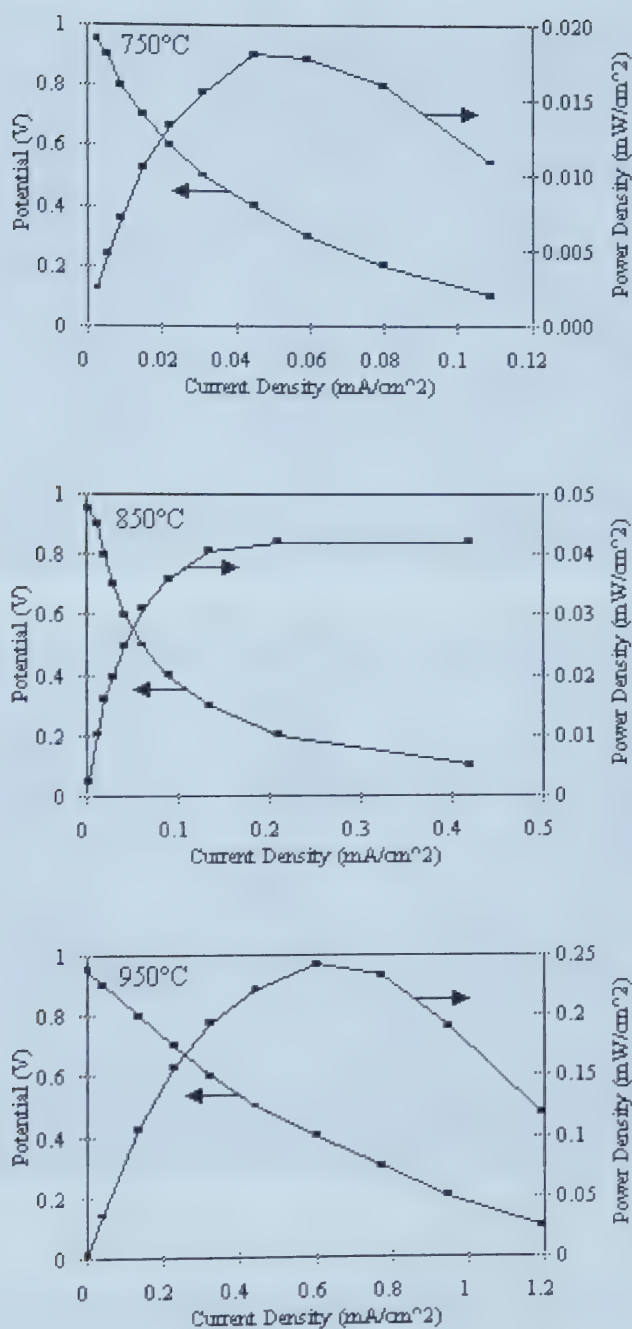


Figure 6.17 - I-V characterization of Pt electrodes after PEVD deposition of 8YSZ using 8YSZ electrolytes.

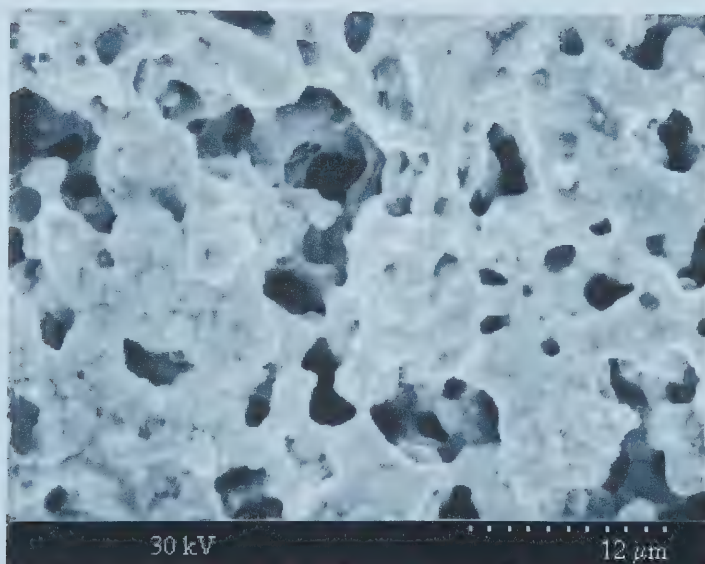
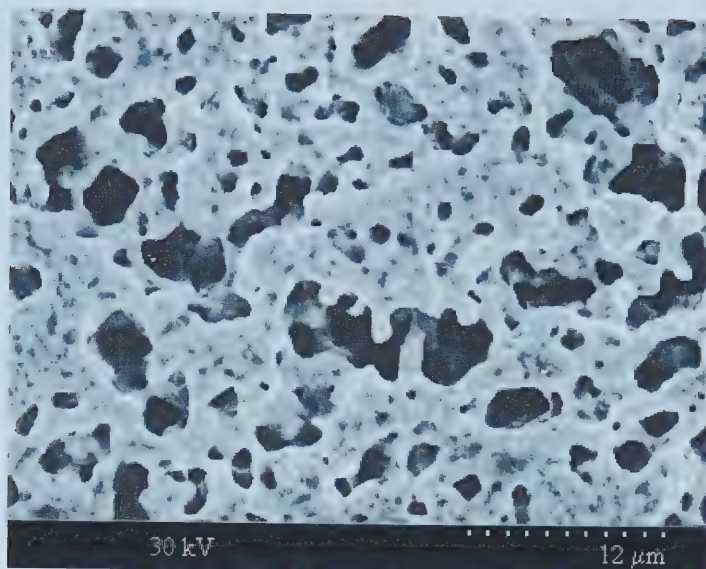


Figure 6.18 - Platinum electrodes sintered in (A) air and (B) hydrogen for 168 h.

comparison with Figure 6.4 supports this assertion, as the microstructure of the platinum electrodes are very similar (although the Figure 6.13 B has a transparent PEVD coating and the magnifications differ).

6.5.2 *Electrochemical Impedance Spectroscopy*

Typical EIS curves for before and after deposition are as observed in Figure 6.19 A and B, respectively. The equivalent circuits observed are very similar to those obtained by Matsui, 1992, and Velle et al., 1991, using a Warburg frequency dependent equivalent circuit as presented in Figure 4.6. Thus, the same equivalent circuit is used here.

It is noted that the electrode resistance from the EIS curves presented in Figure 6.19

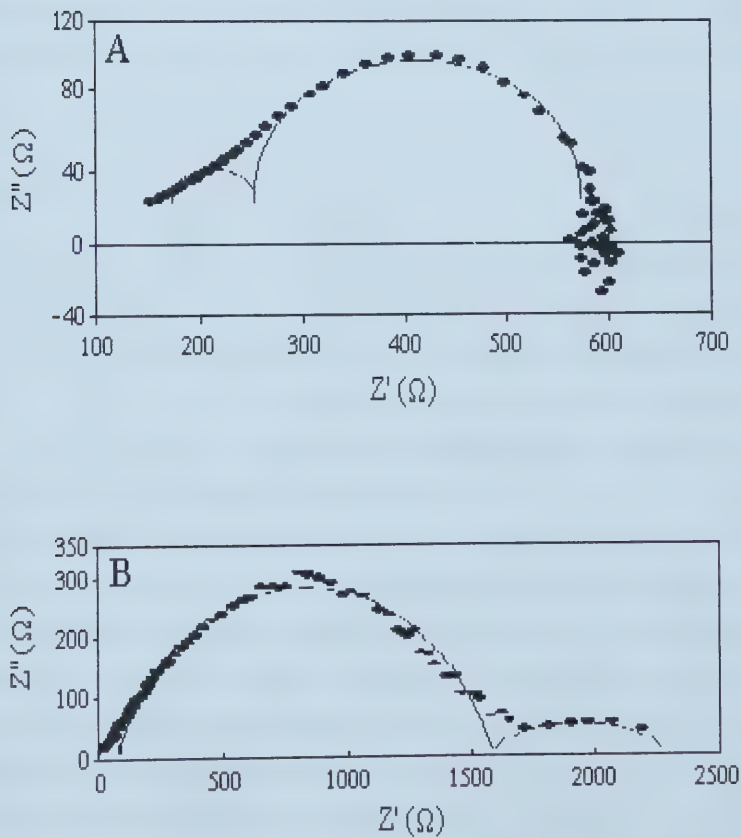


Figure 6.19 - Typical impedance plots at 950°C before (A) and after (B) PEVD deposition of 8 YSZ using 8 YSZ electrolytes.

are much larger than those presented in Figures 4.6 and 4.7. This is likely due to the reduced hydrogen partial pressure that was necessary to prevent leakage as discussed in Section 6.5.1. Mogensen and Lindegaard, 1993, also observed an increase in resistance as the hydrogen partial pressure was reduced. Again, as a comparison of the initial and final state is required, this should not be a problem.

The low frequency end of the pre-deposition impedance curve in Figure 6.19 A ends below the x-axis. This suggests that there is an electrode polarization of greater than ± 0.1 V and confirms the observation of a large pre-deposit polarization in Section 6.5.1. Following deposition, this polarization is no longer present and there is a second loop, most likely an interfacial reaction between the PEVD film and the platinum in the electrode. It is also noted that the resistance defined by the under the first (high frequency) loop (intercept on real axis) in Figure 6.19 B is much larger than that observed in Figure 6.19 A. These curves are in agreement with the performance observed in Section 6.5.1, as there is a large reduction in performance with the addition of 8-10 mol% YSZ to form a two-layer electrode morphology.

6.5.3 *Electrochemical Properties*

It is obvious from the results presented in 6.5.1 and 6.5.2 that an 8 to 10 mol% YSZ film is not the best composition for these two-layer electrodes. The electrocatalytic ability of the film may be insufficient and instead of enhancing the reaction area, it may actually be reducing it. As discussed in Section 4.3.2, adsorption, charge transfer and surface reactions are all involved in electrocatalysis. Problems most likely arise as a result of a combination of adsorption and charge transfer through the film, while surface reactions are not anticipated to be a serious hindrance to electrode performance.

Adsorption sites are most likely limited by the application of an 8 YSZ PEVD coating that is too smooth as a result of a self levelling effect that is too good and a grain size that is too large. The grain size of zirconia stabilized with varying quantities of yttria was discussed in detail in Section 3.3.1. In these TZP membranes, it was found by Bonanos et al., 1984, and Badwal, 1990, that the average grain size increases with increasing yttria content and the resistivity decreases with decreasing grain boundaries. Thus, electrolytes with few grain boundaries have better performance characteristics. In composite two-layer electrodes, however, it appears that fewer grain boundaries may actually be a hindrance to electrode performance. Observations of Figure 6.13 B reveal very few obvious surface flaws. In fact, the surface appears to be smooth which may actually prevent hydrogen adsorption on the

electrode surface.

Problems are also highly likely as a result of a low charge transfer rate resulting from the low electronic transport number inherent in fully stabilized zirconia. This would explain the deposition current observed in Section 6.4, the extremely thin (~ 0.5 to $1\ \mu\text{m}$) membranes attained and why the film so quickly covers the entire surface of the platinum, succeeded by extremely slow film coarsening as discussed in Section 6.3.

This does not, however, preclude the use of two-layer electrodes in electrochemical devices. In sensor situations where catalyst poisoning is severe and consistent performance is valued more than high performance, these films have the high chemical stability of YSZ, while maintaining a consistent conductivity (in moderate oxygen partial pressures). This does not relegate these PEVD electrodes to limited applications. There are many benefits to this process that should be taken advantage of, such as an ultrathin and highly adherent morphology with intimate contact between the film, electrode and electrolyte.

There are clues in the deposit structure and properties which show some potential. For example, in Section 6.4, it was shown that low yttria content films tended to continue to coarsen even after complete platinum coverage was achieved. This suggests that a smaller grain size, although more resistant to oxygen anion conductivity, has a greater number of surface flaws for reactant adsorption and a higher electronic transference number bolsters the charge transfer rate, improving what was deemed to be the two greatest hindrances to electrode performance.

In addition, other processes can be combined with the PEVD process in order to enhance the surface electrocatalytic properties, such as Fe- or Ti-implantation on the outer surface of the electrode, as they are unlikely to diffuse in to the electrolyte and alter its properties; coating the surface of the PEVD coating with an electronic conductor, such as Ni; or coating the metal electrode in a completely alternative ceramic materials, such as Sn doped In_2O_3 or one of the other MIEC materials discussed in Section 4.4.3. As for the suggestion that the PEVD film be coated with Ni, the Ni would sinter to small particulates on the surface of the YSZ. But this need not be a problem in two-layer electrodes (or in this case three-layer), as the Ni particles would provide adhesion sites and are not required to conduct electrons to the current collector.

6.6 Future Considerations

There are still many aspects that should be studied in order to determine the applicability of this process for two-layer electrodes in solid oxide fuel cells. Firstly, the grain

structure of PEVD films must be studied more closely. While it is clear that high yttria contents leads to thinner films, it is only speculated that the grain size is larger than those of low yttria content films from evidence provided from studies on slip cast YSZ samples. TEM studies could be carried out for the purposes of this study. Specimen preparation would not be as complicated as typical ceramic investigations, as the film could easily be deposited on platinum mesh and it appears in Figures 6.12 A and B as though parts of the film are already thin enough for this purpose. Once grain sizes are more confidently known, the effect of the average grain size on performance can be more closely determined.

The effects of various deposition parameters such as applied voltage, substrate temperature and oxygen partial pressure in the anode environment must also be studied more closely for their effect on the PEVD film thickness, grain size and deposition rates. This would fine tune the process such that the morphology of the film could be more closely controlled. Reducing the deposition temperature is utmost for the use of this process for deposition over silver electrodes. A deposition temperature of greater than 800°C is not feasible, as the melting temperature of silver is only 961°C. Increasing the oxygen partial pressure is of interest for manipulating the electrical properties of the YSZ membranes, allowing more control of its thickness.

The electrolyte surface coverage by the PEVD film should be determined. It appears in Figures 6.10 A and 6.11 A that there is some surface coverage, but it is uncertain if this electrolyte coverage is complete. If it is, then this opens this technique to form both a composite electrolyte and two-layer electrode for cerium oxide-based SOFC's. There is speculation that the electronic conduction of the ceria electrolyte in a reducing PEVD anode environment may hasten the coverage of the electrolyte with YSZ, but of course, none of this is certain without further study.

Early emphasis in fuel cell technology was placed on depositing thinner electrolytes that would significantly reduce ohmic resistance, which was the dominant factor in fuel cell polarization. With the advent of new improved techniques such as EVD, as well as strides in existing techniques, such as colloid deposition and CVD, electrolyte ohmic polarization is no longer the rate limiting factor. In the 1980's, much effort was expended to testing new electrode materials as activation polarization was now the limiting factor in SOFC performance. At present, research has shifted from electrode materials to electrode morphology, as it is thought by many that we have the right materials, but improved interfacial properties are needed. The most significant disadvantage of solid electrolytes as compared to liquid electrolytes is the poor interfacial contact which is achieved. There is no "wetting" of the contacted surface.

The following conclusions can be made from the present studies on the PEVD process

and the utilization of two-layer electrodes:

1. The PEVD process is capable of depositing thin oxygen anion conducting films with some electron conducting properties over the surface of electron conducting surfaces.
2. Coatings take place over the surface of electronic conductors so that reduction of the oxide does not cause shrinkage and sintering of the metal is not permitted, so that electrode degradation is minimized.
3. The thickness, morphology and rate of growth of the film depend largely on the ionic and electronic conduction properties of the film being deposited. The film growth characteristics proceed according to the Wagner scale growth theory. Ultrathin membranes ($\sim 0.5 \mu\text{m}$) result for high yttria contents (high ionic and low electronic conductivity) and thin films (~ 1 to $3 \mu\text{m}$) result from low yttria contents (moderate ionic and moderate electronic conductivities). Films with 3 mol% yttria grown over 24 h demonstrate a decreasing zirconia content, measured by EDX, in comparison to platinum, demonstrating that the film is thicker as you approach the electrolyte where deposition initiates.
4. Film growth proceeds at an appreciable rate with cathode applied potentials of between -200 to -300 mV. At potentials of approximately -500 mV and greater, film growth ceases, as the electromotive force for deposition for ZrCl_4 is -531 mV at standard temperature and pressure (which decreases as temperature increases).
5. Film compositions, measure by WDX, ranged from 3 mol% yttria for ZrCl_4 and YCl_3 sublimation temperatures of 170 and 720°C , respectively, to 14 mol% yttria for chloride temperatures of 170 and 735°C , respectively. Composition determinations of films with the higher yttria contents are exceedingly difficult as the film becomes too thin ($\sim 0.5 \mu\text{m}$) to get an accurate measurement.
6. The PEVD current during deposition varies with the electrical properties of the film. In low yttria concentration films, the current slowly decreases with time (approximately 15 mA to 13 mA). In fully stabilized films, the current slowly increases with time (approximately 15 mA to 16 mA) before suddenly decreasing by about 3 to 5 mA

when full coverage is achieved.

7. I-V and impedance characterization carried out on 8 to 10 mol% yttria PEVD films over platinum demonstrated a sharp decrease in electrode performance in the SOFC. This result emphatically points out that two-layer electrodes with 8 to 10 mol% YSZ films on their own are not an improvement over pure platinum two-dimensional TPB electrodes. This, however, does not preclude these types of electrodes from use in SOFC's, but more study is needed to determine first if low yttria films perform better or if further surface modification is necessary.

While the process is expensive, especially when considering the needs of large scale manufacturing and the possible added needs of surface treatment after the conclusion of PEVD, it holds promise of being highly stable over long periods of time (longer than the 50,000 h currently demanded) with much higher current and power densities. A high capital outlay would be worth it if there were significant increases to the lifetime and power density and a decrease in the operating temperature.

The potential benefits are numerous for a film morphology that has such intimate contact with the substrate, is ultrathin ($< 1 \mu\text{m}$) and whose morphology can be manipulated by altering its electrical properties. This process is not only of interest for SOFC anodes, but also in cathode and interconnect deposition, as well as in low temperature fuel cells for protecting the catalyst from poisoning by such impurities as H_2S . The close thickness control may also find applications in microelectronics, such as capacitors.

References

- Abel, J, A. A. Kornyshev and W. Lehnert, *Journal of the Electrochemical Society*, 144 (1997) 4253.
- Aizawa, M., C. Kobayashi, H. Yamane and T. Hirai, *Journal of the Ceramic Society of Japan, Int. Ed.*, 101 (1990) 283.
- Anderson, M. A., M. J. Gieselmann and Q. Xu, *Journal of Membrane Science*, 39 (1988) 243.
- Angrist, S. W., *Direct Energy Conversion*, Allyn and Bacon, Boston, 1982.
- Antonucci, V., E. Modica, G. Monforte, A. S. Arico, and P. L. Antonucci, *Journal of the European Ceramic Society*, 18 (1998) 113.
- Badwal, S. P. S., *Journal of Materials Science*, 19 (1984) 1767.
- Badwal, S. P. S., *Journal of Applied Physics, A: Solids and surfaces*, 50 (1990) 449.

- Badwal, S. P. S. and K. Foger, *Materials Forum*, 21 (1997) 187.
- Badwal, S. P. S. and M. V. Swain, *Journal of Materials Science Letters*, 4 (1985) 487.
- Baker, R., J. Guindet and M. Kleitz, *Journal of the Electrochemical Society*, 144 (1997) 2427.
- Barin, I., *Thermochemical Data of Pure Substances*, pt. 2, Verlag, Chemie, Weinheim, 1989.
- Barnett, S. A., *Energy*, 15 (1990) 1.
- Belot, J. A., R. J. McNeely, A. Wang, C. J. Reedy, T. J. Marks, G. P. A. Yap and A. L. Rheingold, *Journal of Materials Research*, 14 (1999) 12.
- Bockris, J. and S. Srinivasan, *Fuel Cells: Their Electrochemistry*, McGraw-Hill Book Company, New York, 1969.
- Bonanos, N., R. K. Slotwinski, B. C. H. Steele and E. P. Butler, *Journal of Materials Science Letters*, 3 (1984) 245.
- Boukamp, B. A., B. A. van Hassel, I. C. Vinke K. J. de Vries and A. J. Burggraaf, *Electrochimica Acta*, 38 (1993) 1817.
- Bourel, D. L. and W. Kaysser, *Journal of the American Ceramic Society*, 76 (1993) 705.
- Bradford, S. A., "Corrosion Control," Van Nostrand Reinhold, New York, (1993).
- Breiter, M. W., *Electrochemical Processes in Fuel Cells*, Springer Verlag, New York, 1969.
- Brinker, C. J., R. Sehgal, S. L. Hietala, R. Deshpande, D. M. Smith, D. Loy, and C. S. Ashley, *Journal of Membrane Science*, 94 (1994) 85.
- Brinkman, H. W., G. Z. Cao, J. Meijerink, K. J. DeVries and A. J. Burggraaf, *Journal de Physique IV*, 3 (1993) 59.
- Brook, R. J., *Journal of the European Ceramic Society*, 5 (1989) 75.
- Bruce, P. G., *Annual Progress Report on Chemistry, A: Inorganic Chemistry*, 87 (1990) 199.
- Budd, K. D., S. K. Dey and D. A. Payne, *British Ceramic Proceedings*, 36 (1985) 107.
- Budhani, R. C. and R. F. Bunshah, *Advanced Ceramic Processing and Technology*, 1 (1990) 369.

- Cannell, D. and P. Trigg, *Advanced Ceramic Processing and Technology*, 1 (1990) 95.
- Cao, C. B., J. T. Wang, W. J. Yu, D. K. Peng and G. Y. Meng, *Thin Solid Films*, 249 (1994) 163.
- Cao, G. Z., H. W. Brinkman, J. Meijerink, K. J. de Vries and A. J. Burggraaf, *Journal of the American Ceramic Society*, 76 (1993) 2201.
- Carolan, M. and J. Micheals, *Solid State Ionics*, 25 (1987) 207.
- Carolan, M. and J. Micheals, *Solid State Ionics*, 37 (1990a) 189.
- Carolan, M. and J. Micheals, *Solid State Ionics*, 37 (1990b) 197.
- Chaba, P. J. and P. E. Ngoepe, *Materials Research Society Symposium Proceedings*, 453 (1997) 549.
- Chiodelli, G. and M. Scagliotti, *Solid State Ionics*, 73 (1994) 265.
- Chour, K. W., J. Chen and R. Xu, *Thin Solid Films*, 304 (1997) 106.
- Chu, May-Ying, L. C. De Jonghe and M. N. Rahaman, *Acta Metallurgica*, 37 (1989) 1415.
- Claussen, C., C. Bagger, J. B. Bilde-Sorensen and A. Horsewell, *Solid State Ionics*, 70/71 (1994) 59.
- Colomer, M. T., E. Nieto and J. R. Jurado, *American Ceramic Society Bulletin*, 75 (1996) 85.
- Costamagna, P., P. Costa and V. Antonucci, *Electrochimica Acta*, 43 (1998) 375.
- Craciun, D. and V. Craciun, *Applied Surface Science*, 54 (1992) 75.
- de Haart, L. G. J., K. J. de Vries, A. P. M. Carvalho, J. R. Frade and F. M. B. Marques, *Materials Research Bulletin*, 26 (1991a) 507.
- de Haart, L. G. J., Y. S. Lin, K. J. de Vries and A. J. Burggraaf, *Solid State Ionics*, 47 (1991b) 331.
- de Souza, S., S. J. Visco and L. C. de Jonghe, *Journal of the Electrochemical Society*, 144 (1997a) L35.
- de Souza, S., S. J. Visco and L. C. de Jonghe, *Solid State Ionics*, 98 (1997b) 57.

- de Boer, B., M. Gonzalez, H. J. M. Bouwmeester and H. Verweij, *Solid State Ionics*, 127 (2000) 269.
- Dekker, J. P., V. E. J. van Dieten and J. Schoonman, *Solid State Ionics*, 51 (1992) 143.
- Drory, M. D. and A. G. Evans, *Journal of the American Ceramic Society*, 68 (1985) 342.
- Dubourdieu, C., S. B. Kang, Y. Q. Li, G. Kulesha and B. Gallois, *Thin Solid Films*, 339 (1999) 165.
- Duh, J. G. and J. J. Hwang, *Materials Chemistry and Physics*, 20 (1988) 409.
- Duh, J. G. and M. Y. Lee, *Journal of Materials Science*, 24 (1989) 4467.
- Dzjubenko, N., L. Martynenko, N. Zharkova, E. Gavrischuk and A. Gibin, *Materials Science and Engineering*, B18 (1993) 232.
- Eguchi, K., T. Kunisaki and H. Arai, *Journal of the American Ceramic Society*, 69 (1986) C282.
- Eguchi, K., T. Setoguchi and H. Arai, *Vacuum*, 41 (1991) 1061.
- Enloe, J. H. and G. P. Wirtz, *Journal of the Electrochemical Society*, 133 (1986) 1583.
- Etsell, T. H. and S. N. Flengas, *Chemical Reviews*, 70 (1970) 339.
- Evans, A. G. and C. H. Hsueh, *Journal of the American Ceramic Society*, 69 (1986) 444.
- Farrington, Gregory and Bruce Dunn, *Naval Research Reviews*, 37 [2], 1985, p. 27-32.
- Feduska, W. and A. O. Isenberg, *Journal of Power Sources*, 10 (1983) 89.
- Frenkel, J., *Zeitschrift fuer Physik*, 35 (1926) 652.
- Garcia, G., J. Casado, J. Llibre and A. Figueras, *Journal of Crystal Growth*, 156 (1995) 426.
- Goodenough, J. B., *Solid State Microbatteries*, Edited by J. R. Akridge and M. Balkanski, Plenum Press, New York (1990) 195.
- Göpel, W. and H. D. Wiemhöfer, *Berichte der Bunsen Gesellschaft fuer Physikalische Chemie*, 94 (1990) 981.
- Goto, K. S., K. Nagata and G. R. St. Pierre, *Elliot Symposium Proceedings* (1990) 463.

- Grubb, W. T. and L. W. Niedrach, "Fuel Cells," Direct Energy Conversion, Edited by G. W. Sutton, McGraw-Hill Book Company, Toronto (1966) 39.
- Hammouche, A., E. Siebert and A. Hammou, Materials Research Bulletin, 24 (1989) 367.
- Han, J. H. and Y. S. Lin, Solid State Ionics, 73 (1994) 255.
- Hartmanova, M., K. Gmucova, M. Jergel, I. Thurzo, R. Kundracik and M. Brunel, Thin Solid Films, 345 (1999) 330.
- Heavens, S. N., Advanced Ceramic Processing and Technology, 1 (1990) 255.
- Hirano, S. I., T. Yogo, K. I. Kikuta, K. I. Noda, M. Ichida and A. Nakamura, Journal of the American Ceramic Society, 78 (1995) 2956.
- Hseuh, C. C. and M. L. Mecartney, Journal of Materials Research, 6 (1991) 2208.
- Hsiao, Y. C. and R. Selman, Solid State Ionics, 98 (1997) 33.
- Hufschmidt, Heike, A. Weyl and D. Janke, Journal of the American Ceramic Society, 79 (1996) 756.
- Huggins, R., Electrochemistry in Industry - Proceedings of an International Symposium on Electrochemistry, 1980 (pub. 1982) 195.
- Ilischer-Gensch, C. and C. Wagner, Journal of the Electrochemical Society, 105 (1958) 198.
- Inaba, M., A. Mineshige, T. Maeda, S. Nakanishi, T. Takahashi, A. Tasaka, K. Kikuchi and Z. Ogumi, Solid State Ionics, 93 (1997) 187.
- Ioffe, A. I., D. S. Rutman and S. V. Karpachov, Electrochimica Acta, 23 (1978) 141.
- Ioselevich, A., A. A. Kornyshev and W. Lehnert, Journal of the Electrochemical Society, 144 (1997) 3010.
- Isaacs, H. S., L. J. Olmer, E. J. L. Schouler and C. Y. Yang, Solid State Ionics, 3/4 (1981) 503.
- Isenberg, A. O. and G. E. Zymboly, US Patent No. 4,582,766 (1986).
- Itoh, H., T. Yamamoto, M. Mori, T. Horita, N. Sakai, H. Yokokawa and M. Dokiya, Journal of the Electrochemical Society, 144 (1997) 641.

- Ivers-Tiffée, E., B. Jobst, I. Kraus, R. Schachtner and M. Schiessl, *Mat. Sci. Forum*, 79-82 (1991) 875.
- Iwahara, H. and T. Hibino, *Proceedings of the Symposium on Chemical Sensors*, 2 (1993) 464.
- Jang, J. H., J. H. Ryu and S. M. Oh, *Ionics*, 6 (2000) 86.
- Jeon, I. D., L. Gueroudji and N. M. Hwang, *The Korean Journal of Ceramics*, 5 (1999) 131.
- Joshi, A., S. Kulkarni, J. Nachlas, J. Diamond, N. Weber and A. V. Virkar, *Journal of Materials Science*, 25 (1990) 1237.
- Julbe, A., C. Guizard, A. Larbot, L. Cot and A. Giroir-Fendler, *Journal of Membrane Science*, 77 (1993) 137.
- Julien, C., *Materials Science and Engineering*, B6 (1990) 9.
- Kabanova, M. I., V. A. Dubok, S. A. Nochevkin, A. F. Chisty and P. Y. Pakshev, *Soviet Powder Metallurgy and Metal Ceramics*, 30 (1992) 776.
- Kawada, T., N. Sakai, H. Yokokawa, M. Dokiya and I. Anzai, *Solid State Ionics*, 50 (1992a) 189.
- Kawada, T., N. Sakai, H. Yokokawa, M. Dokiya and I. Anzai, *Journal of the Ceramic Society of Japan, Int. Ed.*, 100 (1992b) 838.
- Kawada, T. and H. Yokokawa, *Key Engineering Materials*, 125/126 (1997) 187.
- Kawashima, T. and M. Hishinuma, *Materials Transactions, JIM*, 37 (1996) 1518.
- Keiji, I., M. Murakami, T. Deguchi, A. Morita, N. Tohge and T. Minami, *Journal of the American Ceramic Society*, 72 (1989) 1465.
- Keizer, K., M. J. Verkerk and A. J. Burggraaf, *Ceramurgia International*, 5 (1979) 143.
- Kellett, B. J. and F. F. Lange, *Advanced Ceramic Processing and Technology*, 1 (1990) 1.
- Kendall, K., N. McNalfor, W. J. Clegg and J. D. Birchall, *British Ceramic Proceedings*, 45 (1990) 79.
- Kenjo, T. and M. Nishiya, *Solid State Ionics*, 57 (1992) 295.

- Kettani, M. A., Direct Energy Conversion, Addison-Wesley Publishing Company, London, 1970.
- Khandkar, A. C. and A. V. Joshi, Interface, The Electrochemical Society (1993) 26.
- Kim, E. T., J. W. Lee, S. H. Lee, and S. G. Yoon, Journal of the Electrochemical Society, 140 (1993) 2625.
- Kleitz, M., Solid State Ionics, 3/4 (1981) 513.
- Kudo, T. and H. Obayashi, Journal of the Electrochemical Society, 123 (1976) 415.
- Kumar, R. V. and H. Iwahara, Handbook on the Physics and Chemistry of Rare Earths, 28 (2000) 132.
- Kurzweil, P., J. Ober and D. W. Wabner, Electrochimica Acta, 34 (1989) 1179.
- Kutty, T. R. N. and N. Raghu, Materials Science and Engineering, B13 (1992) 181.
- Labrincha, J. A., L. J. Meng, M. P. dos Santos, F. M. B. Marques and J. R. Frade, Materials Research Bulletin, 28 (1993) 101.
- Ladas, S., S. Kennou, S. Bebelis and C. G. Vayenas, Journal of Physical Chemistry, 97 (1993) 8845.
- Lambert Bates, J., C. W. Griffin, D. D. Marchant and J. E. Garnier, American Ceramic Society Bulletin, 65 (1986) 678.
- Lee, C. H., C. H. Lee, H. Y. Lee and S. M. Oh, Solid State Ionics, 98 (1997) 39.
- Liang, C. C., Chemtech, 5 (1983) 303.
- Lijzenga, C., V. T. Zaspalis, C. D. Ransijn, K. P. Kumar, K. Keizer and A. J. Burggraaf, Key Engineering Materials, 61/62 (1991) 379.
- Linderorth, S., P. V. Hendricksen, M. Mogensen and N. Langvad, Journal of Materials Science, 31 (1996) 5077.
- Liu, M. and A. Khandkar, Solid State Ionics, 52 (1992) 3.
- MacDonald, D. D., Symposium on High Temperature Electrode Materials and Characterization (Ed. D. D. MacDonald and A. C. Khandkar), Electrochemical Society Proceedings, 91-6 (1991) 1.

Mahia, J., C. Vazquez-Vazquez, M. I. Basadre-Pampin, J. Mira, J. Rivas, and M. A. Lopez-Quintela, *Journal of the American Ceramic Society*, 79 (1996) 407.

Maissel, L. I. and R. Glang, *Handbook of Thin film Technology*, McGraw-Hill Book Company, New York, 1970.

Maiwa, H., N. Ichinose and K. Okazaki, *First International Conference on Porcessing Materials for Properties* (1993) 1137.

Mansingh, A. and V. R. Vasant Kumar, *Thin Solid Films*, 167 (1988) L11.

Marinsek, M. and J. Macek, *Key Engineering Materials*, 132-136 (1997) 948.

Masuda, Y., A. Baba, H. Masumoto, T. Goto, M. Minakata and T. Hirai, *Japanese Journal of Applied Physics*, 30 (1991) 2212.

Matsui, Noboru, *Solid State Ionics*, 57 (1992) 121.

Matsui, N., *Denki Kagaku*, 59 (1991) 791.

Meng, G., C. Cao, W. Yu, D. Peng, K. de Vries and A. J. Burggraaf, *Key Engineering Materials* 61/62 (1991) 11.

Metaxas, A. C. and J. G. P. Binner, *Advanced Ceramic Processing and Technology*, 1 (1990) 285.

Mineshige, A., M. Inaba, Z. Ogumi, T. Takahashi, T. Kawagoe, A. Tasaka and K. Kikuchi, *Journal of the American Ceramic Society*, 78 (1995) 3157.

Mineshinge, A., M. Inaba, Z. Ogumi, T. Takahashi, T. Kawagoe, A. Tasaka and K. Kikuchi, *Solid State Ionics*, 86-88 (1996) 1251.

Minh, Nguyen Q., *Journal of the American Ceramic Society*, 76 (1993) 563.

Mishima, Y., H. Mitsuyasu, M. Ohtaki and K. Eguchi, *Journal of the Electrochemical Society*, 145 (1998) 1004.

Mizusaki, J., K. Amano, S. Yamauchi and K. Fueki, *Solid State Ionics*, 22 (1987a) 313.

Mizusaki, J., H. Tagawa, T. Saito, K. Kamitani, T. Yamamura, K. Hirano, S. Ehara, T. Takagi, T. Hikita, M. Ippommatsu, S. Nakagawa and K. Hashimoto, *Journal of the Electrochemical Society*, 141 (1994) 2129.

- Mizusaki, J., K. Amano, S. Yamauchi and K. Fueki, *Solid State Ionics*, 22 (1987b) 323.
- Mogensen, M. and T. Lindegaard, *Proceedings of the 3rd International Symposium on Solid Oxide Fuel Cells*, Electrochemical Society, (1993) 484.
- Nagata, M., H. Hotta and H. Iwahara, *Journal of Applied Electrochemistry*, 24 (1994) 411.
- Nakagawa, N., K. Nakajima, M. Sato and K. Kato, *Journal of the Electrochemical Society*, 146 (1999) 1290.
- Nicoll, A. R., A. Salito and K. Honegger, *Solid State Ionics*, 52 (1992) 269.
- Ogumi, Z., Y. Uchimoto, Y. Tsuji and Z. Takehara, *Solid State Ionics*, 58 (1992) 345.
- Ogumi, Z., T. Ioroi, Y. Uchimoto and Z. Takehara, *Journal of the American Ceramic Society*, 78 (1995) 593.
- Oishi, T., T. Nekazawa and A. Katou, *Electronics and Communications in Japan*, 76 (1993) 50.
- Oniciu, Liviu, *Fuel Cells*, Abacus Press, Kent, England, 1976.
- Overs, A. and I. Riess, *Journal of the American Ceramic Society*, 65 (1982) 606.
- Papic, M. M. and L. A. J. Roosdahl, *Fuel Cells: Their Utility Applications*, Report No. 346 G 470, Report for the Canadian Electrical Association (1986).
- Park, J. H. and R. N. Blumenthal, *Journal of the Electrochemical Society*, 136 (1989) 2867.
- Park, Y. M. and G. M. Choi, *Materials Research Society Symposium Proceedings*, Materials Research Society, 548 (1999) 617.
- Pascual, C., J. R. Jurado and P. Duran, *Ceramic Powders*, (1983) 1015.
- Patil, D. S., N. Venkatramani, V. K. Rohatgi and B. C. Mutsuddy, *Solid State Ionics*, 52 (1992) 189.
- Patterson, J., *Physics of Electronic Ceramics* (1971) 131.
- Peterson and Winnick, *Journal of the Electrochemical Society*, 145 (1998) 1449.
- Powell, C. F., *Vapour Deposition*, Edited by C. F. Powell, J. H. Oxley and J. M. Blocher, John Wiley and Sons, New York (1966) 384.

- Preda, M and R. Dinescu, *Revue Roumaine de Chimie*, 21 (1976) 1023.
- Primdahl, S. and M. Mogensen, *Journal of the Electrochemical Society*, 145 (1998) 2431.
- Pshenichnikov, *Doklady Akademii Nauk Armyanskoi SSR*, 1963
- Raissi A. T., A. Banerjee, K. G. Sheinkopf, *IEEE Proceedings of the 1997 32rd Intersociety Energy Conversion Engineering Conference*, 3/4 (1997) 1953.
- Rice, R., *Advanced Ceramic Processing and Technology*, 1 (1990) 123.
- Robertson, N. L. and J. N. Michaels, *Journal of the Electrochemical Society*, 138 (1991) 1494.
- Sager, W., W. Sun, U. D. Schwartz and H. F. Eicke, *Progress in Colloid and Polymer Science*, 93 (1993) 348.
- Sammes, N. M., M. S. Brown and R. Ratnaraj, *Journal of Materials Science Letters*, 13 (1994) 1124.
- Sasaki, H., M. Suzuki, S. Otoshi, A. Kajimura and M. Ippommatsu, *Journal of the Electrochemical Society*, 139 (1992) L12.
- Sasaki, H., C. Yakawa, S. Otoshi, M. Suzuki and M. Ippommatsu, *Journal of Applied Physics*, 74 (1993) 4608.
- Schiller, G., M. Müller, R. Ruckdäschel, R. Henne and M. Lang, *Thermal Spray: A United Forum for Scientific and Technological Advances, Proceedings of the First United Thermal Spray Conference (1997)* 27.
- Schoonman, J., J. P. Dekker and J. W. Broers, *Solid State Ionics*, 46 (1991) 299.
- Schottky, W., *Zeitschrift fuer Physikalische Chemie Abteilung*, B29 (1935) 335.
- Sheppard, L. M., *Advanced Materials and Processes*, 6 (1987) 46.
- Sheshu, B. D., T. Shi and C. K. Kwok, *Materials Research Society Symposium Proceedings*, 168 (1990) 349.
- Shi-Zhen, Zhu, W. Q. Ming, X. D. Guo, L. Q. Guo, *Journal of Rare Earths*, 12 (1994) 28.
- Shubbarao, E. C., "Zirconia - An Overview," *Advances in Ceramics*, 3, 1-11 (1981).

- Shukla, A. K. and J. Gopalakrishnan, *Bulletin of Electrochemistry*, 11 (1995) 109.
- Slade, R. C. T. and N. Singh, *Solid State Ionics*, 46 (1991) 111.
- Sridhar, S., V. Stancovski and U. B. Pal, *Journal of the Electrochemistry*, 144 (1997) 2479.
- Stochniol, G., E. Syskakis and A. Naoumidis, *Journal of the American Ceramic Society*, 78 (1995) 929.
- Sunde, S., *Journal of the Electrochemical Society*, 142 (1995) L50.
- Suzuki, M., H. Sasaki, S. Otushi, A. Kajimura, N. Sugiura and M. Ippommatsu, *Journal of the Electrochemical Society*, 141 (1994) 1928.
- Takeda, Y., R. Kanno, M. Noda, Y. Tomido and O. Yamamoto, *Journal of the Electrochemical Society*, 134 (1987) 2656.
- Tang, E. Z., D. G. Ivey and T. H. Etsell, *Materials Research Society Symposium Proceedings*, Materials Research Society, 527 (1998) 539.
- Tang, E. Z., T. H. Etsell and D. G. Ivey, *Electrochemical Society Proceedings*, 96-19 (1997a) 71.
- Tang, E. Z., T. H. Etsell and D. G. Ivey, *Electrochemical Society Proceedings*, 96-27 (1997b) 131.
- Tanner, W. C. and A. V. Virkar, *Journal of the Electrochemical Society*, 141 (1994) 1261.
- Tanner, W. C., K. Z. Fung and A. V. Virkar, *Journal of the Electrochemical Society*, 144 (1997) 21.
- Toyama, M., R. Kubo, E. Takata, K. Tanaka and K. Ohwada, *Sensors and Actuators A*, 45 (1994) 125.
- Trubelja, M. F. and V. S. Stubican, *Solid State Ionics*, 49 (1991) 89.
- Tsai, T. and S. A. Barnett, *Solid State Ionics*, 98 (1997) 191.
- Tsai, T. and S. A. Barnett, *Journal of the Electrochemical Society*, 145 (1998) 1696.
- Tsukamoto, K., F. Uchiyama, Y. Kaga, Y. Ohno, T. Yanagisawa, A. Monma, Y. Takahagi, M. J. Lain and T. Nakajima, *Solid State Ionics*, 40/41 (1990) 1003.

- van Herle, J. and A. J. McEvoy, *Berichte der Bunsen Gesellschaft fuer Physikalische Chemie*, 97 (1993) 470.
- van Herle, J. and K. R. Thampi, *Journal of Applied Electrochemistry*, 24 (1994) 970.
- van Hassel, B. A. and A. J. Burggraaf, *Solid State Ionics*, 57 (1992) 193.
- Vayenas, C. G., I. V. Yentekakis, S. I. Bebelis and S. G. Neophytides, *Berichte der Bunsen Gesellschaft fuer Physikalische Chemie*, 99 (1995) 1393.
- Velle, O. J., T. Norby and P. Kofstad, *Solid State Ionics*, 47 (1991) 161.
- Verweij, H., *Advanced Materials*, 10 (1998) 1483.
- Virkar, A. V., *Journal of the Electrochemical Society*, 138 (1991) 1481.
- Virkar, A. V., J. Chen, C. W. Tanner and J. W. Kim, *Solid State Ionics*, 131 (2000) 189.
- Vossen, John, "Thin film Processes," Academic Press Inc, New York, 1978.
- Wang, L. S., E. S. Thiele and S. A. Barnett, *Solid State Ionics*, 52 (1992) 261.
- Wang, S., Y. Jiang, Y. Zhang, W. Li, J. Yan and Z. Lu, *Solid State Ionics*, 120 (1999) 75.
- Watanabe, Y., M. Matsumoto and K. Takasu, *Journal of Power Sources*, 61 (1996) 53.
- Weppner, W., *Journal of Solid State Chemistry*, 20 (1977) 305.
- Wheat, T. A., *Journal of the Canadian Ceramic Society*, 48 (1979) 27.
- Wiemhöfer, H. D., *Berichte der Bunsen Gesellschaft fuer Physikalische Chemie*, 97 (1993) 461.
- Wilkenhoener, R., R. Vassen, H. P. Buchkremer and D. Stover, *Journal of Materials Science*, 34 (1999) 257.
- Williams, D. B. and Carter, C. B., *Transmission Electron Microscopy - Spectrometry*, 4 (1996) 564.
- Winkler, W. and J. Koeppen, *Journal of Power Sources*, 61 (1996) 201.
- Wirtz, G. P. and H. P. Takiar, *Journal of the American Ceramic Society*, 64 (1981) 748.

Xia, C., T. L. Ward, C. Xu, P. Atansova and R. W. Schwartz, *Journal of the Electrochemical Society*, 145 (1998) L4.

Li, X. and B. Hafskjold, *Journal of Physics: Condensed Matter*, 7 (1995) 1255.

Yokokawa, H., N. Sakai, T. Kawada and M. Dokiya, *Solid State Ionics*, 40/41 (1990) 398.

Yoshida, S. and K. Toda, *Electronics and Communications in Japan, Part 2*, 72 (1989) 34.

Zipprich, W., H. D. Wiemhofer, U. Vohrer and W. Gopel, *Berichte der Bunsen Gesellschaft fuer Physikalische Chemie*, 99 (1995) 1406.

Zumdahl, S. S., *Chemistry*, 2nd Edition, D. C. Heath and Company, 1989.

Appendix 1

Wavelength Dispersive X-ray Analysis Data

Specimen Number	Measured Chemical Content (wt%)					Relative Chemical Contents	
	ZrO ₂	Y ₂ O ₃	Pt	Other	Total	ZrO ₂	Y ₂ O ₃
YPO ₄ -st	0.00	59.51	0.00	0.00	59.51	N/A	N/A
Pt-st	2.46	0.39	113.58	0.00	116.42	N/A	N/A
Zircon-st	65.50	0.09	10.91	32.77	109.27	N/A	N/A
Zircon-st*	65.93	0.06	0.00	32.74	98.73	N/A	N/A
Substrate	96.02	4.03	0.00	0.00	100.05	N/A	N/A
6.3-1	62.11	1.60	4.03	26.18	93.92	97.49	2.51
6.3-1	53.63	3.83	10.79	23.50	91.75	93.34	6.66
6.3-1	57.90	1.67	7.79	27.68	95.03	97.20	2.80
6.3-1	51.79	1.46	7.26	24.65	85.16	97.27	2.73
6.3-1	55.59	6.58	2.13	24.97	89.27	89.42	10.58
6.3-1	58.79	1.76	7.02	27.88	95.44	97.10	2.90

Specimen Number	Measured Chemical Content (wt%)					Relative Chemical Contents	
	ZrO ₂	Y ₂ O ₃	Pt	Other	Total	ZrO ₂	Y ₂ O ₃
6.3-1	57.82	2.12	12.75	26.20	98.89	96.46	3.54
6.3-1	64.07	1.57	3.25	27.08	95.97	97.61	2.39
6.3-1	59.35	1.66	8.70	25.62	95.33	97.29	2.71
6.3-1	65.69	1.67	0.37	27.40	95.12	97.53	2.47
6.3-1	62.15	1.47	0.85	27.13	91.60	97.69	2.31
6.3-1	63.74	2.60	0.99	27.75	95.08	96.08	3.92
6.3-1	60.86	1.81	4.03	26.89	93.59	97.12	2.88
6.3-1	58.00	1.55	7.87	25.87	93.29	97.40	2.60
Average					93.53	96.36	3.64
>90 Average					94.58	96.86	3.14
6.3-2	57.12	4.13	1.31	32.96	95.52	93.25	6.75
6.3-2	43.28	2.88	23.96	24.41	94.54	93.75	6.25
6.3-2	59.05	3.94	2.57	30.18	95.74	93.75	6.25
6.3-2	35.72	2.58	34.63	21.55	94.48	93.27	6.73
6.3-2	28.71	1.72	33.48	24.04	87.95	94.34	5.66
6.3-2	47.23	2.86	19.09	24.64	93.82	94.29	5.71
6.3-2	45.06	3.43	15.50	23.62	87.60	92.93	7.07
6.3-2	56.04	2.63	6.19	29.14	93.99	95.52	4.48
6.3-2	60.58	4.12	0.68	32.14	97.52	93.64	6.36
6.3-2	57.02	3.09	0.23	30.42	90.76	94.85	5.15
Average					93.19	93.96	6.04
>90 Average					94.55	94.04	5.96
6.3-3	56.97	5.40	1.22	27.34	90.93	91.34	8.66
6.3-3	53.99	9.07	0.35	27.50	90.92	85.61	14.39
6.3-3	57.46	5.12	0.31	27.53	90.42	91.82	8.18
6.3-3	56.03	6.02	0.69	27.79	90.53	90.30	9.70
6.3-3	53.81	6.12	1.07	26.85	87.85	89.78	10.22
Average					90.13	89.77	10.23
>90 Average					90.70	89.77	10.23
6.3-4	32.40	28.84	0.00	12.54	73.79	52.91	47.09
6.3-4	55.60	9.76	0.61	18.63	84.60	85.07	14.93
6.3-4	55.56	10.11	0.00	18.88	84.56	84.61	15.39
6.3-4	45.58	17.22	0.30	18.76	81.86	72.57	27.43
6.3-4	52.06	13.17	0.18	21.48	86.89	79.80	20.20
6.3-4	54.64	11.14	2.10	20.91	88.79	83.07	16.93
6.3-4	49.98	10.97	0.77	22.07	83.80	82.00	18.00

Specimen Number	Measured Chemical Content (wt%)					Relative Chemical Contents	
	ZrO ₂	Y ₂ O ₃	Pt	Other	Total	ZrO ₂	Y ₂ O ₃
6.3-4	61.57	4.51	0.00	23.58	89.66	93.17	6.83
6.3-4	46.98	15.83	0.00	19.39	82.20	74.80	25.20
6.3-4	56.98	9.64	0.00	24.04	90.67	85.53	14.47
6.3-4	48.39	13.20	1.05	21.74	84.38	78.58	21.42
6.3-4	48.70	19.17	0.00	19.39	87.26	71.76	28.24
6.3-4	55.18	11.86	0.54	23.74	91.32	82.31	17.69
Average					85.37	78.94	21.06
>90 Average					90.11	86.02	13.98
6.3-4	19.16	36.93	0.04	8.81	64.94	34.16	65.84
Average					64.94	34.16	65.84

University of Alberta Library



0 1620 1520 5055

B45562